

AD-A241 095



2

NAVAL POSTGRADUATE SCHOOL Monterey, California



THESIS

**Heat Transfer, Adiabatic Effectiveness and
Injectant Distributions Downstream of Single
and Double Rows of Film-Cooling Holes with
Compound Angles**

by

David T. Bishop, Jr.

September 1990

Thesis Advisor:

Phillip M. Ligrani

Co-Advisor:

Chelakara S. Subramanian

Approved for public release; distribution is unlimited.

91-12227

Unclassified

Security Classification of this page

REPORT DOCUMENTATION PAGE			
1a Report Security Classification Unclassified		1b Restrictive Markings	
2a Security Classification Authority		3 Distribution Availability of Report	
2b Declassification/Downgrading Schedule		Approved for public release; distribution is unlimited.	
4 Performing Organization Report Number(s)		5 Monitoring Organization Report Number(s)	
6a Name of Performing Organization Naval Postgraduate School		7a Name of Monitoring Organization Naval Postgraduate School	
6b Office Symbol (If Applicable) 34		7b Address (city, state, and ZIP code) Monterey, CA 93943-5000	
6c Address (city, state, and ZIP code) Monterey, CA 93943-5000		9 Procurement Instrument Identification Number (If Applicable)	
8a Name of Funding/Sponsoring Organization Wright Aeronautical Laboratories		10 Source of Funding Numbers MIPR FY 1455-89-N0670	
8b Office Symbol		Program Element Number	
8c Address (city, state, and ZIP code) Dayton, OH 45433		Project No	
		Task No	
		Work Unit Accession No	
11 Title (Include Security Classification) HEAT TRANSFER, ADIABATIC EFFECTIVENESS AND INJECTANT DISTRIBUTIONS DOWNSTREAM OF SINGLE AND DOUBLE ROWS OF FILM-COOLING HOLES WITH COMPOUND ANGLES			
12 Personal Author(s) David T. Bishop, Jr.			
13a Type of Report Master's Thesis		13b Time Covered From To	
		14 Date of Report (year, month, day) September 1990	
		15 Page Count 151	
16 Supplementary Notation The views expressed in this thesis are those of the author and do not reflect the official policy or position of the Department of Defense or the U.S. Government.			
17 Cosati Codes		18 Subject Terms (continue on reverse if necessary and identify by block number) Compound Angle Injection, Embedded Vortex, Film-cooling, Turbulent Boundary Layer	
Field	Group	Subgroup	
19 Abstract (continue on reverse if necessary and identify by block number) Experimental results are presented which describe the development and structure of turbulent boundary layer flow downstream of single and double rows of film-cooling holes with compound angles. The film-cooling holes are inclined at an angle of 30 degrees when projected into the spanwise/normal (Y-Z) planes and at an angle of 35 degrees when projected into the streamwise/normal (X-Y) planes with respect to the test surface. Three configurations are used : (1) one row of film-cooling holes with a blowing ratio of $m=0.5$, (2) one row of film-cooling holes with a blowing ratio of $m=1.0$, and (3) two staggered rows of film-cooling holes with a blowing ratio of $m=0.5$. Results indicate that the highest η values are obtained when two rows of compound angle injection cooling holes are employed with a blowing ratio of $m=0.5$, and that the lowest η values result when one row of compound angle injection cooling holes is employed with a blowing ratio of $m=1.0$. Near film cooling holes and for x/d as high as 87, streamwise mean velocity and total pressure distributions show spanwise periodicity near the wall as a result of the discrete nature of the film injection. At $x/d=10.2$, injectant distributions are non-circular in spanwise normal planes. These distributions spread in lateral and normal directions as the boundary layer convects downstream.			
20 Distribution/Availability of Abstract <input checked="" type="checkbox"/> unclassified/unlimited <input type="checkbox"/> same as report <input type="checkbox"/> DTIC users		21 Abstract Security Classification Unclassified	
22a Name of Responsible Individual Phillip M. Ligrani		22b Telephone (Include Area code) (408) 646-3382	
		22c Office Symbol MELi	

DD FORM 1473, 84 MAR

83 APR edition may be used until exhausted

security classification of this page

All other editions are obsolete

Unclassified

Approved for public release; distribution is unlimited.

**Heat Transfer, Adiabatic Effectiveness and Injectant
Distributions Downstream of Single and Double Rows of Film-
Cooling Holes with Compound Angles**

by

**David Turner Bishop, Jr.
Lieutenant, United States Navy
B.S., University of South Alabama, 1985**

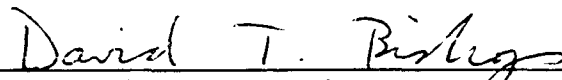
Submitted in partial fulfillment of the requirements
for the degree of

**MASTER OF SCIENCE IN MECHANICAL
ENGINEERING**

from the

**NAVAL POSTGRADUATE SCHOOL
September 1990**

Author:



David Turner Bishop, Jr.

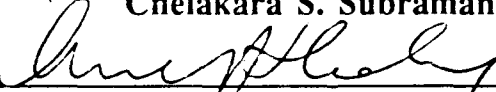
Approved by:



Phillip M. Ligrani, Thesis Advisor



Chelakara S. Subramanian, Co-Advisor



Anthony J. Healey, Chairman, Department of Mechanical
Engineering

ABSTRACT

Experimental results are presented which describe the development and structure of turbulent boundary layer flow downstream of single and double rows of film-cooling holes with compound angles. The film-cooling holes are inclined at an angle of 30 degrees when projected into the spanwise/normal (Y-Z) planes and at angle of 35 degrees when projected into the streamwise/normal (X-Y) planes with respect to the test surface. Three configurations are used : (1) one row of film-cooling holes with a blowing ratio of $m=0.5$, (2) one row of film-cooling holes with a blowing ratio of $m=1.0$ and (3) two staggered rows of film-cooling holes with a blowing ratio of $m=0.5$.

Results indicate that the highest η values are obtained when two rows of compound angle injection cooling holes are employed with a blowing ratio of $m=0.5$, and that the lowest η values result when one row of compound angle injection cooling holes is employed with a blowing ratio of $m=1.0$. Near film cooling holes and for x/d as high as 87, streamwise mean velocity and total pressure distributions show spanwise periodicity near the wall as a result of the discrete nature of the film injection. At $x/d=10.2$, injectant distributions are non-circular in spanwise normal planes. These distributions spread in lateral and normal directions as the boundary layer convects downstream.

Accession For	
NTIS CPAC	J
DTIC TAB	
Unannounced	
Justification	
By	
Distribution	
Availability Codes	
Dist	Availability Codes
A-1	

TABLE OF CONTENTS

I. INTRODUCTION.....	1
A. BACKGROUND.....	1
B. PRESENT STUDY	3
C. EXPERIMENTAL OUTLINE	4
D. THESIS ORGANIZATION	5
II. EXPERIMENTAL APPARATUS AND PROCEDURES.....	6
A. WIND TUNNEL	6
B. INJECTION HOLE CONFIGURATION.....	7
C. INJECTION SYSTEM	7
D. HEAT TRANSFER SURFACE	9
E. HOT-WIRE ANEMOMETRY	11
F. TEMPERATURE MEASUREMENTS	13
G. MEAN VELOCITY MEASUREMENTS	15
H. FLOW VISUALIZATION	16
III. EXPERIMENTAL RESULTS.....	17
A. BOUNDARY LAYER STRUCTURE.....	17
B. HEAT TRANSFER MEASUREMENTS.....	20
1. One row of film cooling holes with $m=0.5$	23
2. One row of film cooling holes with $m=1.0$	24
3. Two rows of film cooling holes with $m=0.5$	24
4. Comparison of film cooling hole configurations	26
C. FIVE HOLE PRESSURE PROBE SURVEYS.....	26
1. One row of film cooling holes with $m=0.5$	27
2. One row of film cooling holes with $m=1.0$	27
3. Two rows of film cooling holes with $m=0.5$	27
D. INJECTANT DISTRIBUTIONS	28
1. One row of film cooling holes with $m=0.5$	29

2. One row of film cooling holes with $m=1.0$	29
3. Two rows of film cooling holes with $m=0.5$	30
E. FLOW VISUALIZATION.....	31
IV. SUMMARY AND CONCLUSIONS	32
APPENDIX A FIGURES	34
APPENDIX B UNCERTAINTY ANALYSIS.....	119
APPENDIX C DATA ACQUISITION, PROCESSING AND PLOTTING PROGRAMS	120
APPENDIX D DATA FILE DIRECTORY.....	125
REFERENCES.....	134
INITIAL DISTRIBUTION LIST.....	136

LIST OF FIGURES

Figure 1. Test Section Coordinate System	35
Figure 2. Top View Schematic of Wind Tunnel Test Section.....	36
Figure 3. Injection Hole Configuration.....	37
Figure 4. Coefficient of Discharge (C_d) versus Reynolds number (Re) for Injection System	38
Figure 5. Injectant Temperature versus Plenum Temperature	39
Figure 6. Stanton number comparison between Exact Solution and Experimental Measurements.....	40
Figure 7. Mean Velocity (U) versus Distance from the wall (Y)	41
Figure 8. Normalized Mean Velocity (U/U_τ) versus Normalized Height (Y/δ)	42
Figure 9. Velocity Profile for $Z/d=-10.6$	43
Figure 10. Velocity Profile for $Z/d=0.0$	44
Figure 11. Velocity Profile for $Z/d=10.6$	45
Figure 12. Normalized Longitudinal Turbulence Intensity (U'/U_τ) versus Normalized Height (Y/δ).....	46
Figure 13. Normalized Longitudinal Turbulence Intensity (U'/U_τ) versus Normalized Height (Y/δ).....	47
Figure 14. Stanton number (St) comparison, 1 row $m=0.5$	48
Figure 15. Spanwise Variation of η , 1 row $m=0.5$	49
Figure 16. Spanwise Variation of St_f/St_0 , 1 row $m=0.5$	50
Figure 17. Spanwise Variation of St/St_0 , 1 row $m=0.5$, $\theta=1.29$	51
Figure 18. Stanton number (St) comparison, 1 row $m=1.0$	52
Figure 19. Spanwise Variation of η , 1 row $m=1.0$	53
Figure 20. Spanwise Variation of St_f/St_0 , 1 row $m=1.0$	54
Figure 21. Spanwise Variation of St/St_0 , 1 row $m=1.0$, $\theta=1.21$	55
Figure 22. Stanton number (St) comparison, 2 rows $m=0.5$	56

Figure 23. Spanwise Variation of η , 2 rows $m=0.5$ (5 data sets)	57
Figure 24. Spanwise Variation of η , 2 rows $m=0.5$ (6 data sets)	58
Figure 25. Spanwise Variation of St_f/St_0 , 2 rows $m=0.5$ (5 data sets).....	59
Figure 26. Spanwise Variation of St_f/St_0 , 2 rows $m=0.5$ (5 data sets).....	60
Figure 27. Spanwise Variation of St/St_0 , 2 rows $m=0.5$, $\theta=1.66$	61
Figure 28. St/St_0 versus θ , 2 rows $m=0.5$, $x/d=33.1$, $Z=0.0$ cm, compact.....	62
Figure 29. St/St_0 versus θ , 2 rows $m=0.5$, $x/d=33.1$, $Z=0.0$ cm, expanded	63
Figure 30. St/St_0 versus θ , 2 rows $m=0.5$, $x/d=54.3$, $Z=0.0$ cm, compact.....	64
Figure 31. St/St_0 versus θ , 2 rows $m=0.5$, $x/d=54.3$, $Z=0.0$ cm, expanded	65
Figure 32. St/St_0 versus θ , 2 rows $m=0.5$, $x/d=75.4$, $Z=0.0$ cm, compact.....	66
Figure 33. St/St_0 versus θ , 2 rows $m=0.5$, $x/d=75.4$, $Z=0.0$ cm, expanded	67
Figure 34. St/St_0 versus θ , 2 rows $m=0.5$, $x/d=96.6$, $Z=0.0$ cm, compact.....	68
Figure 35. St/St_0 versus θ , 2 rows $m=0.5$, $x/d=96.6$, $Z=0.0$ cm, expanded	69
Figure 36. St/St_0 versus θ , 2 rows $m=0.5$, $x/d=33.1$, $Z=-6.35$ cm, compact.....	70
Figure 37. St/St_0 versus θ , 2 rows $m=0.5$, $x/d=33.1$, $Z=-6.35$ cm, expanded	71
Figure 38. St/St_0 versus θ , 2 rows $m=0.5$, $x/d=54.3$, $Z=-6.35$ cm, compact.....	72
Figure 39. St/St_0 versus θ , 2 rows $m=0.5$, $x/d=54.3$, $Z=-6.35$ cm, expanded ...	73
Figure 40. St/St_0 versus θ , 2 rows $m=0.5$, $x/d=75.4$, $Z=-6.35$ cm, compact.....	74
Figure 41. St/St_0 versus θ , 2 rows $m=0.5$, $x/d=75.4$, $Z=-6.35$ cm, expanded ...	75
Figure 42. St/St_0 versus θ , 2 rows $m=0.5$, $x/d=96.6$, $Z=-6.35$ cm, compact.....	76
Figure 43. St/St_0 versus θ , 2 rows $m=0.5$, $x/d=96.6$, $Z=-6.35$ cm, expanded ...	77
Figure 44. St/St_0 versus θ , 2 rows $m=0.5$, $x/d=33.1$, $Z=+6.35$ cm, compact....	78
Figure 45. St/St_0 versus θ , 2 rows $m=0.5$, $x/d=33.1$, $Z=+6.35$ cm, expanded...	79
Figure 46. St/St_0 versus θ , 2 rows $m=0.5$, $x/d=54.3$, $Z=+6.35$ cm, compact....	80
Figure 47. St/St_0 versus θ , 2 rows $m=0.5$, $x/d=54.3$, $Z=+6.35$ cm, expanded...	81
Figure 48. St/St_0 versus θ , 2 rows $m=0.5$, $x/d=75.4$, $Z=+6.35$ cm, compact....	82
Figure 49. St/St_0 versus θ , 2 rows $m=0.5$, $x/d=75.4$, $Z=+6.35$ cm, expanded...	83
Figure 50. St/St_0 versus θ , 2 rows $m=0.5$, $x/d=96.6$, $Z=+6.35$ cm, compact....	84
Figure 51. St/St_0 versus θ , 2 rows $m=0.5$, $x/d=96.6$, $Z=+6.35$ cm, expanded...	85
Figure 52. Comparison of η with x/d	86

Figure 53. Comparison of η with x/s	87
Figure 54. Comparison of St_f/St_0 with x/d	88
Figure 55. Streamwise Velocity Field, 1 row $m=0.5$, $x/d=10.2$	89
Figure 56. Streamwise Velocity Field, 1 row $m=0.5$, $x/d=45.8$	90
Figure 57. Streamwise Velocity Field, 1 row $m=0.5$, $x/d=86.8$	91
Figure 58. Total Pressure Field, 1 row $m=0.5$, $x/d=10.2$	92
Figure 59. Total Pressure Field, 1 row $m=0.5$, $x/d=45.8$	93
Figure 60. Total Pressure Field, 1 row $m=0.5$, $x/d=86.8$	94
Figure 61. Streamwise Velocity Field, 1 row $m=1.0$, $x/d=10.2$	95
Figure 62. Streamwise Velocity Field, 1 row $m=1.0$, $x/d=45.8$	96
Figure 63. Streamwise Velocity Field, 1 row $m=1.0$, $x/d=86.8$	97
Figure 64. Total Pressure Field, 1 row $m=1.0$, $x/d=10.2$	98
Figure 65. Total Pressure Field, 1 row $m=1.0$, $x/d=45.8$	99
Figure 66. Total Pressure Field, 1 row $m=1.0$, $x/d=86.8$	100
Figure 67. Streamwise Velocity Field, 2 rows $m=0.5$, $x/d=10.2$	101
Figure 68. Streamwise Velocity Field, 2 rows $m=0.5$, $x/d=45.8$	102
Figure 69. Streamwise Velocity Field, 2 rows $m=0.5$, $x/d=86.8$	103
Figure 70. Total Pressure Field, 2 rows $m=0.5$, $x/d=10.2$	104
Figure 71. Total Pressure Field, 2 rows $m=0.5$, $x/d=45.8$	105
Figure 72. Total Pressure Field, 2 rows $m=0.5$, $x/d=86.8$	106
Figure 73. Local Injectant Distribution, 1 row $m=0.5$, $x/d=10.2$	107
Figure 74. Local Injectant Distribution, 1 row $m=0.5$, $x/d=45.8$	108
Figure 75. Local Injectant Distribution, 1 row $m=0.5$, $x/d=86.8$	109
Figure 76. Local Injectant Distribution, 1 row $m=1.0$, $x/d=10.2$	110
Figure 77. Local Injectant Distribution, 1 row $m=1.0$, $x/d=45.8$	111
Figure 78. Local Injectant Distribution, 1 row $m=1.0$, $x/d=86.8$	112
Figure 79. Local Injectant Distribution, 2 rows $m=0.5$, $x/d=10.2$	113
Figure 80. Local Injectant Distribution, 2 rows $m=0.5$, $x/d=45.8$	114
Figure 81. Local Injectant Distribution, 2 rows $m=0.5$, $x/d=86.8$	115
Figure 82. Flow Visualization, 1 row $m=0.5$	116

Figure 83. Flow Visualization, 1 row $m=1.0$	116
Figure 84. Flow Visualization, 1 row $m=1.5$	117
Figure 85. Flow Visualization, 2 rows $m=0.5$	117
Figure 86. Flow Visualization, 2 rows $m=1.0$	118
Figure 87. Flow Visualization, 2 rows $m=1.5$	118

LIST OF SYMBOLS

- C_d - coefficient of discharge
 C_f - skin friction coefficient
 d - injection hole diameter (0.945 cm)
 h - average heat transfer coefficient
 k - thermal conductivity
 m - blowing ratio, $\frac{\rho_c U_c}{\rho_\infty U_\infty}$
 Pr - Prandtl number
 Re - Reynolds number
 St - Stanton number
 St_f - Iso-energetic Stanton number
 St_0 - Baseline Stanton number, no film cooling
 T - static temperature
 T_c - coolant temperature
 T_{inj} - injectant temperature
 T_{plenum} - plenum temperature
 T_w - wall temperature
 T_∞ - freestream temperature
 U - mean velocity
 U' - longitudinal turbulence intensity
 U^+ - turbulent flow parameter
 U_τ - friction velocity
 U_∞ - freestream velocity

- X - downstream distance measured from the leading edge of the boundary layer trip
- x/d - dimensionless streamwise position : streamwise distance measured from the downstream edges of the injection holes divided by the injection hole diameter
- Y - distance normal to the test surface
- Y^+ - turbulent flow parameter
- Y/δ - non-dimensional height
- Z - spanwise distance measured from the test surface centerline
- Z/d - dimensionless spanwise position

Greek Symbols

- α - thermal diffusivity
- β_1 - complete beta function
- β_{ui} - incomplete beta function
- δ - boundary layer thickness based on the position y where $U=0.99 U_\infty$
- δ_1 - momentum thickness
- δ_2 - energy thickness
- ξ - unheated starting length
- η - adiabatic film cooling effectiveness
- ν - kinematic viscosity
- θ - non-dimensional temperature, $\frac{T_c - T_\infty}{T_w - T_\infty}$
- ρ - density

Subscripts

- ad - adiabatic condition
- c - coolant
- f - film flow
- m - main flow
- o - stagnation condition
- w - wall
- ∞ - freestream

ACKNOWLEDGMENTS

This research was sponsored by Wright Aeronautical Laboratories, Wright-Patterson Air Force Base, MIPR FY 1455-89-N0670. Program monitor was Dr. Bill Troha.

Professor Phillip Ligrani was a very influential and important driving force behind the composition of this study. Dr. Chelakara Subramanian was helpful with his knowledge of computer programming and technical familiarity of all laboratory procedures employed.

I wish to thank both Professor Phillip Ligrani and Dr. Subramanian for their patience, guidance and never ending enthusiasm for this study.

I. INTRODUCTION

A. BACKGROUND

Current inlet temperatures of gas turbines are approaching 2000 K. These high temperatures can cause substantial thermal loading of turbine blades and endwalls. Film cooling is one method of protection for these gas turbine surfaces. In many situations over the past 10-15 years, simple angle injection is employed on turbine blades, turbine endwalls, combustion chamber linings, and afterburner linings so that film is injected approximately in the direction of the mainstream flow. However, more recently, these components include film holes with compound angle orientations. This is advantageous since they often provide better protection and higher film effectiveness than simple angle orientations. However, almost no data is available in the archival literature for the flow field downstream of injection holes with compound angle orientations. The present study is intended to remedy this deficiency.

The present work is additionally unique since adiabatic film cooling effectiveness values are determined using linear superposition theory from Stanton number ratios measured at different injection temperatures. This is possible since the three-dimensional energy equation which describes the flow field is linear and homogeneous in its dependent variable, temperature. This equation is of the form :

$$\alpha \left(\frac{\partial^2 T}{\partial x^2} + \frac{\partial^2 T}{\partial y^2} + \frac{\partial^2 T}{\partial z^2} \right) = u \frac{\partial T}{\partial x} + v \frac{\partial T}{\partial y} + w \frac{\partial T}{\partial z} \quad (\text{Equation 1.1})$$

where $\alpha = \frac{k}{\rho C}$. (Equation 1.2)

The technique of superposition was first applied to film cooling by Metzger, Carper and Swank [Ref. 1]. They examined the effect of secondary fluid injection through nontangential slots on the heat transfer in regions near the injection site. They found that slight but significant differences in the various tangential injection geometries employed are reflected in rather large variations in adiabatic wall temperature variations. Since there are large wall temperature variations, heat transfer rate comparisons are difficult. They develop the parameter Φ , which depends on a temperature difference ratio (θ) and a mass velocity ratio (m), to facilitate comparisons of various film cooling schemes. The parameter Φ is defined as :

$$\Phi = \frac{h_{with\ film\ injection}}{h_{without\ injection}} \quad (\text{Equation 1.3})$$

In a comment on the Metzger, Carper and Swank paper, E.R.G. Eckert relates Φ to the adiabatic wall temperature (T_{ad}). This quantity is defined as the temperature which the film-cooled wall assumes when the specific heat flux q in the following equation is zero.

$$q = hA(T_w - T_m) \quad (\text{Equation 1.4})$$

An effectiveness parameter is then expressed as :

$$\eta = \frac{T_{ad} - T_m}{T_f - T_m} = \frac{1}{\theta_{ad}} \quad (\text{Equation 1.5})$$

which is the reciprocal of the temperature parameter θ for the condition of $T_w=T_{ad}$. A new heat transfer coefficient is introduced by :

$$\dot{q} = h_f A (T_w - T_{ad}) \quad (\text{Equation 1.6})$$

Finally, a heat transfer ratio can be defined as :

$$\frac{h_f}{h} = \frac{\theta_{ad}}{\theta_{ad} - \theta} \quad (\text{Equation 1.7})$$

These ideas presented by E.R.G. Eckert are of use for the present study. Later, Ligrani and Camci [Ref. 2] expanded their approach by applying it to a variable property flow.

B. PRESENT STUDY

The objective of the present work is to determine Stanton numbers at $\theta=0$, 0.5, 0.7, 1.0 and 1.2 at x/d ratios of 6.7, 17.2, 33.1, 54.3, 75.4 and 96.6. From these, adiabatic film cooling effectiveness is determined using linear superposition theory applied to heat transfer results obtained from a constant heat flux surface. These results are to be obtained and analyzed for three different injection configurations : (1) one row of film-cooling holes with a

blowing ratio of $m=0.5$, (2) one row of film-cooling holes with a blowing ratio of $m=1.0$ and (3) two rows of film-cooling holes with a blowing ratio of $m=0.5$.

C. EXPERIMENTAL OUTLINE

The present study consists of five different experiments :

1. Determination of the boundary layer structure.
2. Measurement of heat transfer distributions including Stanton numbers, Stanton number ratios and adiabatic film cooling effectiveness at 21 spanwise locations at x/d ratios of 6.7, 17.2, 33.1, 54.3, 75.4 and 96.6.
3. Measurement of mean velocities and total pressure in the Y-Z planes at x/d ratios of 10.2, 45.8 and 86.8.
4. Surveys of mean temperature ($T - T_w$) to provide information on injectant distributions in Y-Z planes at x/d ratios of 10.2, 45.8 and 86.8.
5. Flow visualization of injectant.

Four different experimental configurations were utilized :

1. No film cooling ($m=0.0$).
2. One row of five compound angle injection cooling holes with $m=0.5$ and $\theta = 0, 0.5, 0.9, 1.1$ and 1.3 .
3. One row of five compound angle injection cooling holes with $m=1.0$ and $\theta = 0, 0.5, 0.7, 1.0$ and 1.2 .
4. Two rows of five compound angle injection cooling holes with $m=0.5$ and $\theta = 0, 0.5, 0.8, 1.1, 1.4$ and 1.6 .

D. THESIS ORGANIZATION

The remainder of this thesis is organized as follows. Chapter II discusses the experimental apparatus and procedures. Chapter III contains experimental results. Chapter IV then presents a summary and conclusions. Appendix A contains all of the figures. Appendix B gives the uncertainty levels for the parameters measured and calculated. Appendix C discusses all of the data acquisition, processing and plotting programs developed and used for this thesis. Appendix D contains a data file directory listing the names of all data files contained on micro floppy disks.

II. EXPERIMENTAL APPARATUS AND PROCEDURES

A. WIND TUNNEL

The open-circuit, subsonic wind tunnel located in the laboratories of the Department of Mechanical Engineering of the Naval Postgraduate School is employed for the present study. This is the same wind tunnel used in References 3,4,5,6 and 8. A variable speed centrifugal blower is the source of the wind tunnel flow. A coarse filter is located on the inlet of the blower and the surrounding room air is ejected from the blower through a diffuser. A fine grade filter within the diffuser aids in the removal of small air particulates. Four baffle vanes are also contained to minimize noise and flow separation. The inlet air then passes into a header box which contains three screens and a honeycomb to further reduce spatial non-uniformities of the flow. After the header, the flow enters a 16 to 1 ratio nozzle and exits into the wind tunnel test section.

The test section is a rectangular duct 3.05 m long and 0.61 m wide. The test section contains the constant heat flux transfer surface as well as the two rows of compound angle film injection holes. The adjustable top wall of the test section permits changes in the streamwise pressure gradient. For the present study, a zero pressure gradient is maintained along the length of the test section (without the film cooling) to within 0.01 inches of water differential pressure. The freestream velocity is adjustable from 1 m/s to 40 m/s, and the freestream turbulence intensity is approximately 0.1 percent for a freestream velocity of 30 m/s. The boundary layer is tripped near the nozzle exit 1.077 m upstream of the constant heat flux transfer surface. Figure 1 shows the coordinate system as

well as locations of the rows of thermocouples placed within the heated test surface. Figure 2 shows a top view of the wind tunnel test section. When the heat transfer section is in operation, an unheated starting length of 1.077 m exists. The direction of heat transfer is from the constant heat flux surface to the air.

B. INJECTION HOLE CONFIGURATION

The injection hole configuration consists of two rows of holes, where each row contains five injection cooling holes with compound angle orientations. The holes are 0.945 cm in diameter, with centerlines spaced $7.8d$ apart within each row. Centerlines of holes in separate rows are separated by $5.2d$ in the X-direction. The holes in the two rows are staggered with Z-distances between hole centerlines from different rows of $3.9d$. The plane of each injection hole is angled at 50.5 degrees from the streamwise/normal (X-Y) plane. Within the plane of each hole, centerlines are oriented at angles of 24 degrees from the X-Z plane of the test surface. When projected into spanwise/normal (Y-Z) planes, holes are inclined at an angle of 30 degrees with respect to the test surface. When projected into streamwise/normal (X-Y) planes, holes are inclined at an angle of 35 degrees from the test surface. Figure 3 shows details of the compound-angle injection hole configuration.

C. INJECTION SYSTEM

Film coolant is injected from either one or two rows of injection holes into the boundary layer developing along the bottom wall of the test section. Air for the film coolant injection begins in a 10 hp, two stage, 150 psig Ingersol-Rand air compressor. From the compressor, the air flows through a pressure

regulator, a rotameter, a diffuser and finally into the injection heat exchanger and plenum chamber. The heat exchanger allows heating of the injectant at temperatures from 10 to 70 degrees Celsius above the ambient air temperature. The upper surface of the plenum chamber contains ten brass injection tubes, each three inches long, which terminate in the two rows of five compound angle injection cooling holes. Additional details on the injection system are presented in References 3 and 4.

The present injection system is qualified from measurements of discharge coefficients as a function of injection Reynolds number. A plot of the coefficient of discharge (C_d) versus Reynolds number (Re) is shown in Figure 4. Because the range and magnitudes of these data are as expected, the injection system is considered to be operating normally.

All film cooling parameters, such as the blowing ratio, are calculated using the temperature at the exits of the injection holes, (T_{inj}). For this reason, additional qualification tests were employed to determine the relation between injection plenum temperature (T_{plenum}) and T_{inj} . A plot of injectant temperature (T_{inj}) versus plenum temperature (T_{plenum}) is shown in Figure 5. The equation relating the two temperatures is given by :

$$T_{inj} (^{\circ}C) = 2.2907 + 0.85948 * T_{plenum} (^{\circ}C) \quad (\text{Equation. 2.1})$$

This equation represents an empirical fit to experimental data for blowing ratios ranging from 0 to 1.5, and ranges of injection temperature from 0 to 100 degrees Celsius. With this arrangement, the injection temperature may be calculated after measurement of the plenum temperature.

When both rows of cooling holes are employed, the blowing ratio is maintained at $m=0.5$. When only the downstream row is used, blowing ratios of $m=0.5$ and $m=1.0$ are used. With this arrangement, the upstream holes are plugged and covered with cellophane tape.

D. HEAT TRANSFER SURFACE

The heat transfer test surface is designed to provide constant heat flux over most of its area. This plate is inserted into the bottom wall of the wind tunnel test section. The upper surface of the plate is maintained level with the test surface and adjacent to the wind tunnel airstream using height adjustment screws mounted in the plexiglass support frame. The test surface is made of stainless steel foil, with dimensions of 1.3 m x 0.476 m x 0.20 mm, coated with seven layers of liquid crystals. Copper-constantan thermocouples are attached to the underside of the stainless steel foil in six rows of 21 thermocouples per row, with a spanwise spacing of 1.27 cm between individual thermocouples. Thermocouple lead wires are embedded in grooves cut into a triple sheet of 0.254 mm thick double sided tape. RTV epoxy is then used to fill spaces around thermocouple lead wires within these grooves. Electrobond epoxy is used to attach a foil heater, with dimensions of 1.0 mm x 1.118 m x 0.438 m and manufactured by the Electrofilm Corporation, to the underside of the double sided tape. The heater is rated at 120 volts and 1500 watts, with interior foil designed with adjacent braces sufficiently close together to maintain uniform dissipation of heat throughout the heater. A 12.7 mm thick Lexan sheet, followed by 25.4 mm of foam insulation, an 82.55 mm thick Styrofoam layer, three sheets of 0.254 mm thick Lexan and one 9.53 mm thick sheet of balsa wood

make up the remaining insulation. A plexiglass support frame then encases the bottom portion of the test surface and provides support. This frame is then mounted on the underside of the wind tunnel.

The energy balance by Ortiz [Ref. 3] is used to determine conductive heat losses from the heat transfer plate. These amount to approximately 1.5 to 2.5 percent of the total power into the heater, whereas radiation losses average about 8.5 percent of the total power. The contact resistance between the thermocouples and the upper foil is given by Joseph [Ref. 5], but later verified by Williams [Ref. 6].

To provide a baseline data check, Stanton numbers, measured without film injection present, are compared to an empirical relationship given by Kays and Crawford [Ref. 8]. This particular relationship represents turbulent boundary layer flow in a zero pressure gradient over a constant heat flux surface just downstream of an unheated starting length. The equation is given by :

$$St Pr^{0.4} = 0.03 Re^{-0.2} \times \frac{\beta_1(19,109)}{\beta_{u1}(19,109)} \quad (\text{Equation 2.2})$$

Here, β_1 and β_{u1} are the Beta function and the incomplete Beta function, respectively. The term $u1$ is defined as :

$$u1 = 1 - \left(\frac{\xi_1}{X} \right)^{\frac{9}{10}} \quad (\text{Equation 2.3})$$

β_{u1} is a function of $u1$.

Equation 2.2 is compared to the baseline data in Figure 6. For Reynolds numbers greater than 8×10^5 , experimental data values are within ± 4 percent of Equation 2.2 providing a check on spanwise-averaged Stanton number behavior with no film injection present.

E. HOT-WIRE ANEMOMETRY

The most common instrument used for measuring instantaneous velocities in turbulent flows is the hot-wire anemometer. The basic theory of operation is quite straightforward. A hot-wire anemometry system consists of one or more thin sensor wires connected to supports, each wire forming a leg of a Wheatstone bridge. In a constant temperature hot-wire system (used in this study) the bridge is balanced before the probe is exposed to the flow by means of a variable resistor. The resistance required to balance the bridge is called the "cold wire" resistance. The variable resistance is then increased to an arbitrary value, usually from 1.2 to 1.8 times the "cold wire" resistance. To operate the system, a small current is passed through the circuit causing resistive heating and a temperature increase in the wire. The resistance of the wire increases until the bridge is rebalanced. The resistance is related to temperature by :

$$R=R_0[1+\alpha(T-T_0)] \quad (\text{Equation 2.4})$$

where R is the resistance at temperature T , R_0 is the resistance at reference temperature T_0 and α is the temperature coefficient of resistance.

When the probe is exposed to a flow, convective cooling of the wire occurs and the wire resistance will decrease causing a bridge unbalance. A feedback

loop is used to detect this unbalance and the current flow in the circuit is increased by a feedback amplifier, rebalancing the bridge. Since the feedback amplifier responds very quickly, the wire temperature and resistance remain virtually constant and flow velocity is measured as a function of bridge voltage. This bridge voltage is directly proportional to the current.

The widely accepted relationship between bridge voltage and effective cooling velocity in a forced convection environment is given by :

$$U_{eff} = K(E^2 - E_{oc}^2)^{\frac{1}{n}} \quad (\text{Equation 2.5})$$

where E is the bridge voltage at effective cooling velocity U_{eff} , and E_{oc} is the bridge voltage extrapolated from forced convection calibration at $U_{eff}=0$ (no-flow voltage). K and n are empirical constants found by calibration. The effective cooling velocity is defined as the component of the velocity vector that is normal to the wire [Ref. 4].

Velocity calibration involves placing the probe at a fixed orientation to a steady flow of known velocity U , recording the measured voltage E , and then repeating this procedure for a number of known flow velocities. The calibration is done outside the turbulent boundary layer where turbulence intensity is lowest. A simple linear relationship between E^2 and U^n is then given by :

$$E^2 = E_{oc}^2 + BU^n \quad (\text{Equation 2.6})$$

With measured voltage E and known velocity U , the computer program HWCAL is run on the Naval Postgraduate School's IBM 310 main frame computer to determine the calibration constants B and E_{oc} with a specified value of $n=0.45$. The program HWRED is then used, with the known calibration constants, to determine velocity distributions, from which various boundary layer parameters such as δ , δ_1 , δ_2 , the Karman Shape Factor and the Clauser Shape Factor are calculated.

F. TEMPERATURE MEASUREMENTS

All temperature measurements are made using calibrated copper-constantan thermocouples. These include heat transfer surface temperatures, the freestream temperature, local boundary layer temperatures and the injection plenum temperature. The calibration equation used for heat transfer surface temperatures is given by Ortiz [Ref. 3]. These are connected to channels 1 - 126 of the data acquisition system. The calibration equation used for the freestream thermocouple is given by Williams [Ref. 6]. This thermocouple is connected to data acquisition channel 147.

New thermocouples are employed in the plenum chamber and used to measure film injectant temperatures in the boundary layer. These were calibrated using a bath whose temperature is regulated using heaters and anti-freeze. Bath temperatures during calibration are measured using a platinum resistance thermometer as a reference. From this calibration, a third-order polynomial representing temperature as a function of thermocouple output

voltage (E-volts) was determined which is given by :

$$T(^{\circ}\text{C}) = 0.0858454 + 26017.4569 * E - 74032.8 * E * E + 35639480 * E * E * E$$

(Equation 2.7)

This same equation applies to all new thermocouples employed. Three are used on channels 148, 149 and 150 for measurement of plenum temperature. Two of these same thermocouples are employed on channels 147 and 153 for measurement of the freestream temperature and boundary layer temperature respectively, as injection distributions are determined.

Temperature surveys to determine injectant distributions are performed using the boundary layer temperature (T) thermocouple and the freestream temperature (T_{∞}) thermocouple to obtain distributions of $(T - T_{\infty})$. For these tests, freestream temperature is maintained at ambient temperature while injectant is heated to 50 degrees Celsius in the injection plenum, with no power applied to the heat transfer test plate. For each survey, local temperatures are taken at 400 (10 x 40) locations in the Y-Z plane at a particular x/d location. The spatial resolution between sampling points is 0.2 inches in each direction (Y and Z), and the overall sampling plane dimensions are 6 cm x 22 cm. The traversing device consists of spanwise and vertical traversing blocks allowing two degrees of freedom. Each is mounted on separate assemblies consisting of two steel case hardened support shafts and a 20 thread per inch pitch drive screw. Separate M092-FD310 stepping motors are used to drive each of the two shafts. A two-axis Motion Controller (MITAS), equipped with 2K bytes of

memory and a MC68000 16 bit microprocessor controls a motor drive which runs the motors. The motors, controller and drive are manufactured by the Superior Electric Company. Software within a Hewlett-Packard Series 9000 Model 310 computer provides instructions which control operation of the controller and traversing device.

A Hewlett-Packard 3497A Data acquisition/Control Unit with a Hewlett-Packard 3498A extender is used to collect all voltages from the thermocouples used. These units are also controlled by a Hewlett-Packard Series 9000 Model 310 computer.

G. MEAN VELOCITY MEASUREMENTS

A DC-250-24CD five hole pressure probe manufactured by the United Sensors and Control Corporation is used to measure the three mean velocity components. The pressure probe has a tip diameter of 6.35 mm and is mounted on the automated traversing device discussed in the temperature measurements section above. Calibration characteristics, given by Williams [Ref. 6], are used to convert the pressure coefficients into velocity components. During these surveys, the freestream temperature, heat transfer surface temperatures, and the plenum injectant temperature are maintained at ambient conditions. A separate Celesco model LCVR differential pressure transducer is used to measure the pressure from each of the five ports of the pressure probe. Each transducer has a full scale pressure range of 2.0 cm of differential water pressure. Transducer output signals are converted to D.C. voltage by five Celesco CD-10D carrier demodulators. The converted voltages are then sent to the Hewlett-Packard 3497A Data Acquisition Unit.

H. FLOW VISUALIZATION

A Rosco Electric Fog/Smoke Machine, Model 1500, is used to supply fog to the injection plenum enabling the injectant to be visualized. A commercial fog/smoke generator is employed because it is safer, more compact and more convenient than a wood burning smoke generator. The fog machine uses a mix of glycols of low molecular weight. The fluid is drawn into the device interior, heated to near its vaporization point and then atomized by forcing the fluid through an orifice. The smoke is carried from the smoke generator to the plenum chamber through a 10.3 cm diameter tube. During these tests, the plenum pressure is maintained entirely by the Smoke Machine, and freestream velocity is adjusted to give desired blowing ratios.

A Nikon F-3 SLR camera body with a 55 mm, f2.8 lens is used for the photography. A tripod is used for mounting and stability. Spotlights are used for lighting. When photographs are taken, the camera is positioned approximately 0.6 m from above the transparent top wall of the wind tunnel test section, and extraneous lighting is minimized as much as possible. An f-stop of either 4 or 5.6, which corresponds to a shutter speed of about 1/80 second, are used for all photographs.

III. EXPERIMENTAL RESULTS

A. BOUNDARY LAYER STRUCTURE

Measurements of the turbulent boundary layer structure were conducted just downstream of the injection holes at $x/d=2.75$. These are intended to provide a check on the behavior of flow along the wind tunnel test surface when no film injection is employed. Figures 7 - 13 show various dimensional and non-dimensional quantities. Table I provides information on a number of parameters determined from mean velocity profiles at different locations. The spanwise locations are $Z/d=-10.6$, $Z=-10$ cm, on the left, to $Z/d=0.0$, $Z=0.0$ cm, on the center and $Z/d=10.6$, $Z=10$ cm on the right. Right and left are considered when looking downstream.

TABLE I. BOUNDARY LAYER PARAMETERS

<u>Quantity (units)</u>	<u>Spanwise Locations</u>		
	<u>Z/d=-10.6</u> <u>Z=-10 cm</u>	<u>Z/d=0.0</u> <u>Z=0 cm</u>	<u>Z/d=10.6</u> <u>Z=10 cm</u>
δ (mm)	10.087	9.168	9.926
δ_1 (mm)	2.007	2.058	2.183
δ_2 (mm)	1.19	1.15	1.26
Karman Shape Factor	1.68	1.79	1.73
Momentum Thickness Reynolds No.	748.0	725.5	812.1
Skin Friction Coefficient (Clauser Plot)	0.00232	0.00229	0.00224
Friction Velocity (m/s)	0.477	0.475	0.478
Clauser Shape Factor	8.42	9.24	8.9

All mean profiles (Figures 7-11) were measured on July 3, 1990, whereas all longitudinal turbulence intensity profiles (Figures 12 and 13) were measured on July 2, 1990. All results were obtained using DANTEC 55P05 single hot wire sensors. Sensing length is 1.25 mm and sensors are oriented normal to the airstream and parallel to the test surface. Using averages of thicknesses for the three spanwise locations investigated, values of δ/d , δ_1/d and δ_2/d are 1.029, 0.22, and 0.127, respectively.

Figure 7 shows a plot of mean velocity (U) versus distance from the wall (y) in dimensional form. The plot shows a velocity deficit typical of turbulent boundary layers at low momentum thickness Reynolds numbers. Because the three profiles from different spanwise locations are very similar, the flow is spanwise uniform. In Figure 8, the same profiles are presented such that velocity is normalized using the freestream velocity (U_∞), and position is normalized using the boundary layer thickness (δ). The boundary layer thickness is based on the distance from the wall where U is equal to 99% of the freestream velocity (U_∞). Results in Figure 8 also evidence spanwise uniformity, as expected.

Figures 9-11 show profiles from Figures 7 and 8 in inner boundary layer coordinates along with the log-law velocity profile. These coordinates are U_+ and y_+ which are defined as :

$$U_+ = \frac{U}{U_\tau} \quad \text{(Equation 3.1)}$$

and
$$y_+ = \frac{yU_\tau}{\nu} \quad \text{(Equation 3.2)}$$

where $U_\tau = \text{friction velocity} = U_* \sqrt{\frac{C_f}{2}}$ (Equation 3.3)
 $C_f/2 = \text{skin friction coefficient}$
 $\nu = \text{kinematic viscosity}$

Values of U_τ and $C_f/2$ were determined using a Clauser plot. Determination of $C_f/2$ using a Clauser plot begins with two equations given by :

$$y_+ U_+ = \frac{Uy}{\nu} \quad (\text{Equation 3.4})$$

and $\frac{Uy}{\nu} = y_+ \left[5.1 + \frac{1}{0.41} \ln y_+ \right]$ (Equation 3.5)

Using the left-hand term of Equation 3.5 applied in the log-law region of the turbulent boundary layer, y_+ on the right-hand side may then be determined. With this information, friction velocity and skin friction coefficient are calculated using equations of the form :

$$U_\tau = \frac{y_+ \nu}{y} \quad (\text{Equation 3.6})$$

and $\frac{C_f}{2} = \frac{U_\tau^2}{U^2}$ (Equation 3.7)

Because the friction velocity given by Equation 3.6 is then used to determine y_+ and U_+ , data in Figures 9-11 agree with the log-law equation given by :

$$U_+ = 5.1 + \frac{1}{0.41} \ln y_+ \quad (\text{Equation 3.8})$$

for values of y_+ between 90 and 300. For values of y_+ greater than 300, the U_+ data are above Equation 3.8 in the wake region. For values of y_+ less than 90, the data are below Equation 3.8 in the viscous sublayer.

Figures 12 and 13 show normalized distributions of longitudinal turbulence intensities as functions of non-dimensional distance from the wall, (y/δ) . In Figure 12, turbulence intensities are normalized using the freestream velocity, U_∞ , and in Figure 13 turbulence intensities are normalized using the friction velocity, U_τ . Both plots evidence typical turbulent behavior as well as spanwise uniformity of the flow.

B. HEAT TRANSFER MEASUREMENTS

Heat transfer measurements are presented in three parts, where each part addresses results from a different film injection configuration. These configurations are : (1) one row of compound angle injection cooling holes with a blowing ratio of $m=0.5$, (2) one row of compound angle injection cooling holes with a blowing ratio of $m=1.0$, and (3) two rows of compound angle injection cooling holes with a blowing ratio of $m=0.5$. For all three arrangements, plots of Stanton number versus Reynolds number are presented for various values of non-dimensional temperature (θ). Plots of the spanwise variation of adiabatic film cooling effectiveness (η), iso-energetic Stanton number ratio (St_f/St_o) and Stanton number ratio (St/St_o) are then given, where the last of these is given for $\theta=1.29, 1.21$ and 1.66 , respectively . In addition to these figures, results for the third configuration include plots showing the linearity of St/St_o versus θ for

different values of x/d . At the end of this discussion, variations of η with x/d and x/s , and St_f/St_o with x/d are compared for all three configurations.

Values of η and St_f/St_o are determined using the linear superposition technique. This is possible since the three-dimensional energy equation which describes the flow field is linear and homogeneous in its dependent variable, temperature. Determination of η and St_f/St_o begins with five governing equations given by :

$$\theta = \frac{T_c - T_\infty}{T_w - T_\infty} \quad (\text{Equation 3.9})$$

$$\eta = \frac{T_{aw} - T_\infty}{T_c - T_\infty} \quad (\text{Equation 3.10})$$

$$\dot{q}''_o = h_o(T_w - T_\infty) \quad (\text{Equation 3.11})$$

$$\dot{q}'' = h(T_w - T_\infty) \quad (\text{Equation 3.12})$$

$$\dot{q}'' = h_f(T_w - T_{aw}) \quad (\text{Equation 3.13})$$

Equation 3.9 is the definition of a non-dimensional temperature ratio and Equation 3.10 is the definition of the adiabatic film cooling effectiveness. Equation 3.11 is the heat flux without film cooling and Equations 3.12 and 3.13 give values of heat flux with film cooling. Setting Equations 3.12 and 3.13 equal

to one another yields :

$$h(T_w - T_\infty) = h_f(T_w - T_{aw}) \quad (\text{Equation 3.14})$$

Now, dividing Equation 3.14 by the right-hand side of Equation 3.11 yields :

$$\frac{h(T_w - T_\infty)}{h_o(T_w - T_\infty)} = \frac{h_f(T_w - T_{aw})}{h_o(T_w - T_\infty)} \quad (\text{Equation 3.15})$$

Rearranging Equation 3.15 then gives :

$$\frac{h}{h_o} = \frac{h_f}{h_o}(1 - \eta\theta) \quad (\text{Equation 3.16})$$

From Equation 3.16, the Stanton number ratio St/St_o is determined to be of the form :

$$\frac{St}{St_o} = \frac{St_f}{St_o}(1 - \eta\theta) \quad (\text{Equation 3.17})$$

By setting $\theta=0$ in Equation 3.17, the iso-energetic Stanton number ratio St_f/St_o is determined to be :

$$\frac{St_f}{St_o} = \frac{St}{St_o} \quad (\text{Equation 3.18})$$

Now, if St/St_0 is set equal to zero in Equation 3.17, then it becomes :

$$(1 - \eta\theta) = 0 \quad \text{(Equation 3.19)}$$

Rearranging Equation 3.19 subsequently yields :

$$\theta = \frac{1}{\eta} \quad \text{(Equation 3.20)}$$

Therefore, by determining values of St/St_0 at different values of θ , both the adiabatic film cooling effectiveness η and the iso-energetic Stanton number ratio St_f/St_0 can be determined using Equations 3.18 and 3.20.

1. One row of film cooling holes with $m=0.5$

Figure 14 shows Stanton numbers versus Reynolds number for various values of non-dimensional temperature (θ). Also included is the baseline curve for no film injection. At a given value of Reynolds number, St values generally increase as θ decreases. At a particular θ , St values generally decrease with increasing Re , such that all sets of data show similar qualitative trends. With the exception of film cooling data for $\theta=0.0$, all curves show values of St which are lower than the baseline curve.

Figures 15 and 16 show the spanwise variation of η and St_f/St_0 for x/d values of 6.7, 17.2, 33.1, 54.3, 75.4 and 96.6. With the exception of data at x/d of 6.7 and 17.2, these figures demonstrate a uniform distribution in the spanwise direction. At the first two streamwise locations, spanwise variations of η and St_f/St_0 are evident which correspond to concentrations and deficits of injectant, where higher η are associated with larger amounts of injectant.

Figure 17 shows spanwise variations of St/St_0 for x/d values of 6.7, 17.2, 33.1, 54.3, 75.4 and 96.6 for a θ of 1.29. With the exception of data at x/d of 6.7 and 17.2, this figure also shows uniform distributions in the spanwise direction.

2. One row of film cooling holes with $m=1.0$

Figure 18 shows Stanton numbers versus Reynolds number for various values of non-dimensional temperature (θ). Also included is the baseline curve for no film injection. As for the $m=0.5$ data, at a given value of Reynolds number, St values generally increase as θ decreases. At a particular θ , St values generally decrease with increasing Re , such that all sets of data show similar qualitative trends. Most all of the curves show values of St which are higher than the baseline curve.

Figures 19 and 20 show the spanwise variation of η and St_f/St_0 for x/d values of 6.7, 17.2, 33.1, 54.3, 75.4 and 96.6. Data at all x/d in Figure 19 show some periodicity due to deficits and accumulations of injectant. These variations are amplified in Figure 20, where data show less uniformity than when one row of cooling holes with $m=0.5$ is employed. Similar behavior is evident in Figure 21, which shows spanwise variations of St/St_0 for x/d values of 6.7, 17.2, 33.1, 54.3, 75.4 and 96.6 for a θ of 1.21.

3. Two rows of film cooling holes with $m=0.5$

Figure 22 shows Stanton numbers versus Reynolds number for various values of non-dimensional temperature (θ). Also included is the baseline curve for no film injection. As before, at a given value of Reynolds number, St values generally increase as θ decreases. At a particular θ , St values generally decrease

with increasing Re . With the exception of film cooling data for $\theta=0.0$, all curves show values of St which are lower than the baseline curve.

Figures 23 and 24 show spanwise variations of η for x/d values of 6.7, 17.2, 33.1, 54.1, 75.4 and 96.6, determined using either five or six sets of η versus θ data. This was done to show that removal of data at one θ does not affect η and St_f/St_0 magnitudes and distributions. With the exception of data at x/d of 6.7 and 17.2, these figures demonstrate fairly uniform spanwise distributions. At the first two streamwise locations, spanwise variations of η and St_f/St_0 are evident which correspond to injectant accumulations and deficits.

Figures 25 and 26 show spanwise variations of St_f/St_0 for x/d values of 6.7, 17.2, 33.1, 54.1, 75.4 and 96.6, determined using five and six sets of data, respectively. With the exception of data at x/d of 6.7 and 17.2, spanwise uniform variations are evident. Similar trends are evident in Figure 27, which shows distributions of St/St_0 for x/d values of 6.7, 17.2, 33.1, 54.3, 75.4 and 96.6 for a $\theta = 1.66$.

Figures 28 - 51 show plots of St/St_0 versus θ for three different values of Z and for x/d values of 33.1, 54.3, 75.4 and 96.6. These plots are presented in both a compact and expanded form to illustrate the linear relationship between St/St_0 and θ , and to show how data can be used to determine the X-axis intercept which is the inverse of the adiabatic film cooling effectiveness (η).

Figures 28 through 35 show the variation of St/St_0 versus θ for the Z value of 0.0 cm. Figures 36 through 43 show the variation of St/St_0 versus θ for the Z value of -6.35 cm. Figures 44 through 51 show the variation of St/St_0 versus θ for the Z value of +6.35 cm.

4. Comparison of film cooling hole configurations

Figure 52 shows spanwise averaged values of the adiabatic film cooling effectiveness (η) as a function of x/d for the various configurations and blowing ratios used. The one row with $m=0.5$ (Yoshida) data is taken from Reference 9. The plot demonstrates that the configuration with the highest η is the one with two rows of compound angle injection cooling holes with a blowing ratio of $m=0.5$. The configuration with the lowest η is the one with one row of compound angle injection cooling holes with a blowing ratio of $m=1.3$ [Ref. 10]. This plot also shows that the two row η data is unaffected by the use of either five or six sets of St/St_0 data.

Figure 53 shows η as a function of x/s where s is the spanwise spacing between injection holes. This plot shows that data sets with about the same value of s collapse together. For the one row data from the present study, η generally decreases with m at a particular value of x/s .

Figure 54 shows variations of St_f/St_0 versus x/d for the various configurations used. These data all lie between 1.0 and 1.2 for all x/d between 0 and 100.

C. FIVE HOLE PRESSURE PROBE SURVEYS

Distributions of streamwise mean velocity and total pressure are presented in Figures 55 - 72. These surveys were obtained using the five hole pressure probe described in Chapter II. For each survey, the probe is positioned at 400 different positions in the spanwise plane at x/d values of 10.2, 45.8 and 86.8. The freestream velocity, U_∞ , is maintained at 10 m/s for all tests. The three configurations surveyed are : (1) one row of compound angle injection cooling

holes with a blowing ratio of $m=0.5$, (2) one row of compound angle injection cooling holes with a blowing ratio of $m=1.0$ and (3) two rows of compound angle injection cooling holes with a blowing ratio of $m=0.5$.

1. One row of film cooling holes with $m=0.5$

Figures 55 - 57 present streamwise velocity distributions and Figures 58 - 60 show total pressure distributions downstream of one row of compound angle injection cooling holes with a blowing ratio of $m=0.5$ at x/d values of 10.2, 45.8 and 85.6. Figures 55 and 58 include arrows to indicate the positions and orientations of the film cooling holes. All distributions show that the flow is spanwise periodic near the wall as a result of film injection at discrete locations. As one moves downstream, the boundary layer becomes thicker and the quantitative variations near the wall become less.

2. One row of film cooling holes with $m=1.0$

Figures 61 - 63 present streamwise velocity distributions and Figures 64 - 66 show distributions of total pressure downstream of one row of compound angle injection cooling holes with a blowing ratio of $m=1.0$ at x/d values of 10.2, 45.8 and 85.6. Figures 61 and 64 include arrows to indicate the positions and orientations of the film cooling holes. As for the $m=0.5$ data, the flow is spanwise periodic near the wall. Here, however, the injectant has a more intense effect on boundary layer behavior away from the wall, especially for $x/d=45.8$ and 86.8.

3. Two rows of film cooling holes with $m=0.5$

Figures 67 - 69 present the streamwise velocity distributions and Figures 70 - 72 show total pressure distributions downstream of two rows of compound angle injection cooling holes with a blowing ratio of $m=0.5$ at x/d values of 10.2,

45.8 and 85.6. As before, Figures 67 and 70 include arrows to illustrate positions and orientations of the injection holes. Figures 67 and 70 show spanwise periodicity near the wall spaced twice as frequently as when one row is employed. Six velocity deficits are apparent near the wall. As one moves downstream, the boundary layer shows greater spanwise uniformity away from the wall than obtained from the other two injection configurations which utilize half as many injection locations.

D. INJECTANT DISTRIBUTIONS

Figures 73 - 81 show the injectant distributions as determined from surveys of mean temperature. For each injection configuration, data are given for three x/d locations of 10.2, 45.8 and 86.8. Results for three different configurations are presented : (1) one row of compound angle injection cooling holes with a blowing ratio of $m=0.5$, (2) one row of compound angle injection cooling holes with a blowing ratio of $m=1.0$, and (3) two rows of compound angle injection cooling holes with a blowing ratio of $m=0.5$.

Procedures to determine injectant distributions were developed by Ligrani, et al [Ref. 4]. Injection distributions are correlated to mean temperature distributions, measured when the injectant is heated to 50 degrees Celsius without providing any heat to the test plate. Thus, because the injectant is the only source of thermal energy (relative to freestream flow), higher temperatures (relative to freestream temperatures) generally indicate greater amounts of injectant. The temperature fields in Figures 73 - 81 are therefore given as $(T-T_{\infty})$, and as such, show how injectant accumulates and is rearranged mostly as a result of convective processes from the boundary layer. These temperature variations are

different from ones which would exist if the wall were heated because of different distributions of turbulent diffusion of injectant heat. However, in spite of this, a good qualitative indication of injectant distributions is obtained because, compared to convection, turbulent diffusion is of secondary importance in organizing relative positions of injectant concentrations.

1. One row of film cooling holes with $m=0.5$

Figures 73 - 75 show injectant distributions at x/d values of 10.2, 45.8 and 86.8 downstream of one row of compound angle injection cooling holes (5 holes) with a blowing ratio of $m=0.5$. Also included in the first figure are arrows illustrating the locations and orientation of film cooling holes. Here, injectant distributions are spanwise periodic at Z locations of -9 cm to -7 cm, -1.5 cm to 0.5 cm, and 5.5 cm to 7.5 cm. There is little injectant between these locations and thus, protection from film cooling is periodically minimal. Injectant distributions appear to be about the same from the different holes with distorted non-circular distributions, unlike the circular distributions associated with simple angle injection systems [Ref. 4].

Figure 74 shows that injectant distributions for x/d of 45.8 are more diffuse than at x/d of 10.2, but not diffuse enough to merge. These trends continue in Figure 75 for x/d of 86.8, where injectant continues to spread laterally and away from the wall as it is convected downstream.

2. One row of film cooling holes with $m=1.0$

Figures 76 - 78 show injectant distributions at x/d values of 10.2, 45.8 and 86.8 downstream of one row of compound angle injection cooling holes (5 holes) with a blowing ratio of $m=1.0$. As for the $m=0.5$ data, the first figure contains arrows illustrating the locations and orientation of film cooling holes.

Here, injectant distributions are spanwise periodic at Z locations of -9.5 cm to -8.0 cm, -2.5 cm to -1.0 cm, and 4.5 cm to 6.5 cm. There is little injectant between these locations and thus, protection from film cooling is periodically minimal. Injectant distributions appear to be about the same from the different holes with distorted non-circular distributions and slightly larger than the one row of film cooling holes with $m=0.5$ data.

Figure 77 shows that injectant distributions for x/d of 45.8 are more diffuse than at x/d of 10.2, but once again not diffuse enough to merge. However, the injectant, in addition to spreading laterally, has now begun to move away from the wall which lessens the protection normally provided by film cooling. These trends continue in Figure 78 for x/d of 86.8, where injectant continues to spread laterally and away from the wall as it is convected downstream.

3. Two rows of film cooling holes with $m=0.5$

Figures 79 - 81 show injectant distributions at x/d values of 10.2, 45.8 and 86.8 downstream of two rows of compound angle injection cooling holes (10 holes) with a blowing ratio of $m=0.5$. As before, the figure for the first downstream location contains arrows illustrating the locations and orientation of film cooling holes. Here, injectant distributions are spanwise periodic at Z locations of -12.7 cm to -11.2 cm, -9.0 cm to -7.0 cm, -5.5 cm to -4.0 cm, -2.0 cm to 0.5 cm, 1.5 cm to 3.5 cm, and 5.3 cm to 7.5 cm. Injectant distributions appear to be about the same, not for every hole, but every other hole because cooling holes from the two rows are staggered as shown in Figure 3.

Figure 80 shows that injectant distributions for x/d of 45.8 are more diffuse than at x/d of 10.2 and that injectant from neighboring holes is merging

together. These trends continue in Figure 81 for x/d of 86.8, where injectant continues to spread laterally away from the wall as it is convected downstream.

E. FLOW VISUALIZATION

Flow visualization results are presented in Figures 82-87. Photographs show injectant from either one or two rows of compound angle injection cooling holes with blowing ratios of 0.5, 1.0 or 1.5. In the background of the photographs, a 1/16 inch, black fiberboard is evident, which is placed on top of the test surface. In each photograph, the flow is moving from top to bottom. The three horizontal lines, from top to bottom, correspond to x/d values of 6.7, 17.2 and 33.1, respectively. The vertical lines are spaced one inch apart. The test surface spanwise centerline is annotated with a draftsman's centerline symbol.

All of the photographs indicate that the injectant flow is turbulent. Figures 85-87 show that the configuration of two rows of film cooling holes provides better coverage than is available from one row of film cooling holes (Figures 82-84). The photographs also show that injectant flow becomes more aligned in the streamwise direction as the blowing ratio is decreased.

IV. SUMMARY AND CONCLUSIONS

Experimental results are presented which describe the development and structure of turbulent boundary layer flow downstream of single and double rows of film-cooling holes with compound angles. The film-cooling holes are inclined at angles of 30 degrees with respect to the test surface when projected into the spanwise/normal (Y-Z) planes, and at angles of 35 degrees with respect to the test surface when projected into the streamwise/normal (X-Y) planes. Three configurations are used : (1) one row of film-cooling holes with a blowing ratio of $m=0.5$, (2) one row of film-cooling holes with a blowing ratio of $m=1.0$ and (3) two staggered rows of film-cooling holes with a blowing ratio of $m=0.5$.

Results from heat transfer measurements show that, for a given Reynolds number, Stanton numbers generally increase as θ decreases, and at a particular θ , Stanton values generally decrease with increasing Reynolds numbers for all sets of data. The highest η values are obtained when two rows of compound angle injection cooling holes are employed with a blowing ratio of $m=0.5$. The lowest η values are obtained when one row of compound angle injection cooling holes is used with a blowing ratio of $m=1.0$. η values generally decrease with blowing ratio at a particular x/s , where s is the spanwise spacing between injection holes.

Streamwise mean velocity and total pressure distributions indicate the flow to be spanwise periodic near the wall as a result of the discrete nature of the film injection locations. When one row of film cooling holes with a blowing ratio of $m=1.0$ is employed, the injectant has a more intense effect on boundary layer behavior away from the wall than when $m=0.5$ is used. When two rows of film cooling holes with $m=0.5$ are employed, the boundary layer shows greater

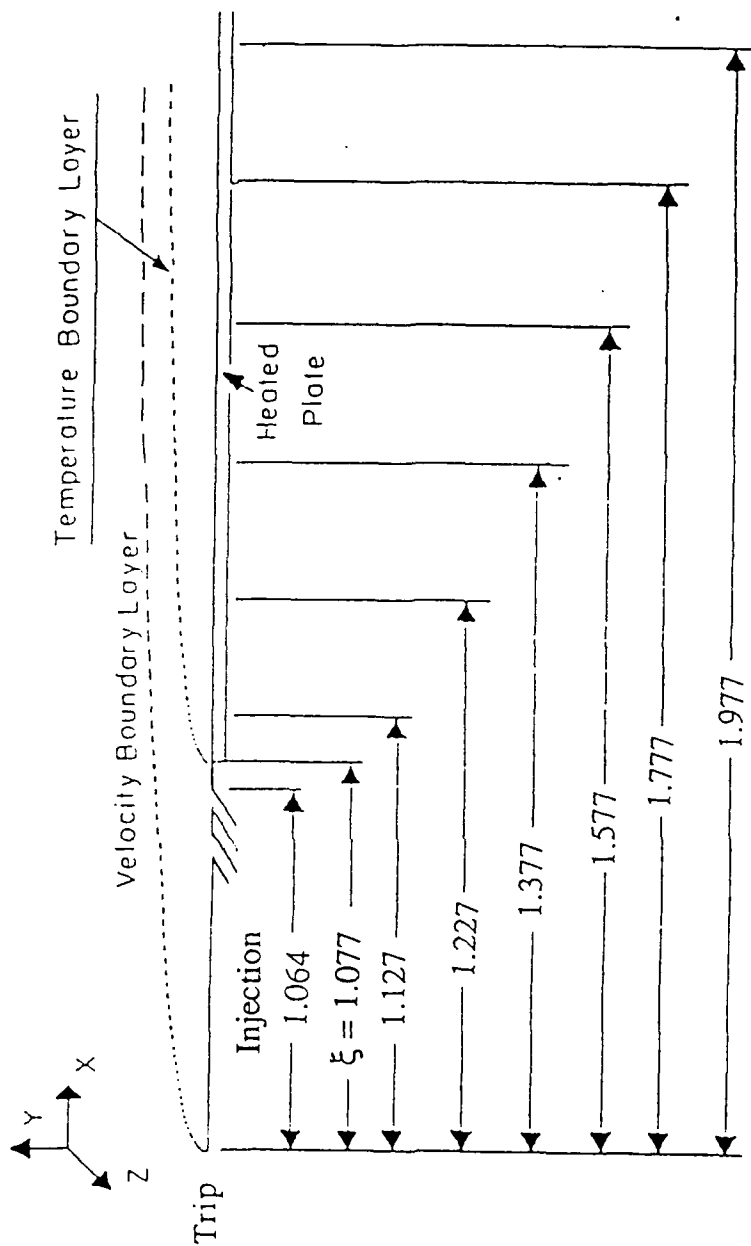
uniformity away from the wall than obtained with the other two configurations which utilize half as many injection holes.

Injectant distributions in spanwise/normal planes are spanwise periodic and non-circular. As the boundary layer convects downstream, injectant spreads laterally and normal to the wall. When one row of film cooling holes with $m=1.0$ is employed, most of the injectant moves away from the wall which evidences a decrease in the protection normally provided by film cooling. When two rows of film cooling holes are employed with $m=0.5$, injectant from neighboring holes merges together as the boundary layer convects downstream.

APPENDIX A

FIGURES

Appendix A contains all of the figures generated for this thesis. These figures include the test set-up, hole configurations, plots of Stanton numbers versus Reynolds numbers and spanwise plots of velocity, pressure and temperature for the three configurations used. Flow visualization pictures are also included for all configurations.



ALL DIMENSIONS IN METERS

Figure 1. Test Section Coordinate System

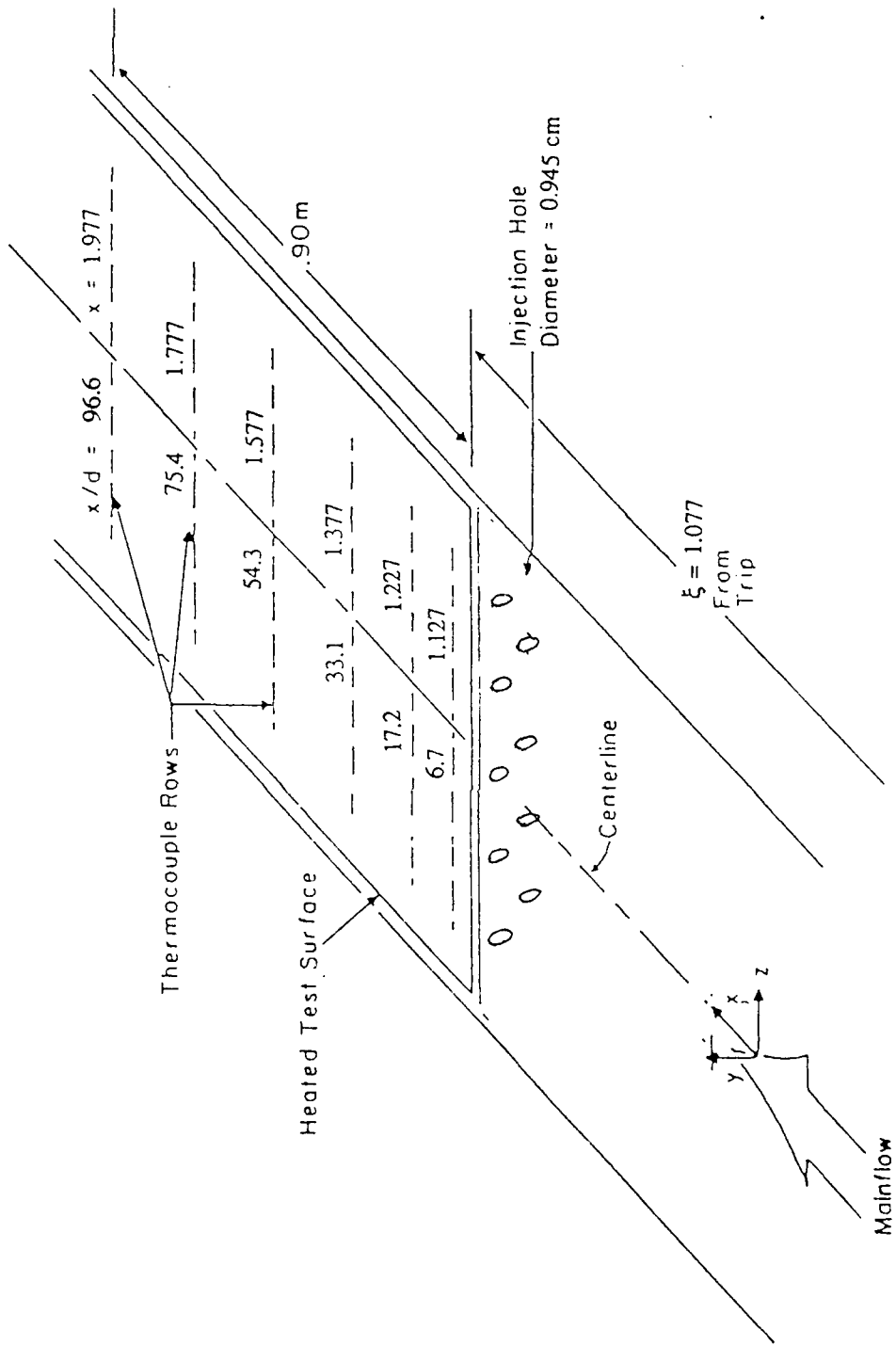


Figure 2. Top View Schematic of Wind Tunnel Test Section

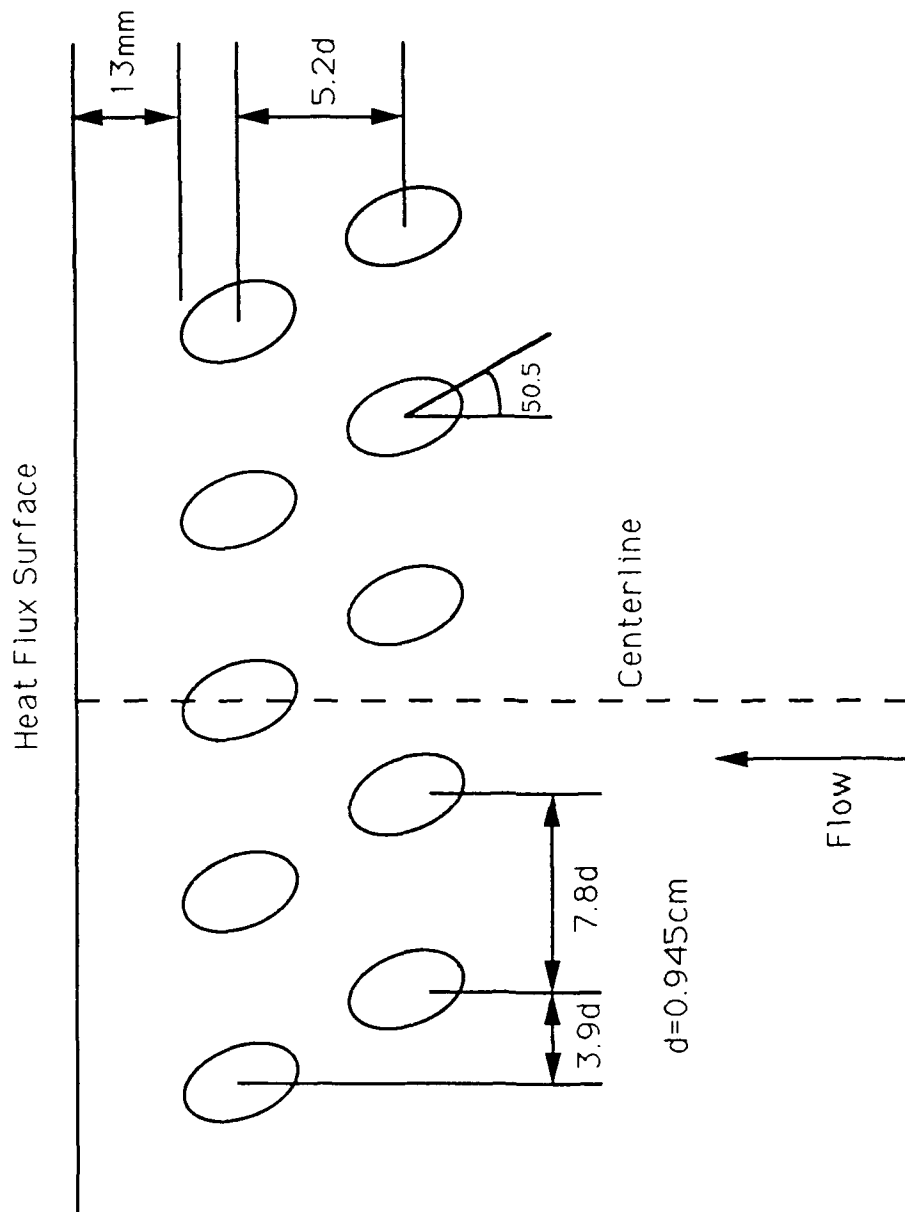


Figure 3. Injection Hole Configuration

Cd vs Reynolds No.

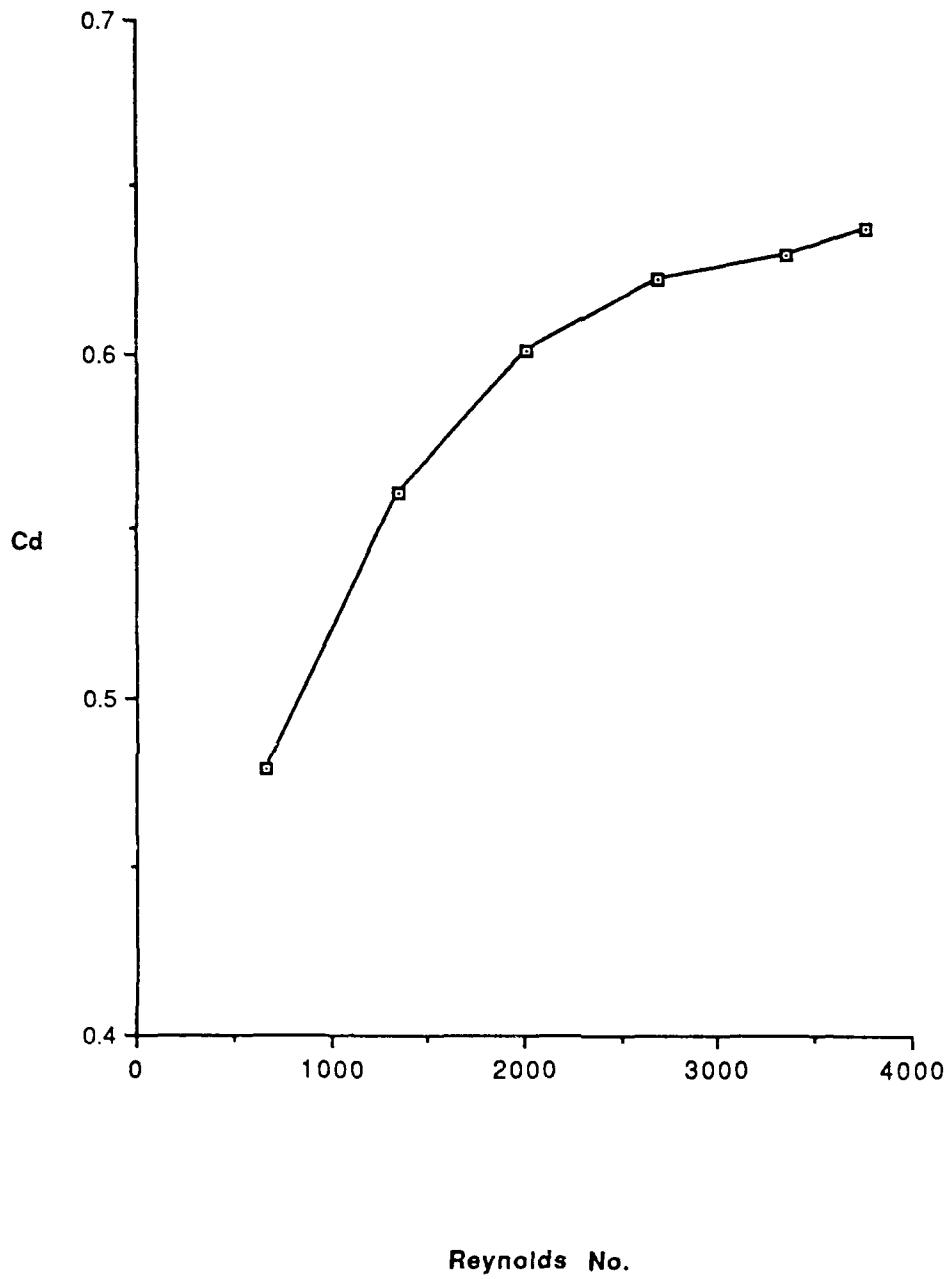


Figure 4. Coefficient of Discharge (C_d) versus Reynolds number for Injection System

T injection vs T plenum

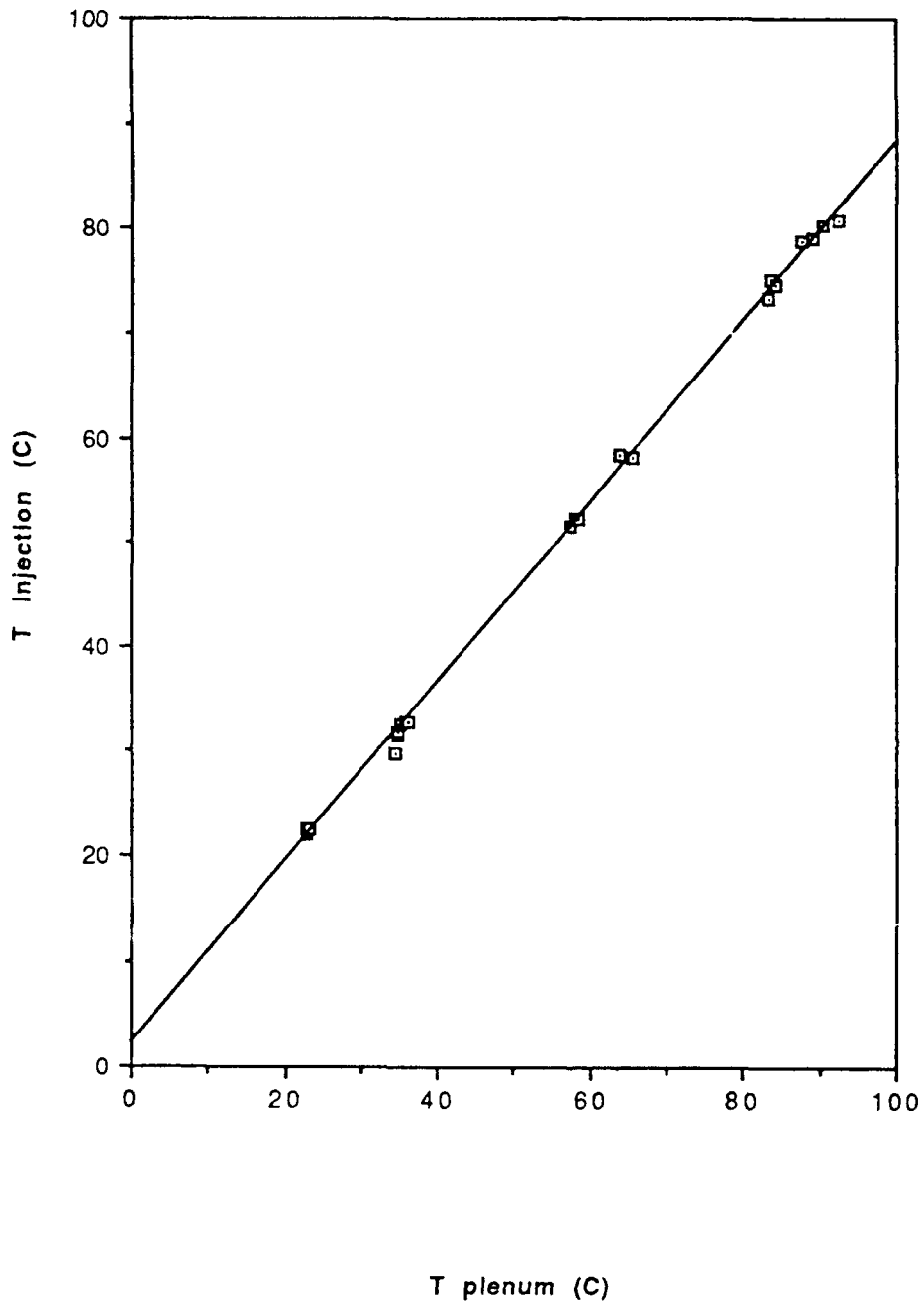


Figure 5. Injectant Temperature versus Plenum Temperature

Stanton No. vs Reynolds No.

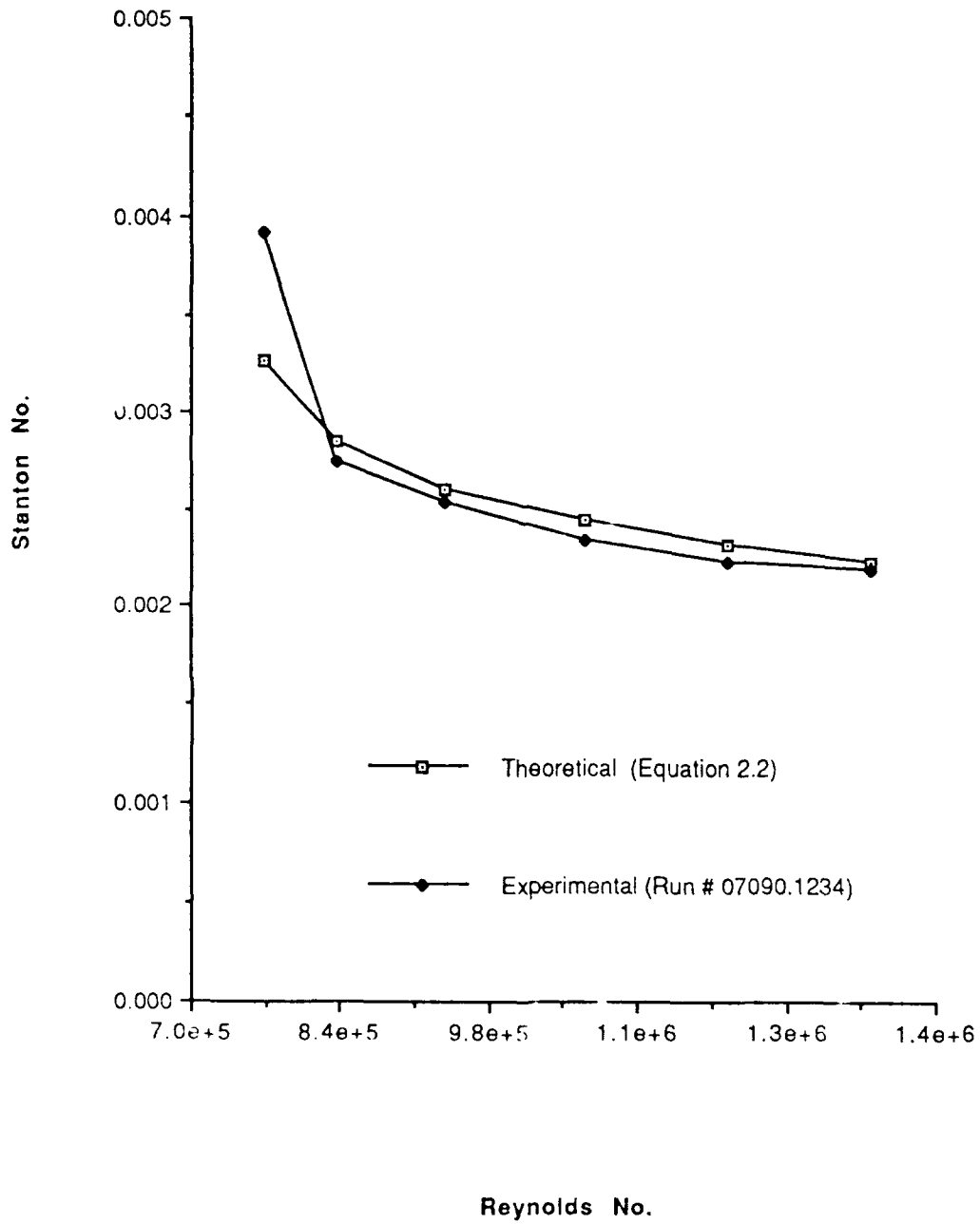


Figure 6. Stanton number comparison between Exact Solution and Experimental Measurements

U vs Y

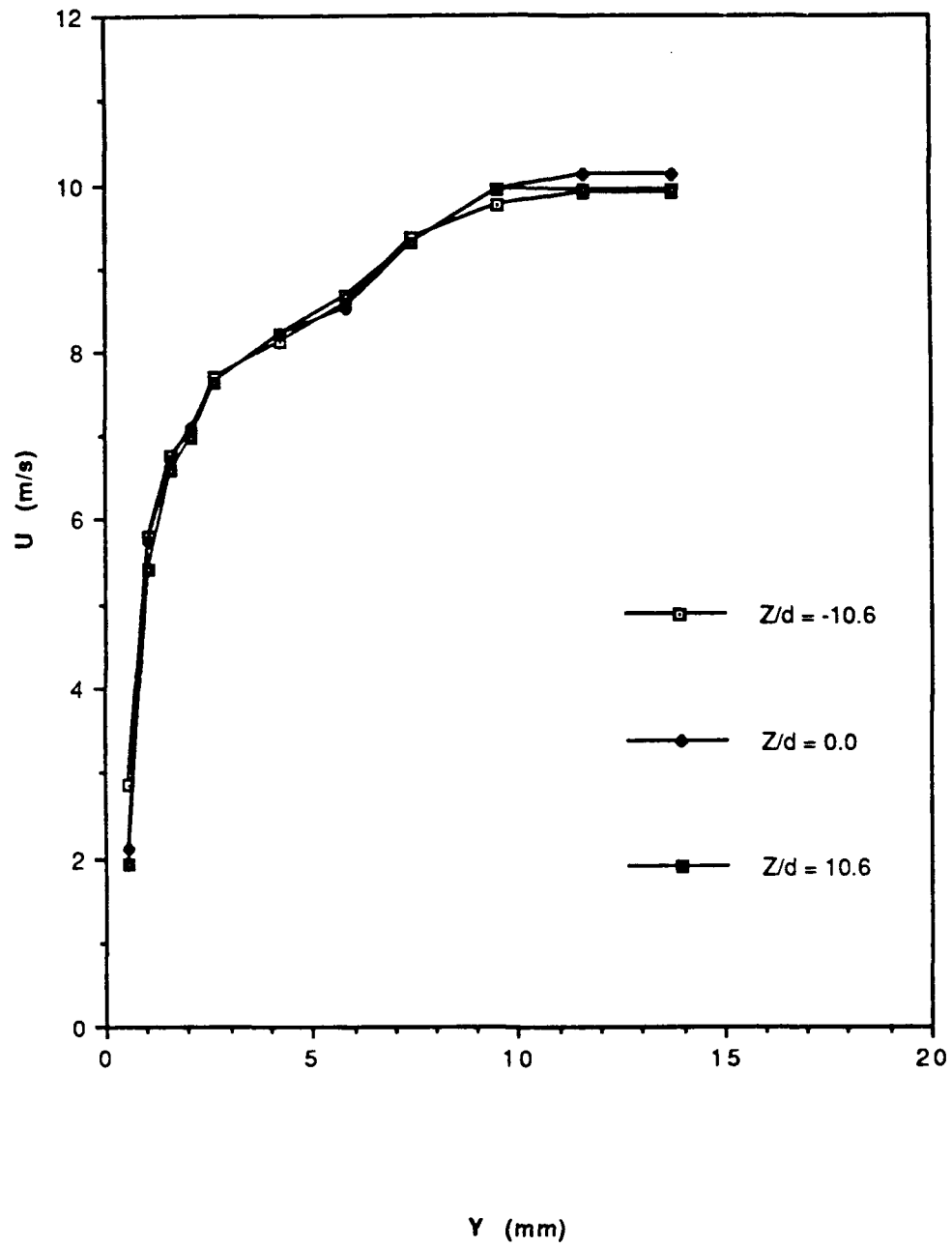


Figure 7. Mean Velocity (U) versus Distance from the wall (Y)

U/U_{inf} vs Y / δ

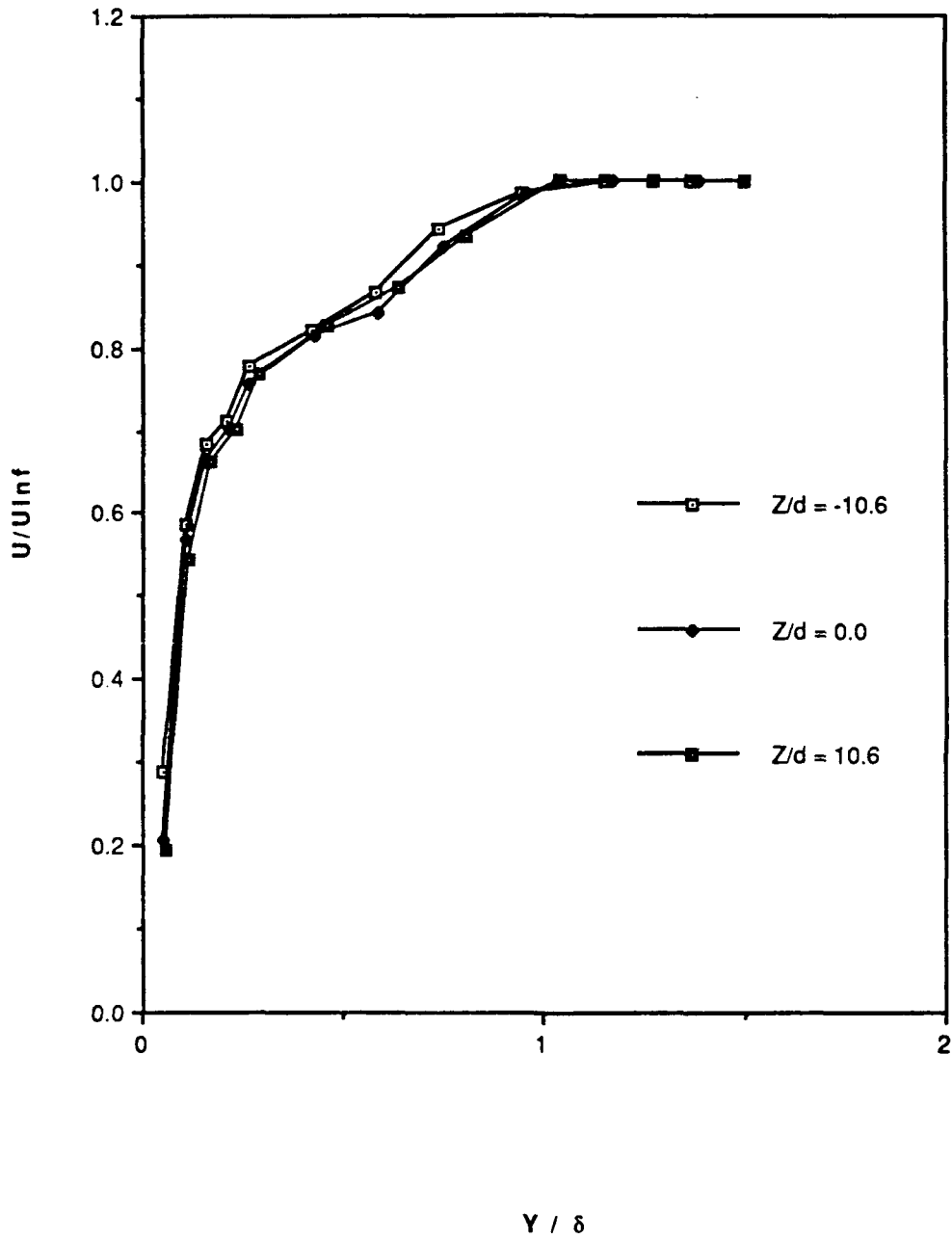


Figure 8. Normalized Mean Velocity (U/U_{∞}) versus Normalized Height (Y/δ)

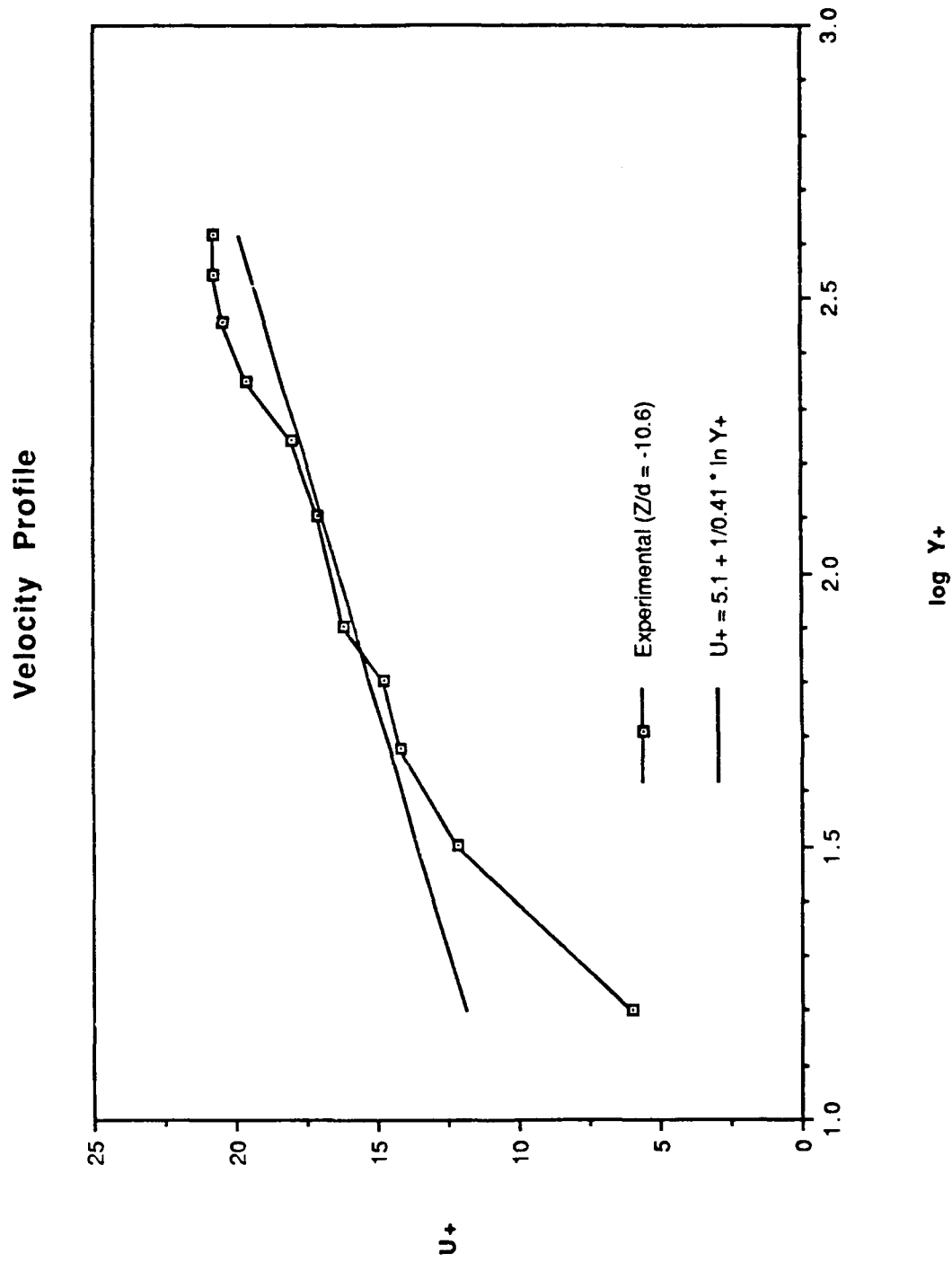


Figure 9. Velocity Profile for $Z/d=-10.6$

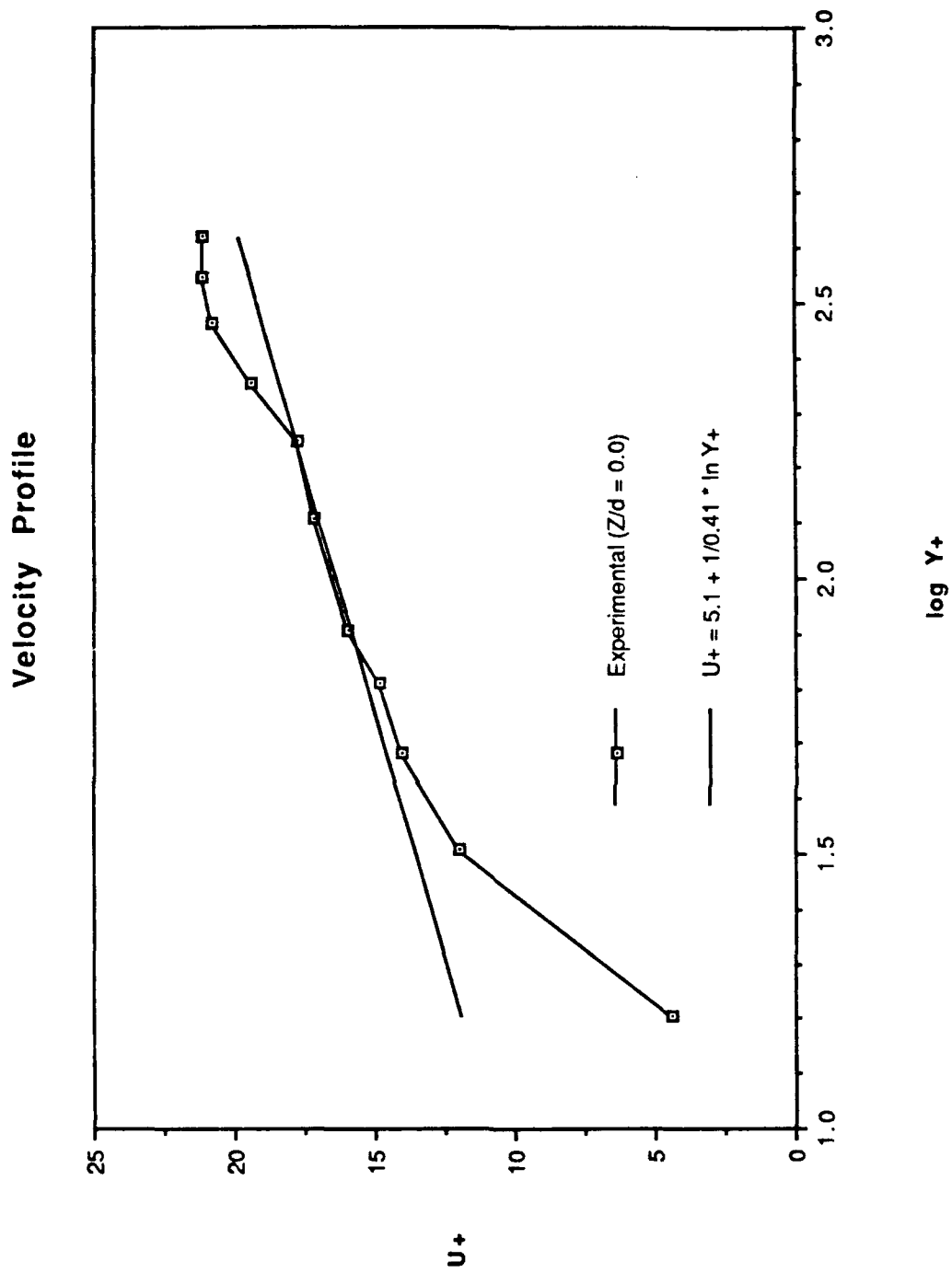


Figure 10. Velocity Profile for $Z/d=0.0$

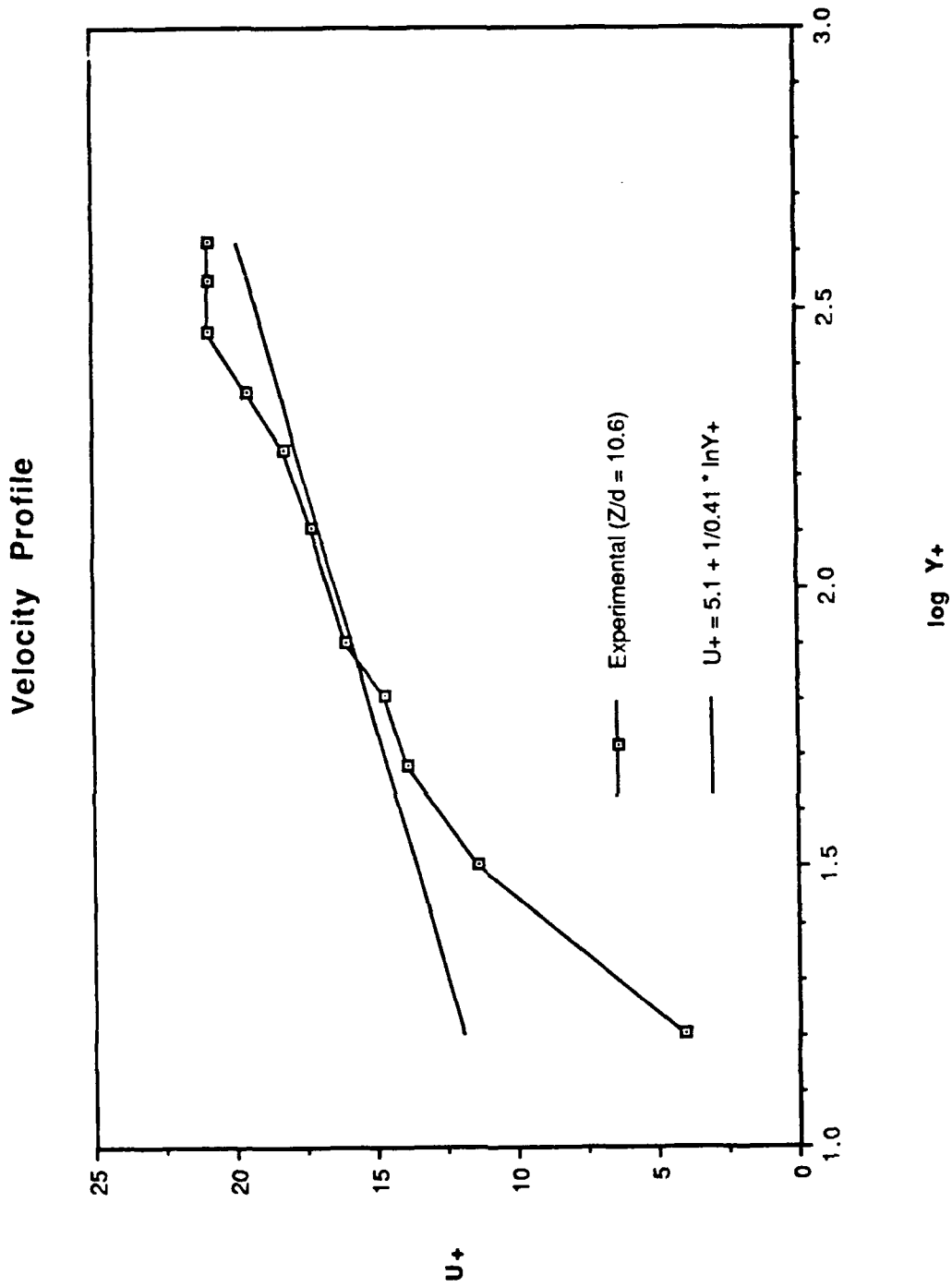


Figure 11. Velocity Profile for $Z/d=10.6$

U' / U_{inf} vs Y / δ

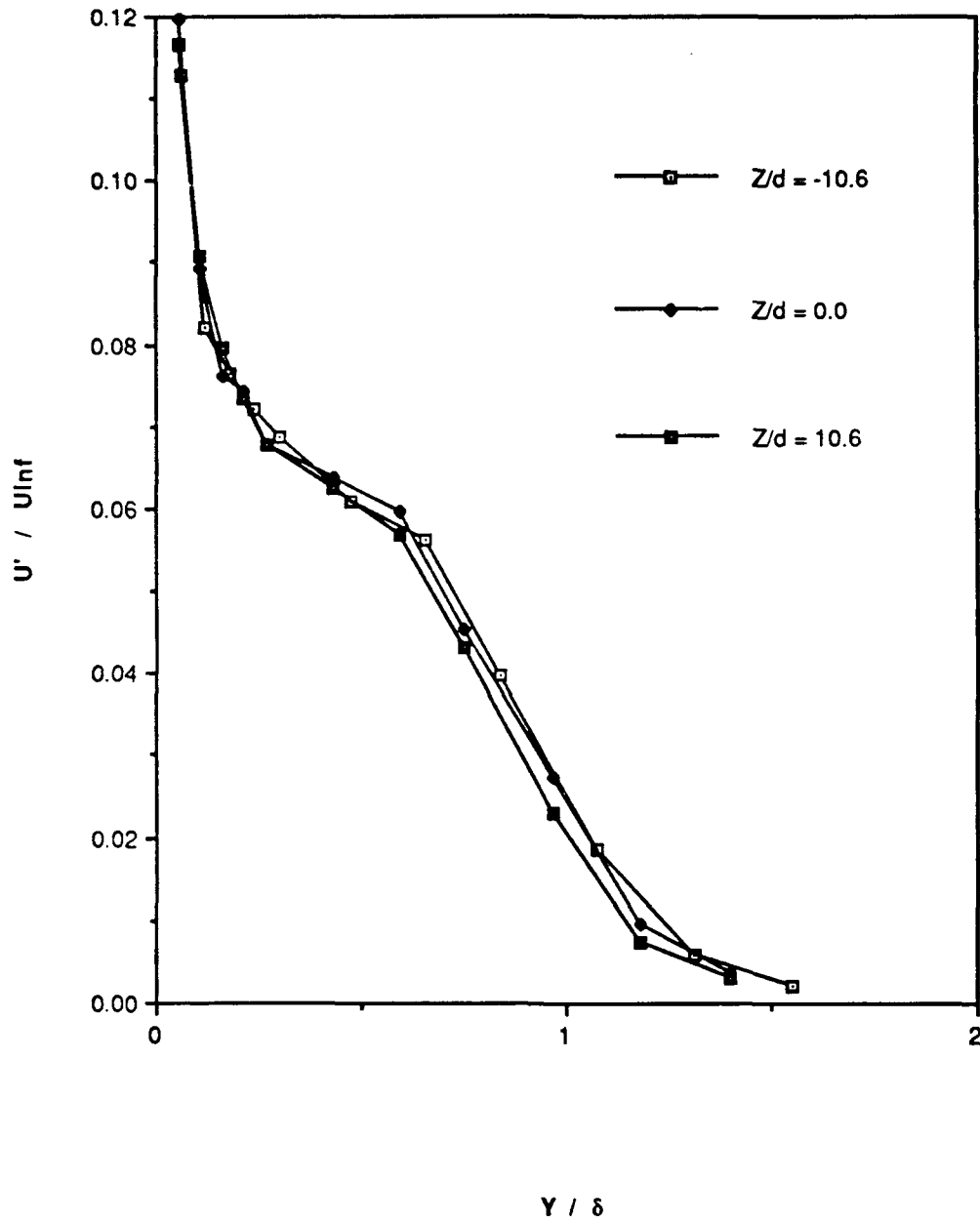


Figure 12. Normalized Longitudinal Turbulence Intensity (U'/U_{inf}) versus Normalized Height (Y/δ)

U' / U_{τ} vs Y / δ

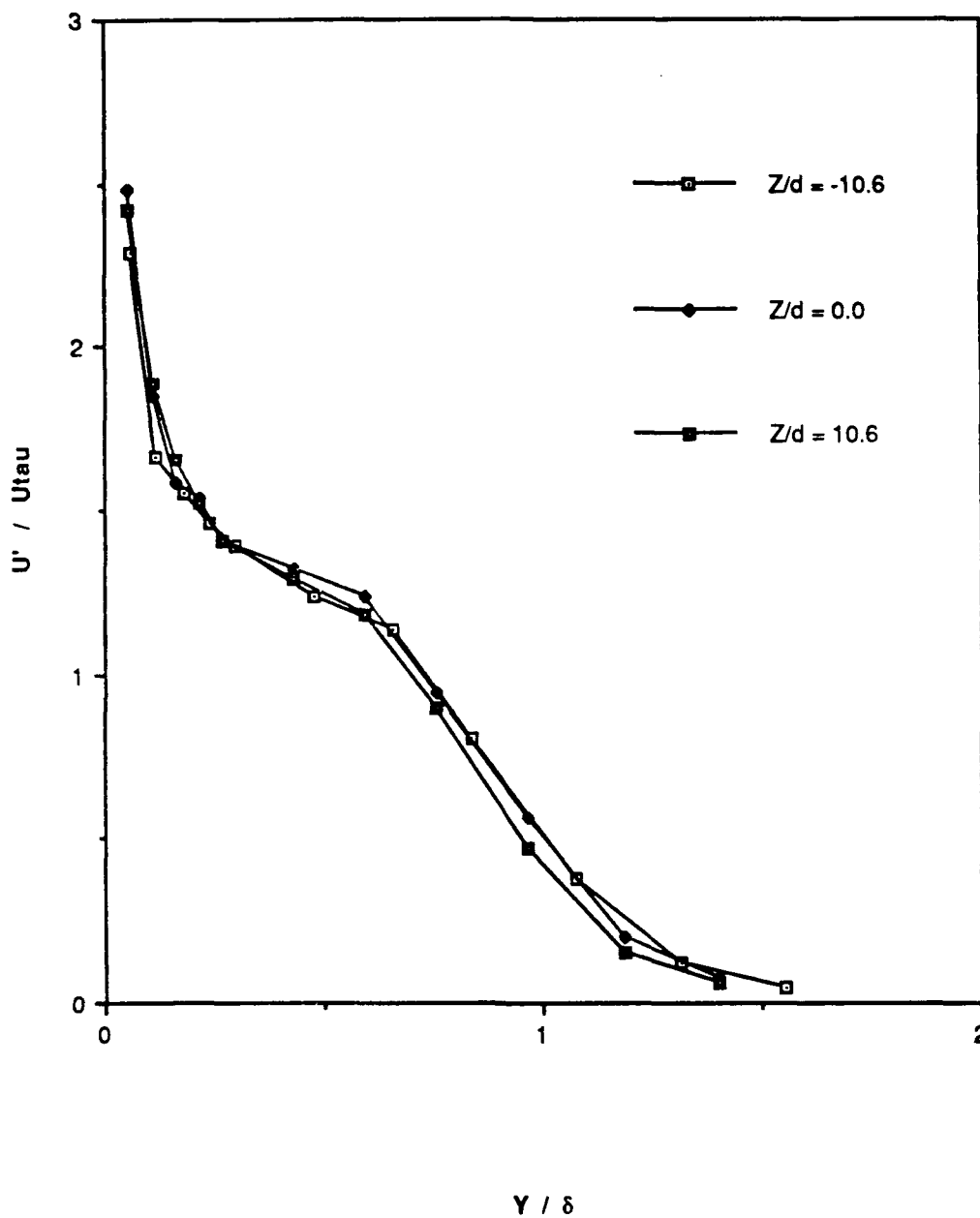


Figure 13. Normalized Longitudinal Turbulence Intensity (U'/U_{τ}) versus Normalized Height (Y/δ)

1 row $m=0.5$

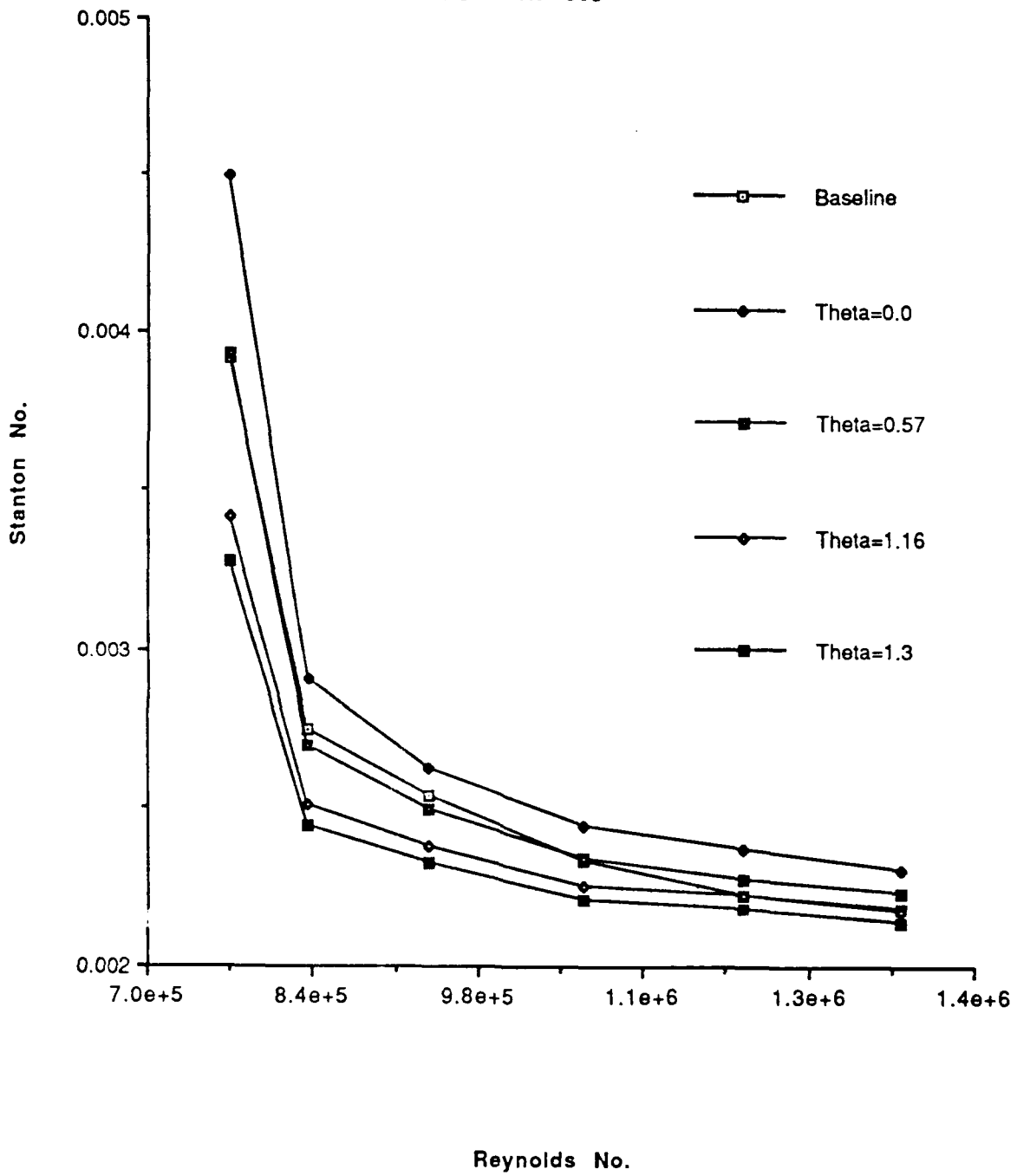


Figure 14. Stanton number (St) comparison, 1 row $m=0.5$

FILM-COOLING EFFECTIVENESS

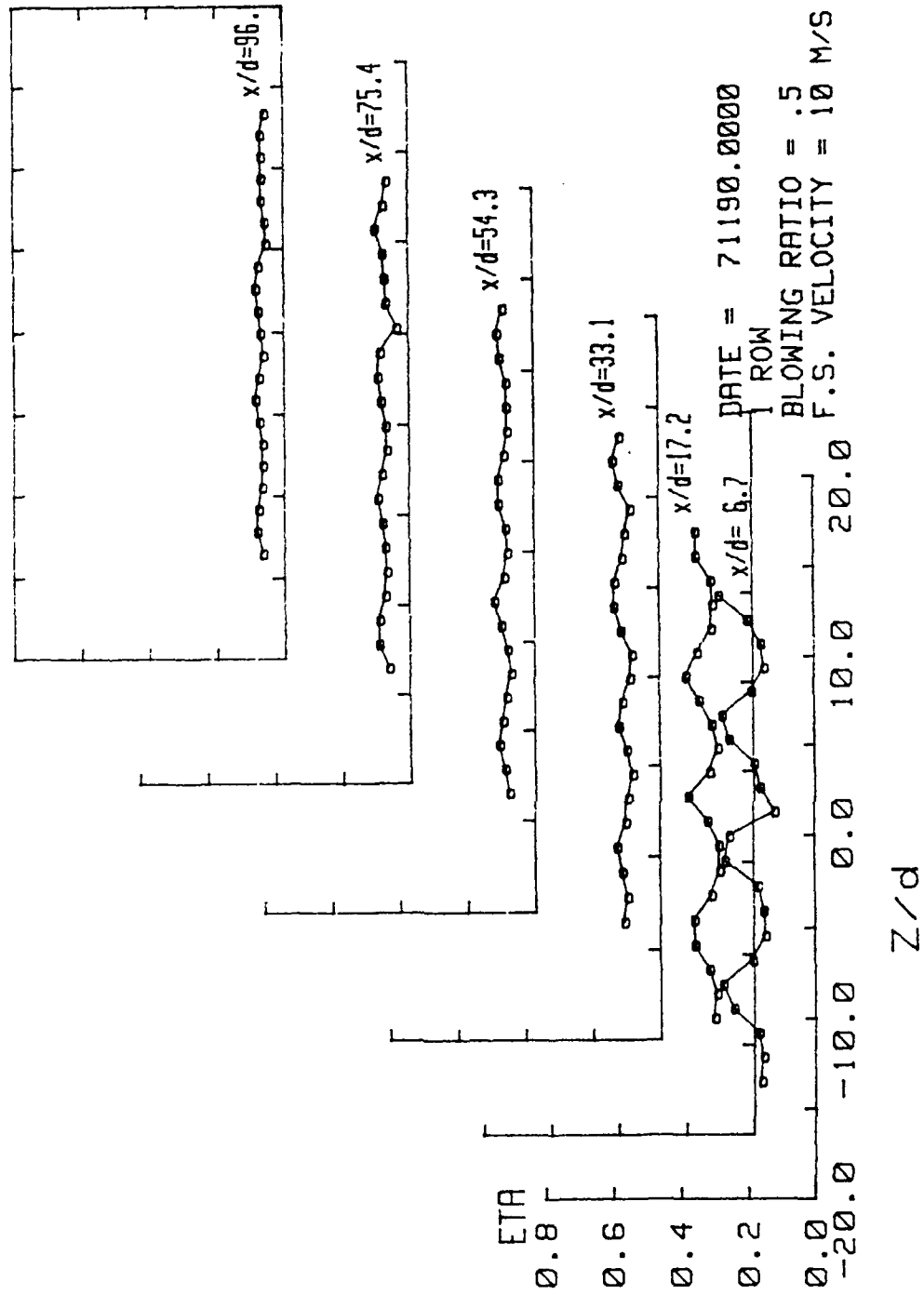


Figure 15. Spanwise Variation of η , 1 row $m=0.5$

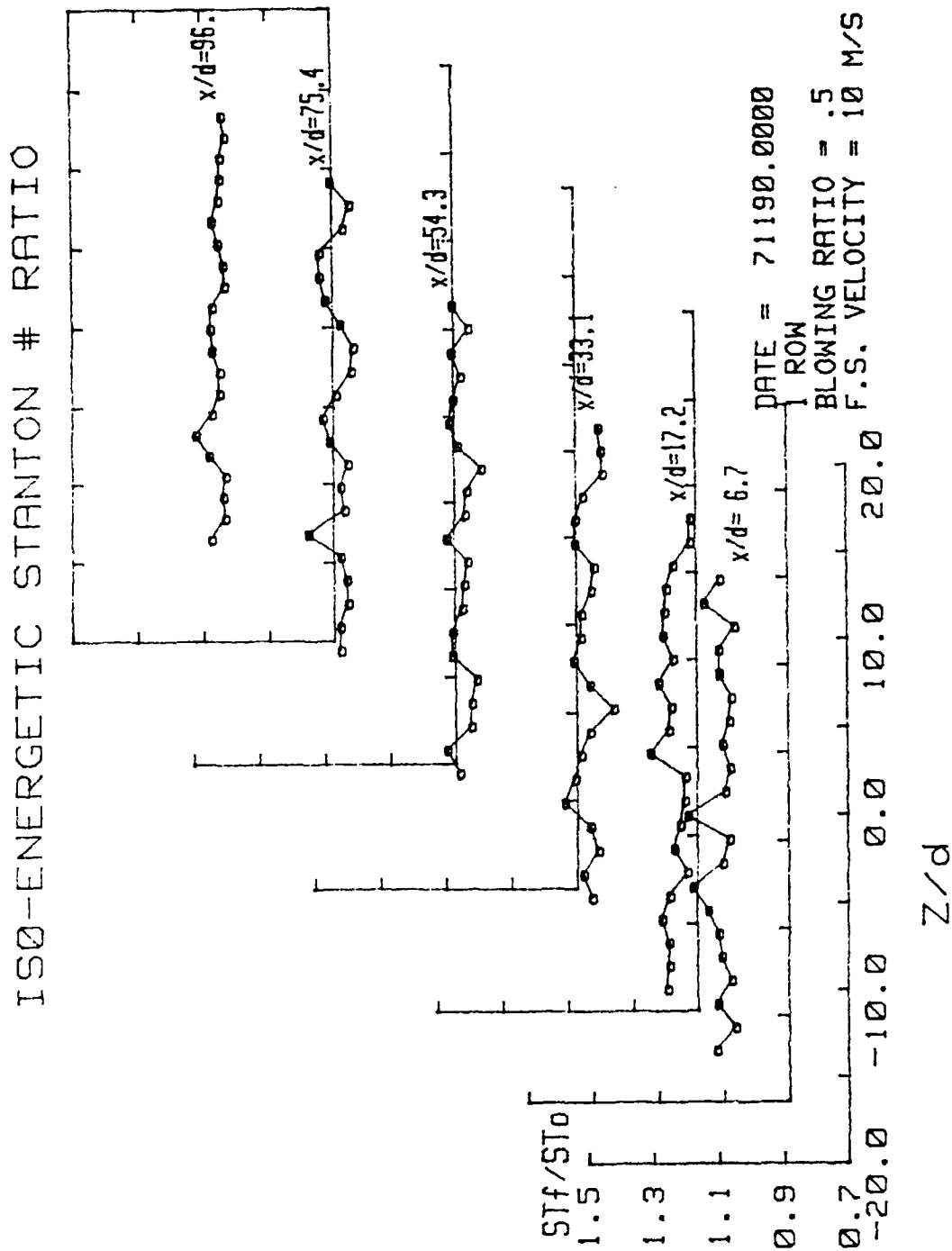


Figure 16. Spanwise Variation of St_f/St_0 , 1 row $m=0.5$

STANTON NUMBER RATIOS

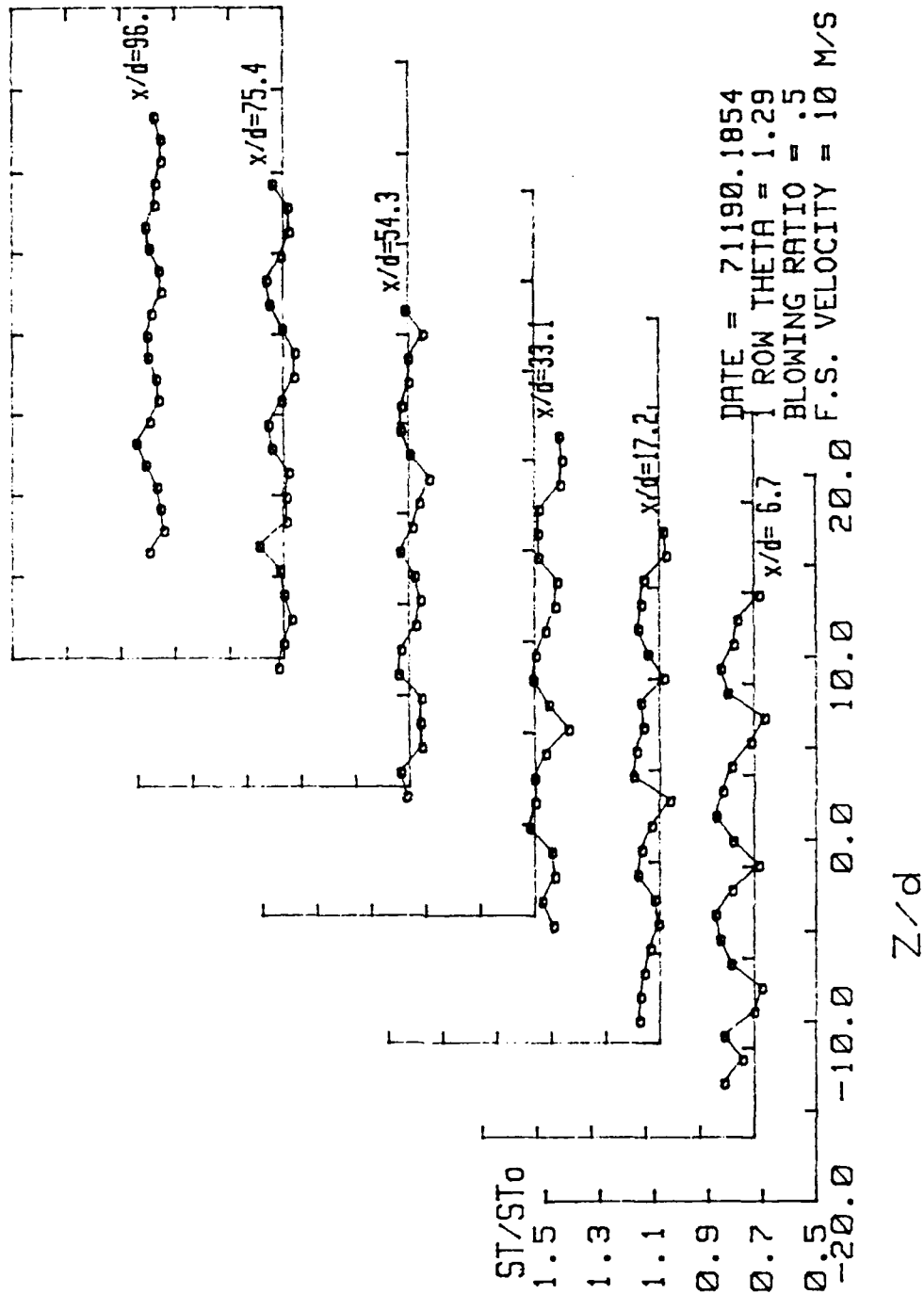


Figure 17. Spanwise Variation of St/St_0 , 1 row $m=0.5$, $\theta=1.29$

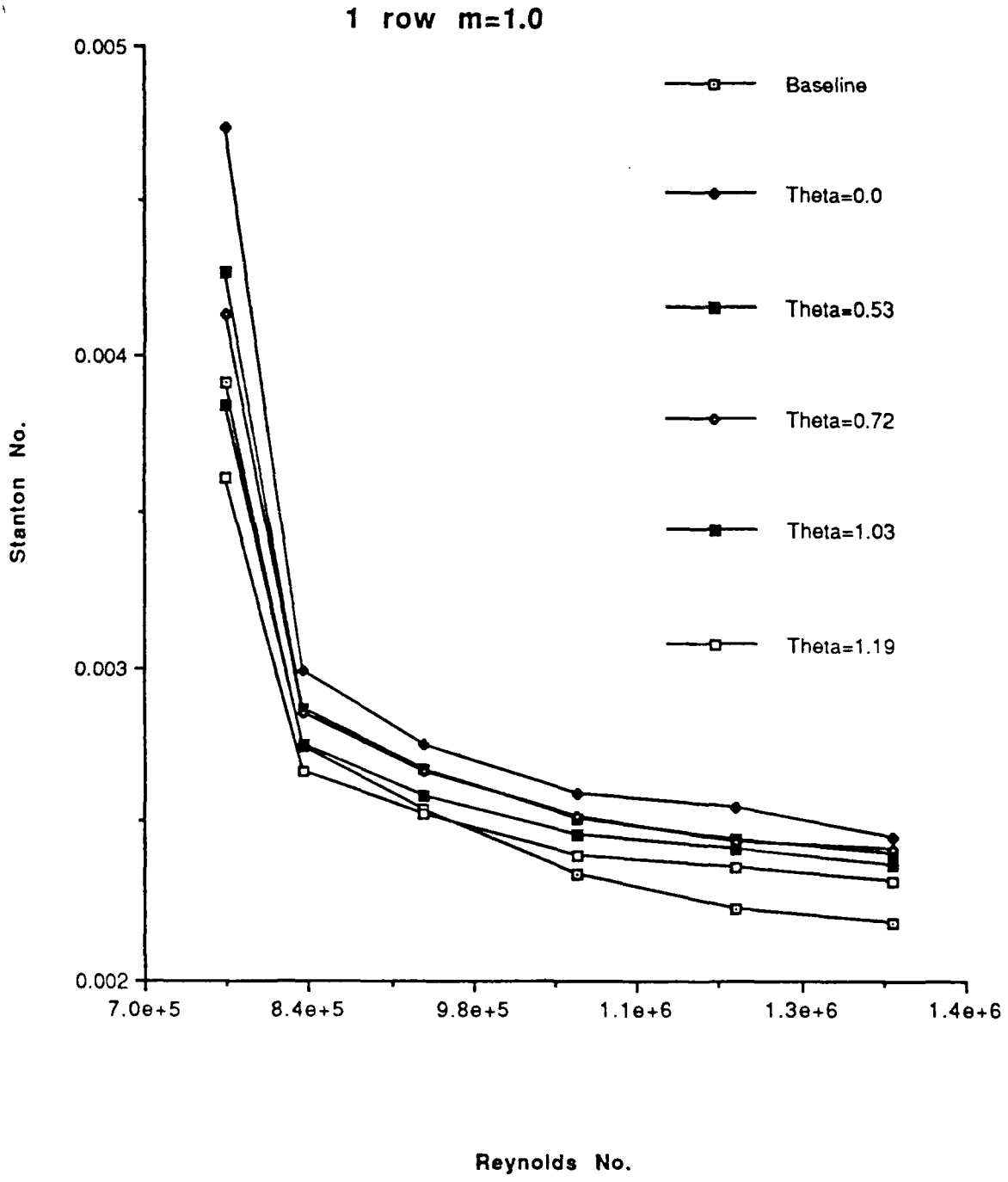


Figure 18. Stanton number (St) comparison, 1 row m=1.0

FILM-COOLING EFFECTIVENESS

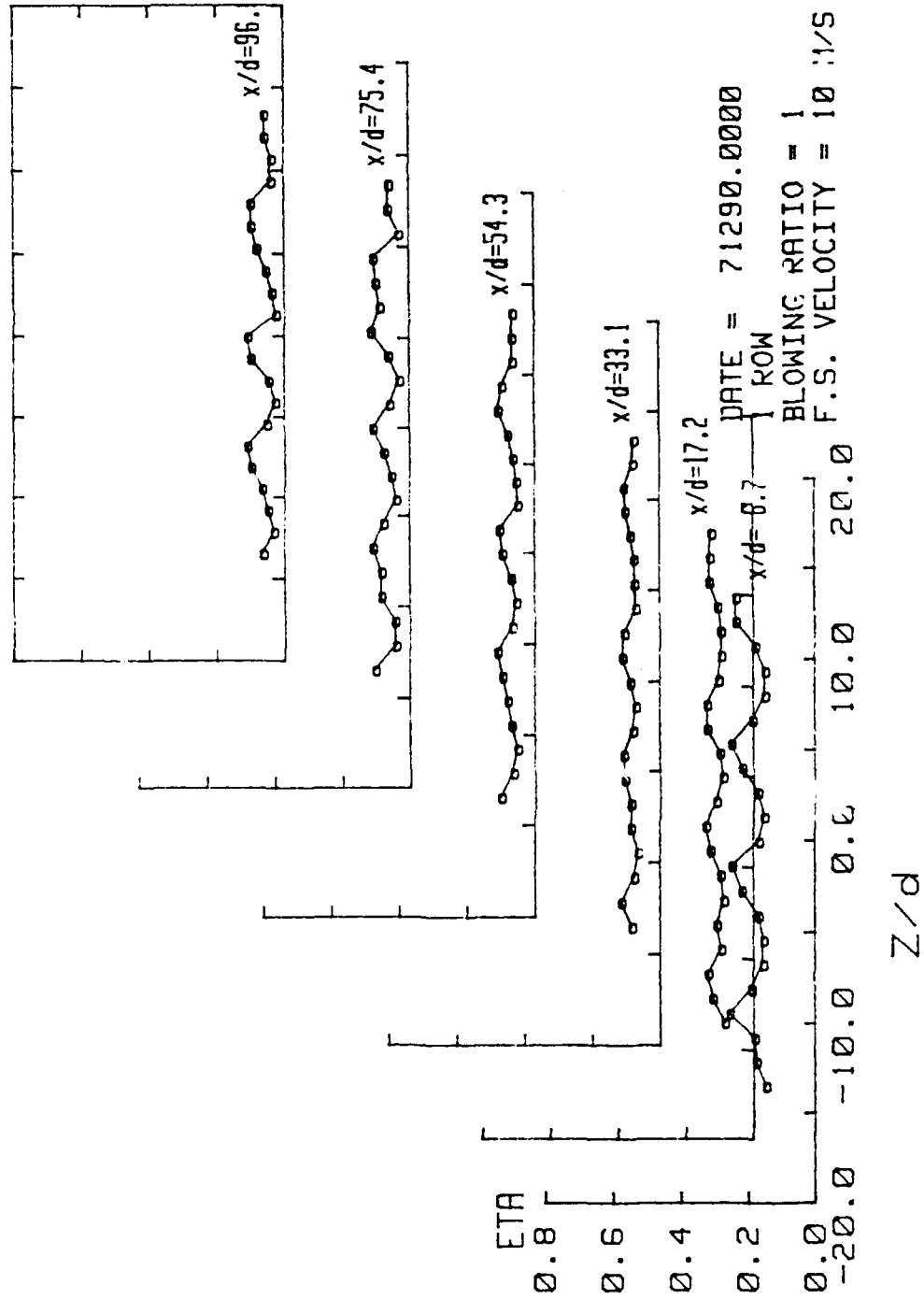


Figure 19. Spanwise Variation of η , 1 row $m=1.0$

ISO-ENERGETIC STANTON # RATIO

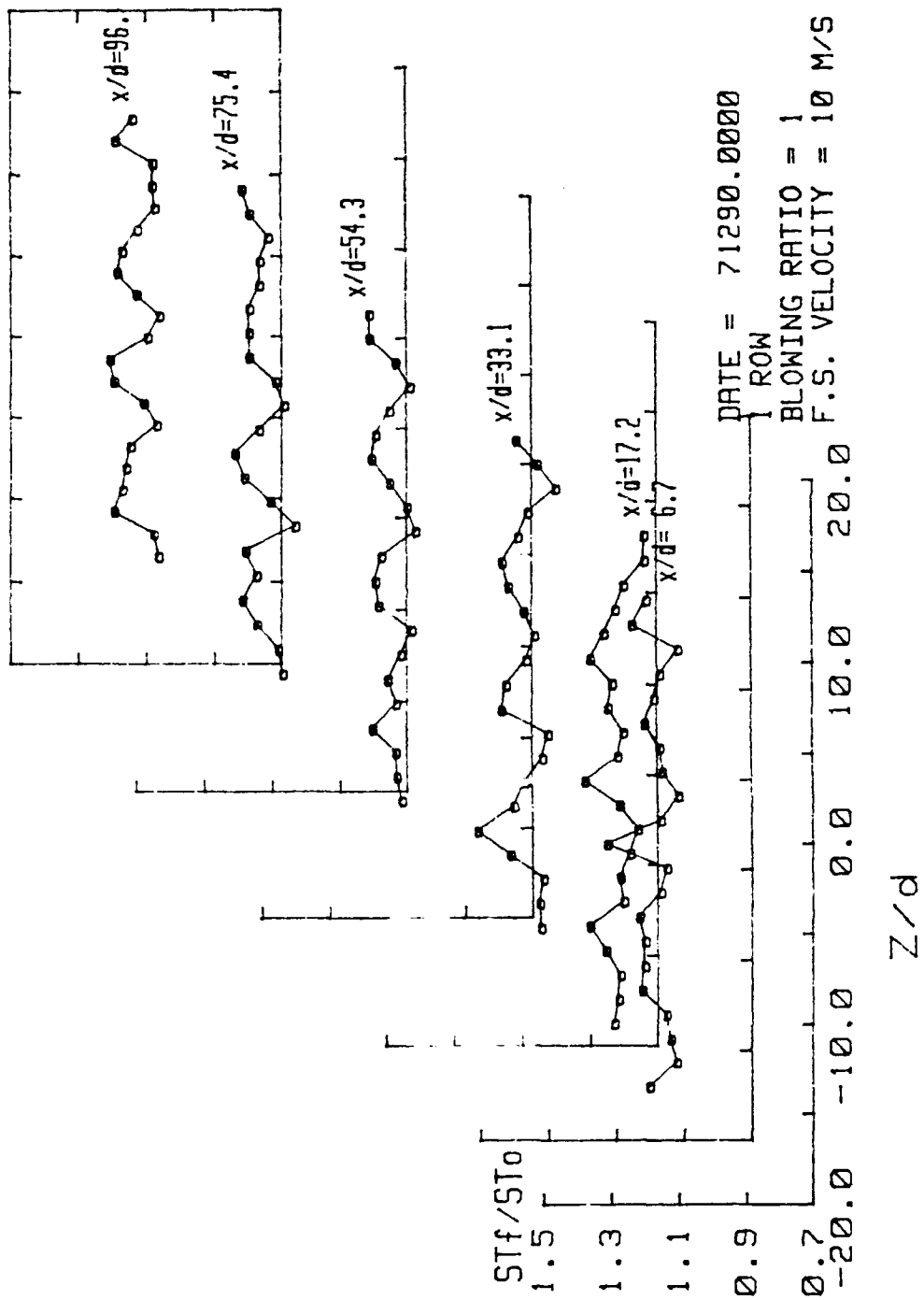


Figure 20. Spanwise Variation of St_f/St_0 , 1 row $m=1.0$

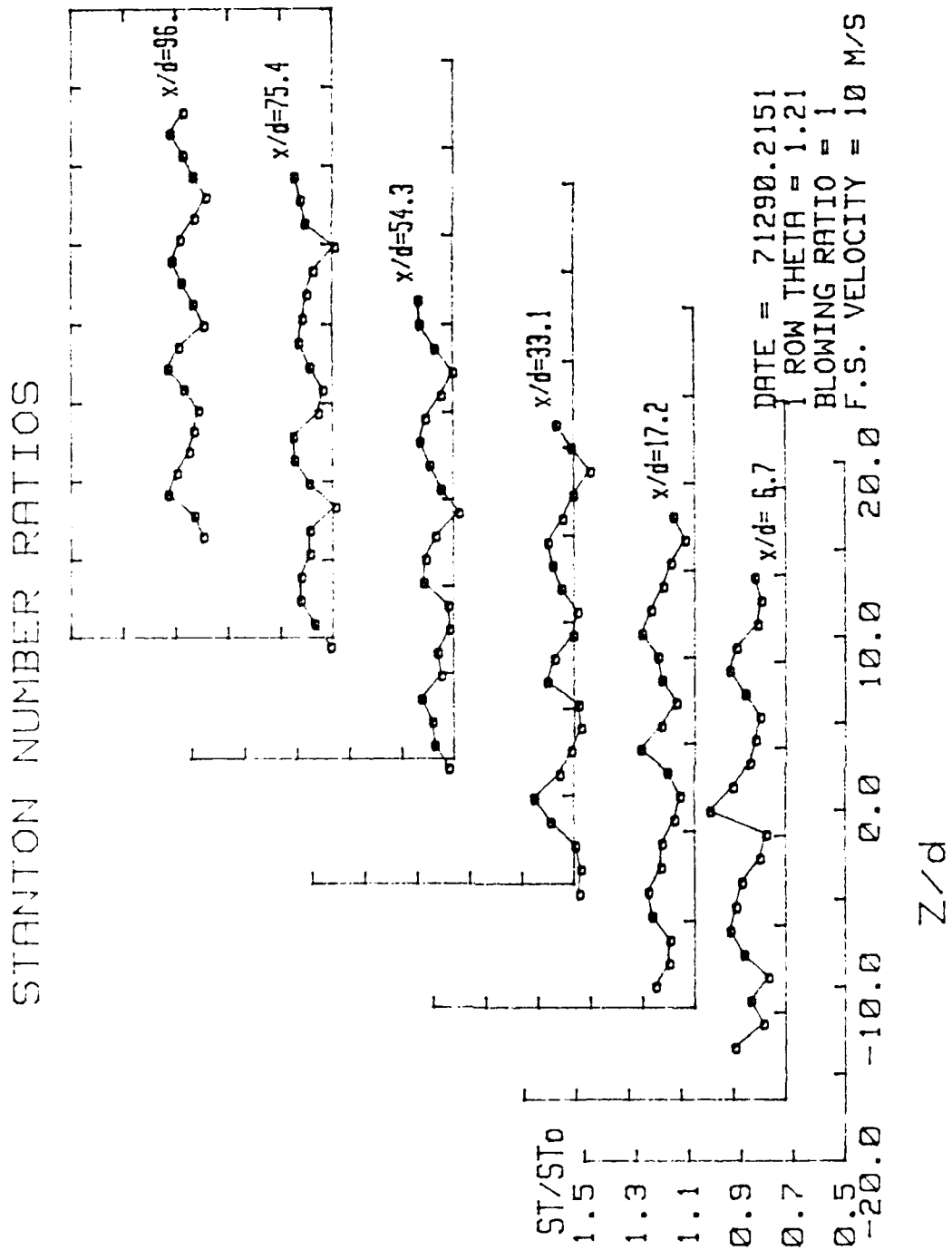


Figure 21. Spanwise Variation of St/St_0 , 1 row $m=1.0$, $\theta=1.21$

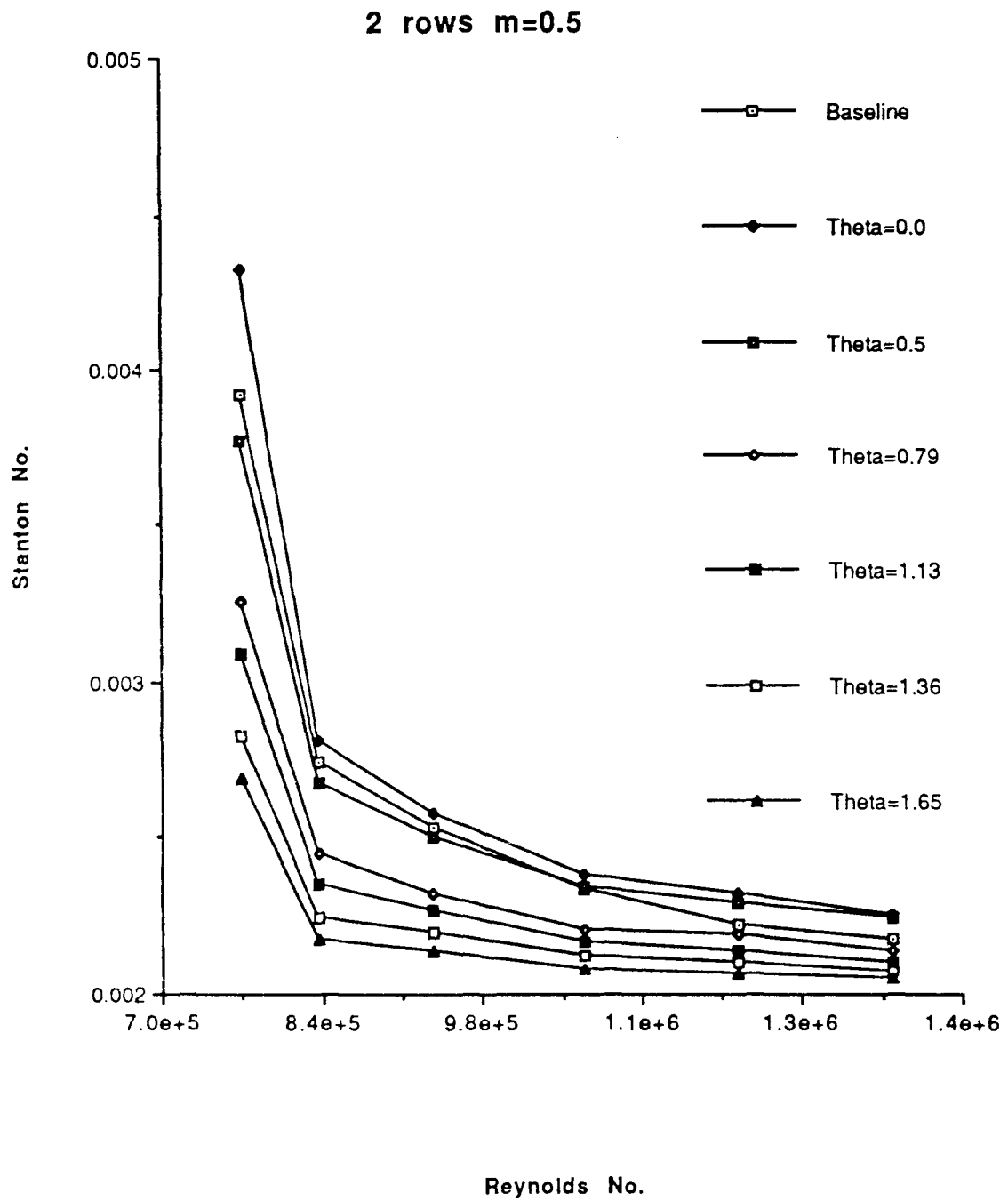


Figure 22. Stanton number (St) comparison, 2 rows $m=0.5$

FILM-COOLING EFFECTIVENESS

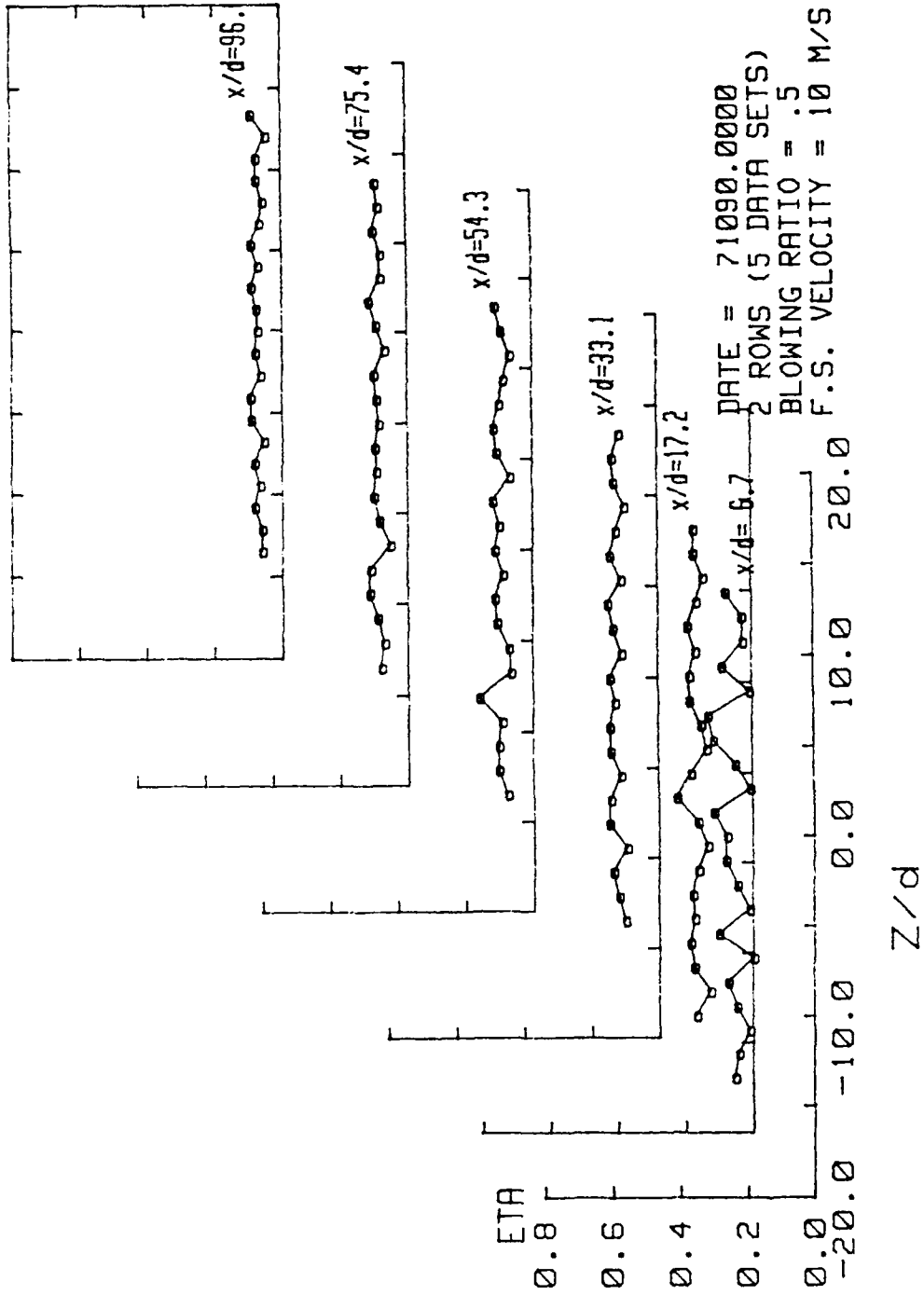


Figure 23. Spanwise Variation of η , 2 rows $m=0.5$ (5 data sets)

FILM-COOLING EFFECTIVENESS

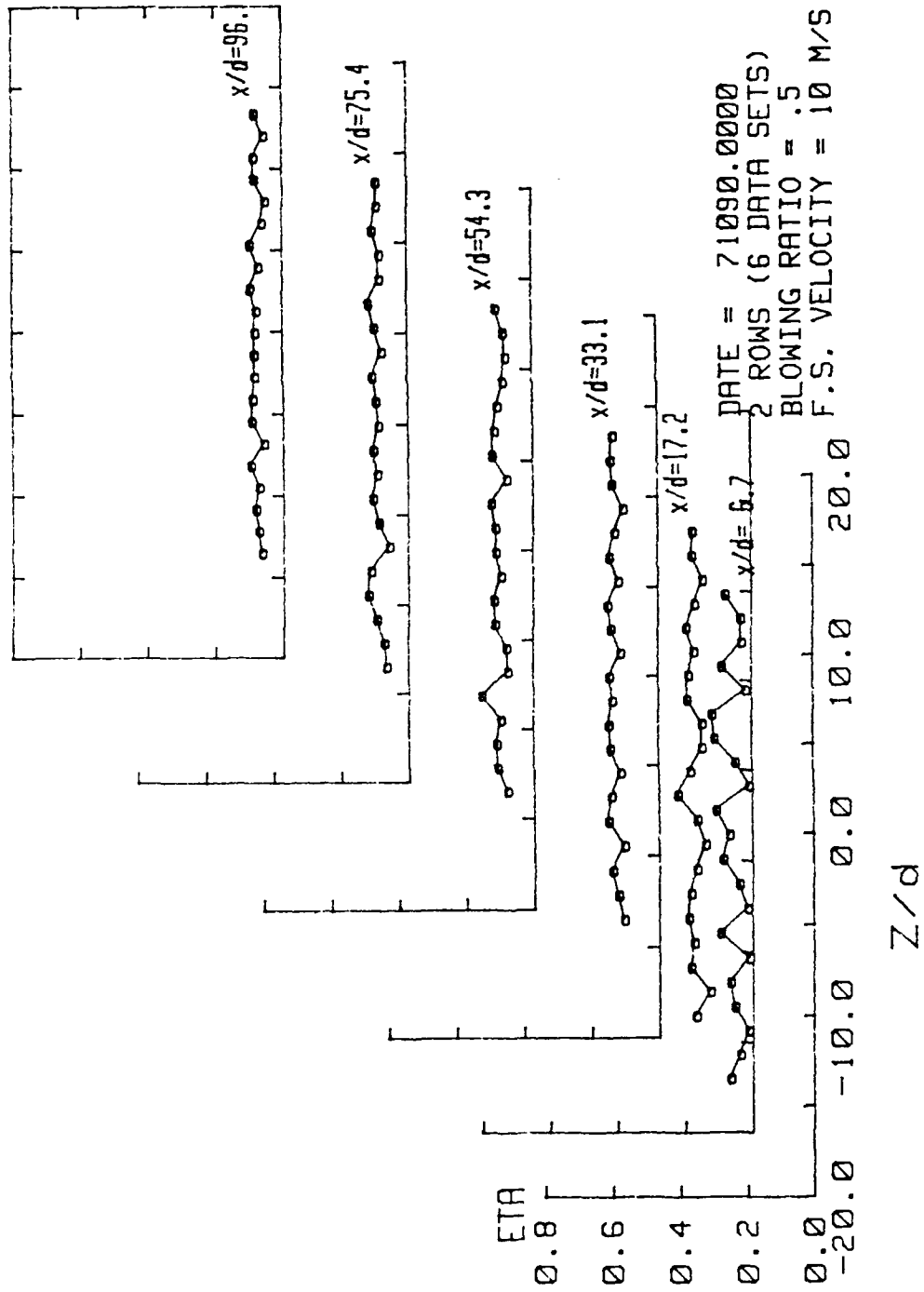


Figure 24. Spanwise Variation of η , 2 rows $m=0.5$ (6 data sets)

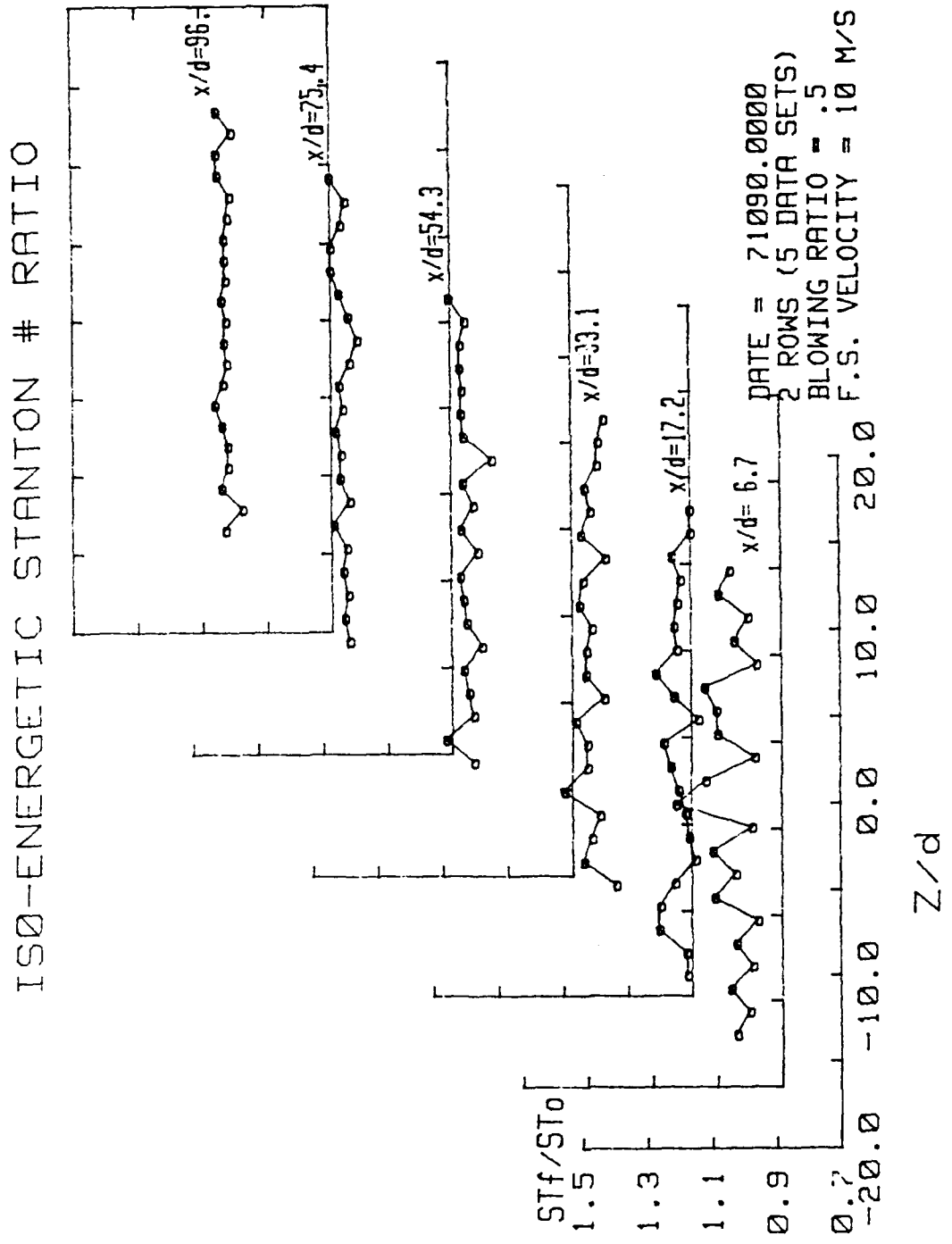


Figure 25. Spanwise Variation of St_f/St_0 , 2 rows $m=0.5$ (5 data sets)

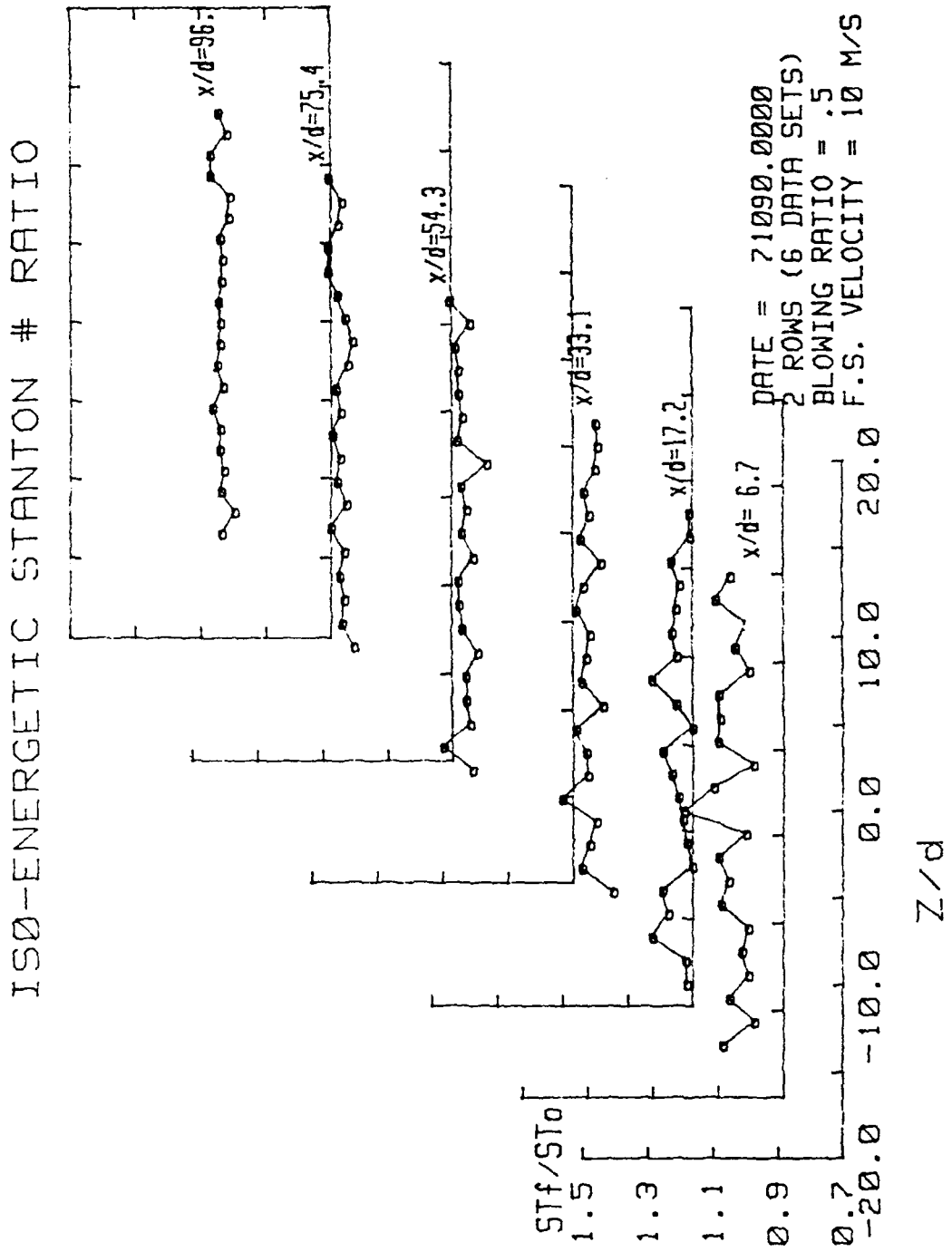


Figure 26. Spanwise Variation of St_f/St_0 , 2 rows $m=0.5$ (6 data sets)

STANTON NUMBER RATIOS

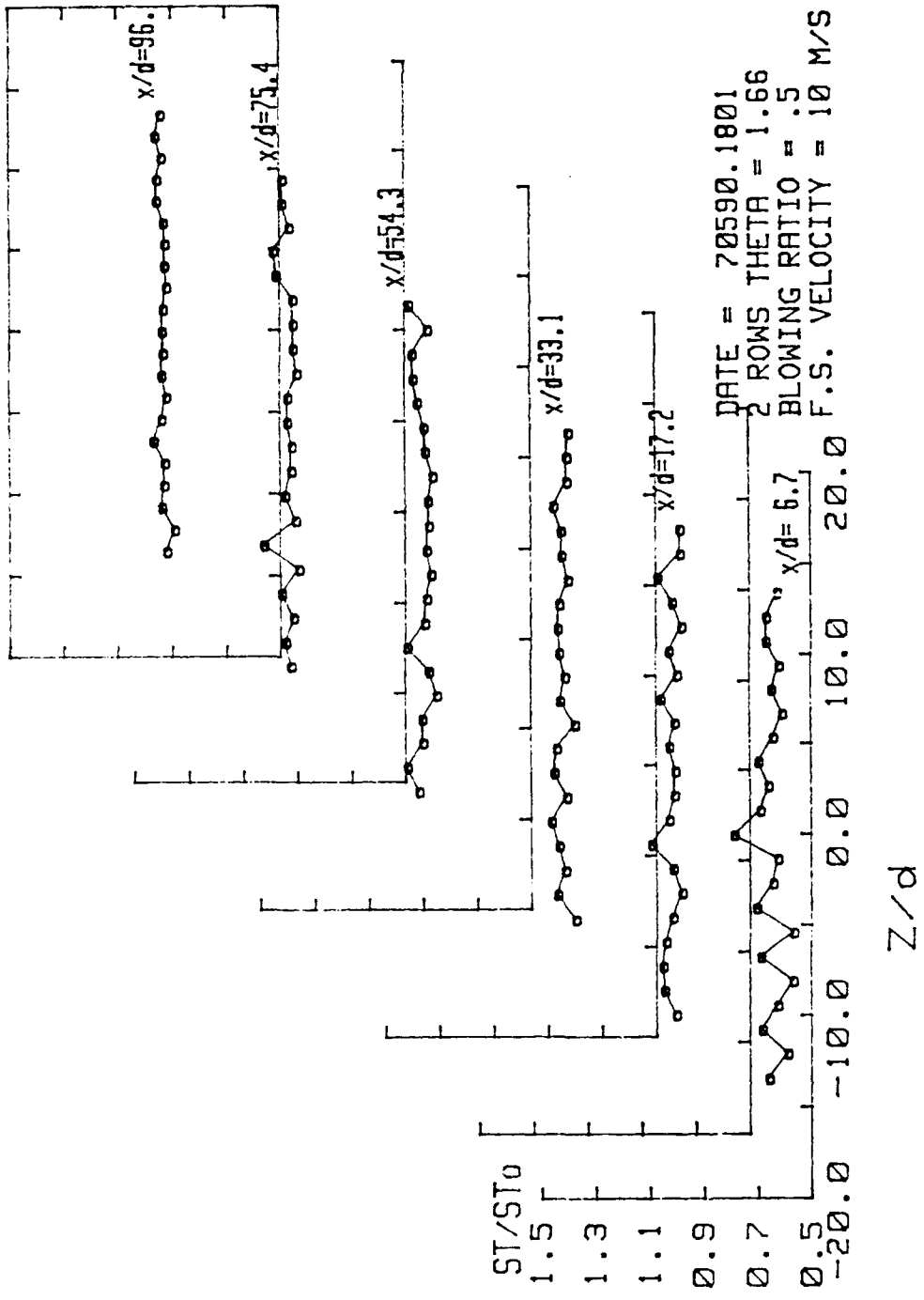


Figure 27. Spanwise Variation of St/St_0 , 2 rows $m=0.5$, $\theta=1.66$

2 rows $m=0.5$ $z=0.0$

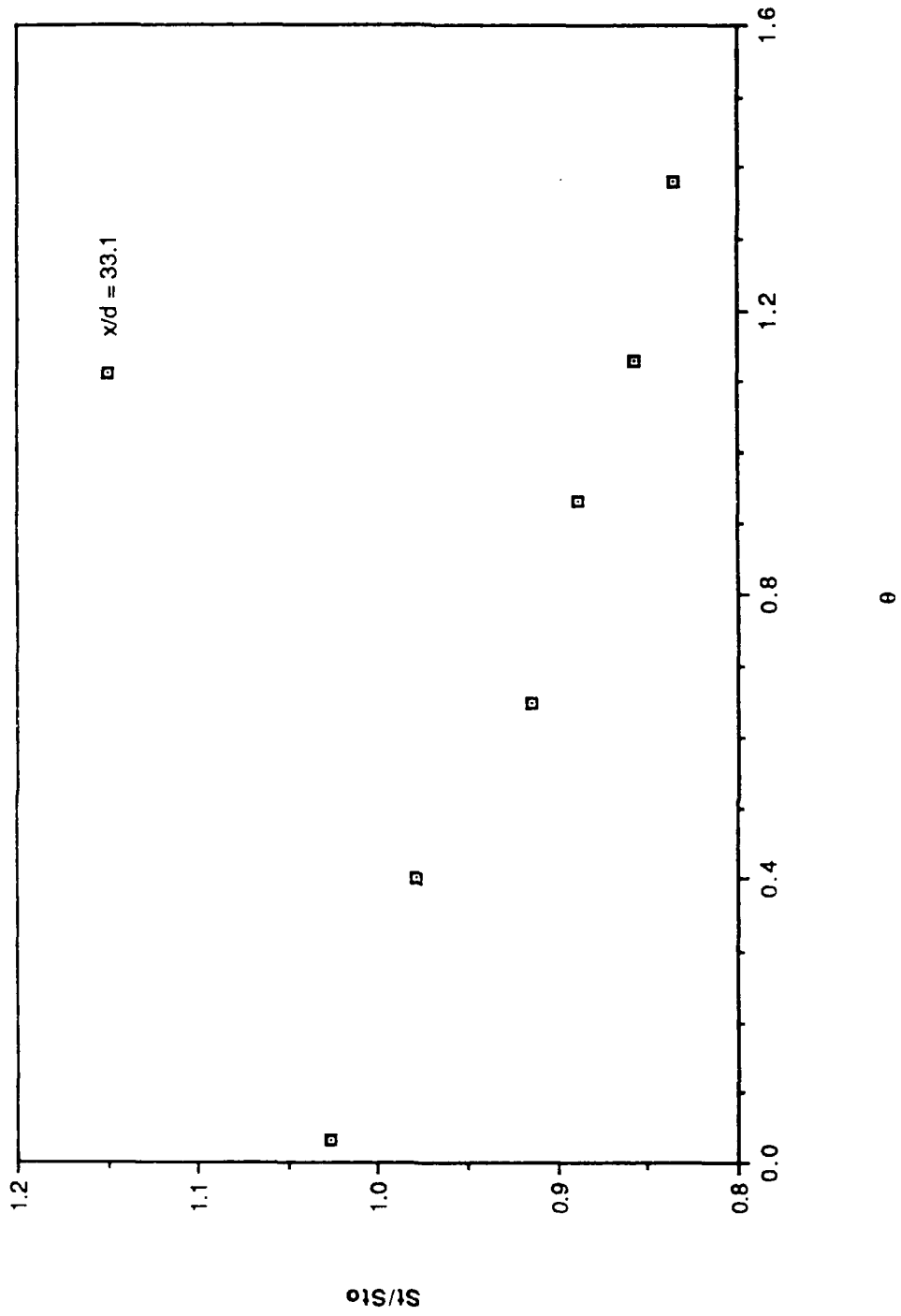


Figure 28. St/St_0 versus θ , 2 rows $m=0.5$, $x/d=33.1$, $Z=0.0$ cm, compact

2 rows $m=0.5$ $z=0.0$

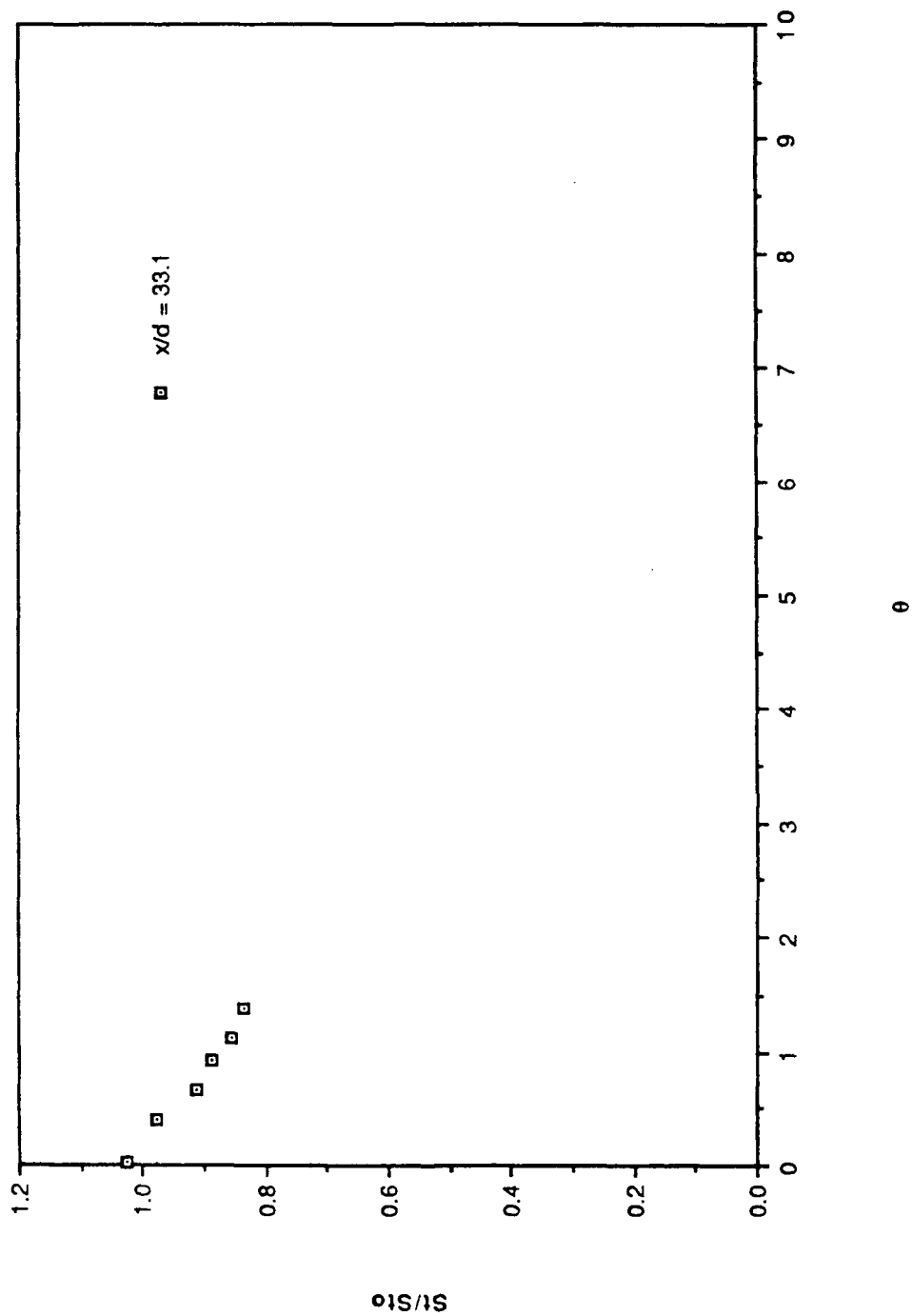


Figure 29. St/St_0 versus θ , 2 rows $m=0.5$, $x/d=33.1$, $Z=0.0$ cm, expanded

2 rows $m=0.5$ $z=0.0$

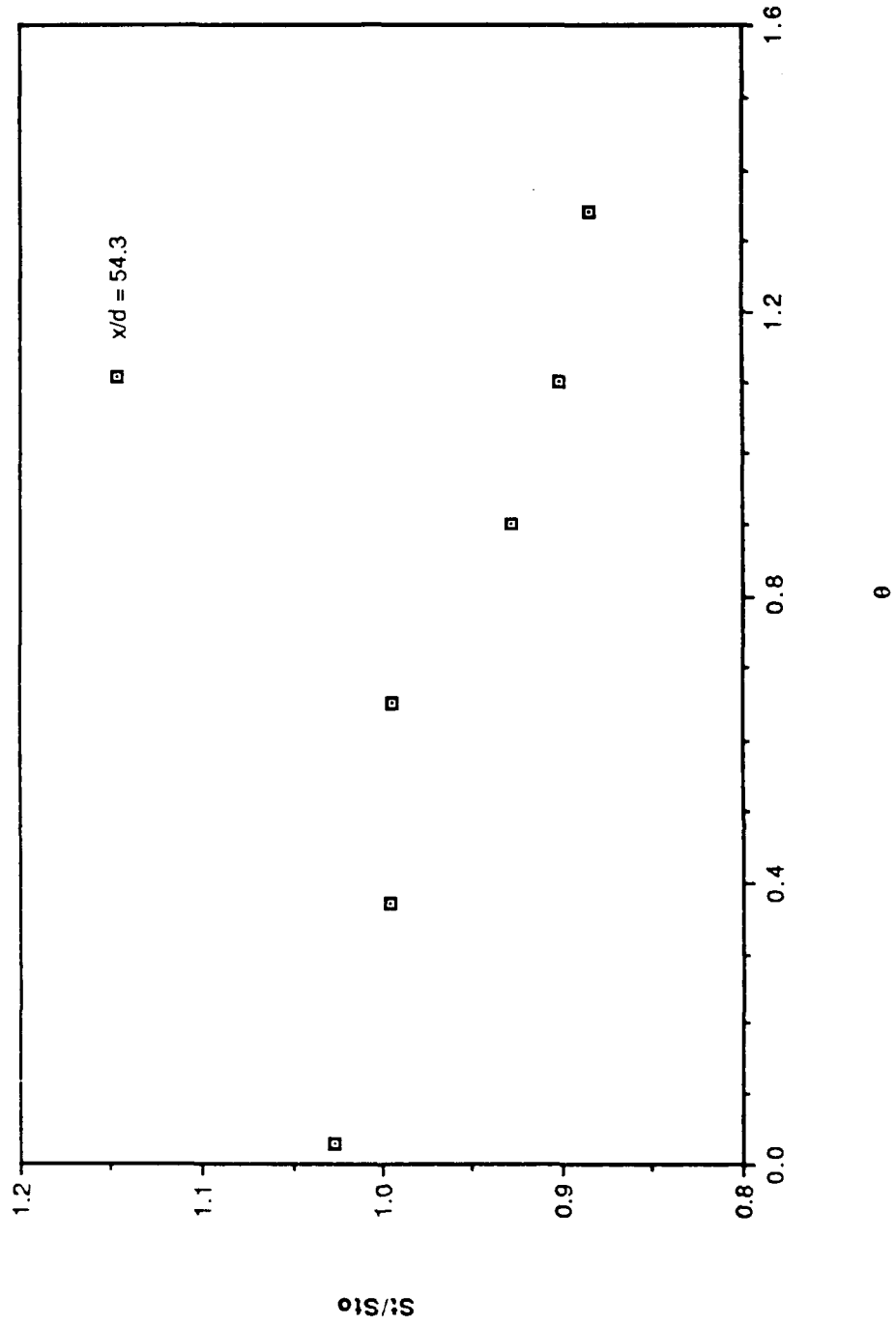


Figure 30. St/St_0 versus θ , 2 rows $m=0.5$, $x/d=54.3$, $Z=0.0$ cm, compact

2 rows $m=0.5$ $z=0.0$

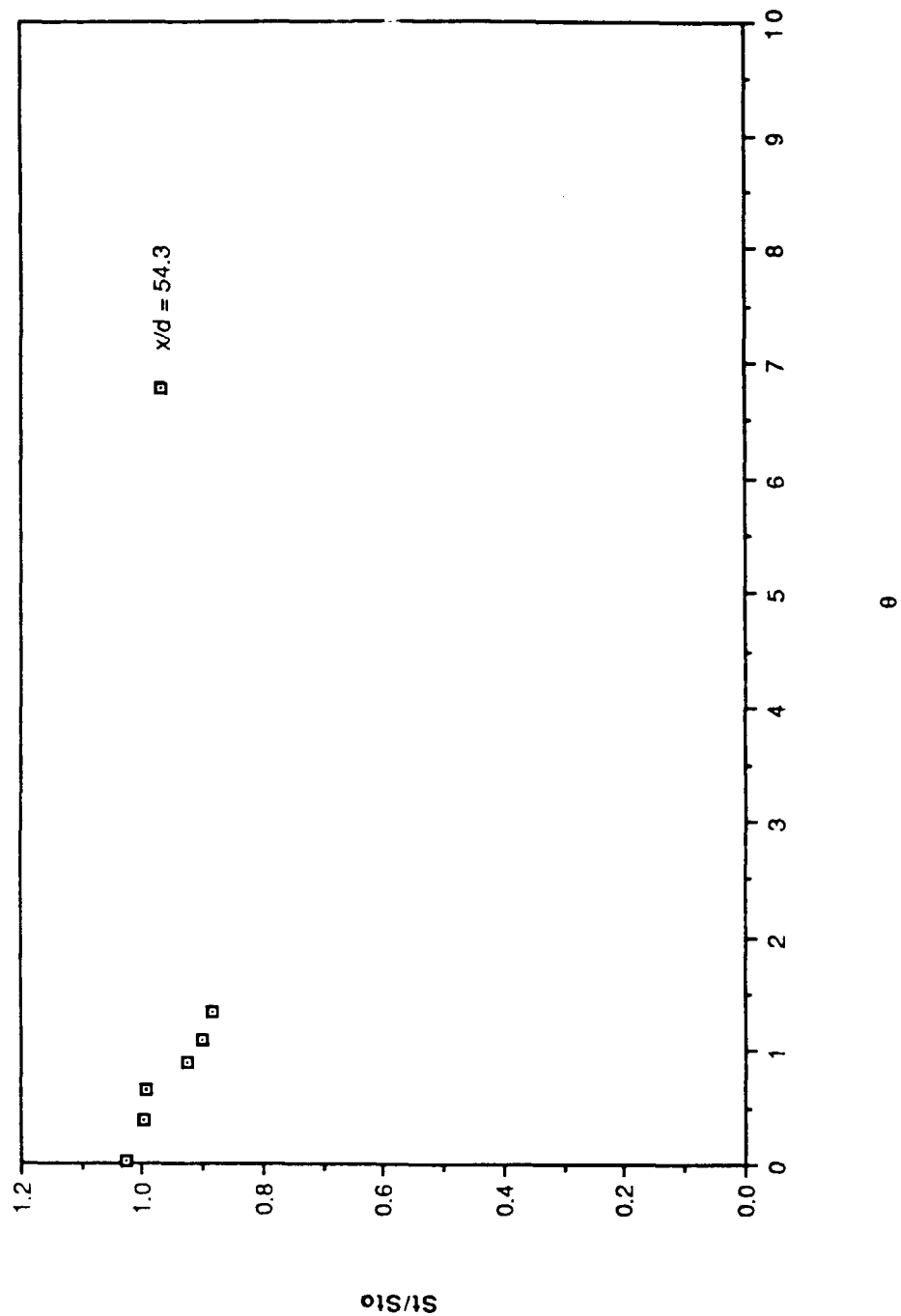


Figure 31. St/St_0 versus θ , 2 rows $m=0.5$, $x/d=54.3$, $Z=0.0$ cm, expanded

2 rows $m=0.5$ $z=0.0$

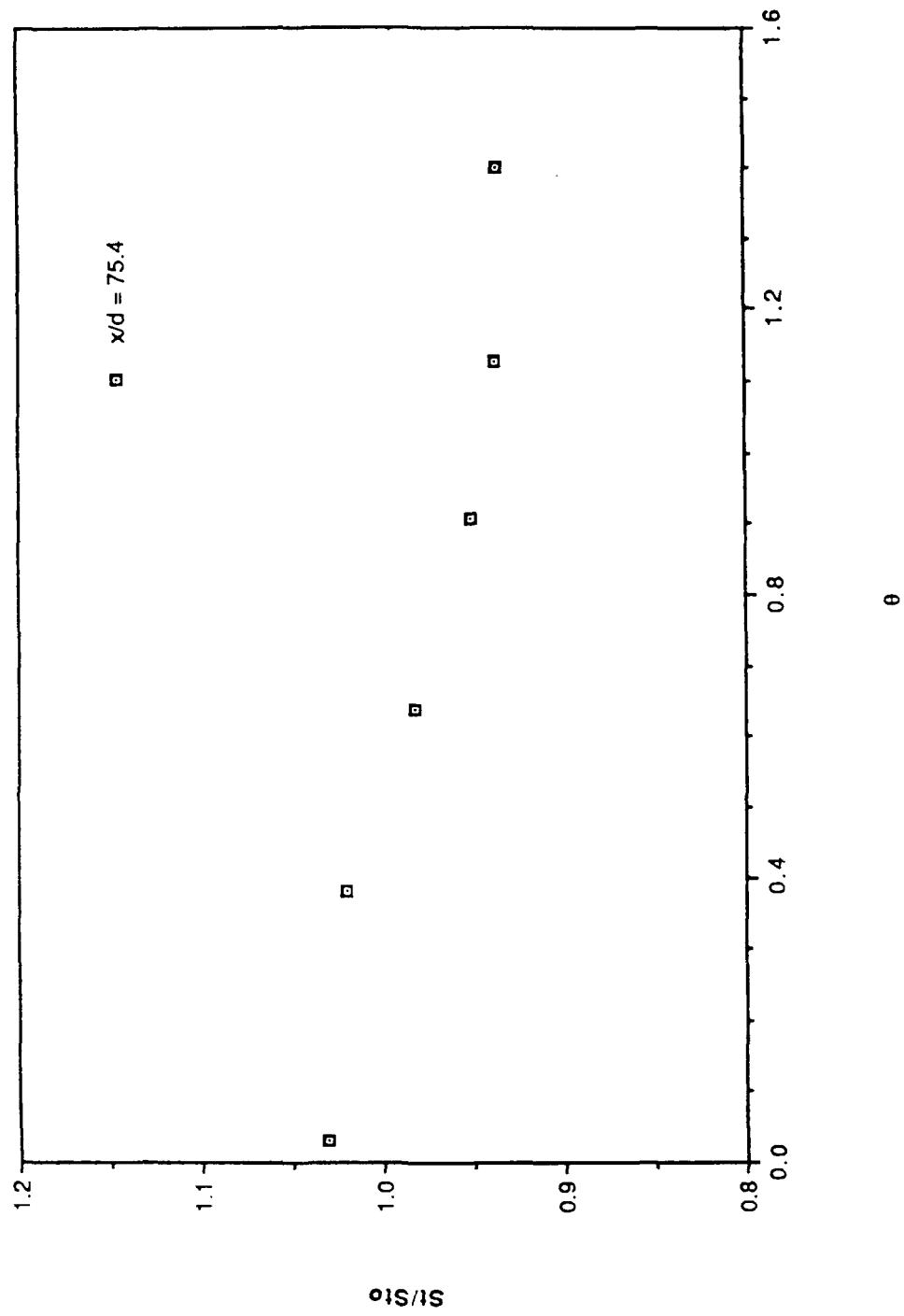


Figure 32. St/St_0 versus θ , 2 rows $m=0.5$, $x/d=75.4$, $Z=0.0$ cm, compact

2 rows $m=0.5$ $z=0.0$

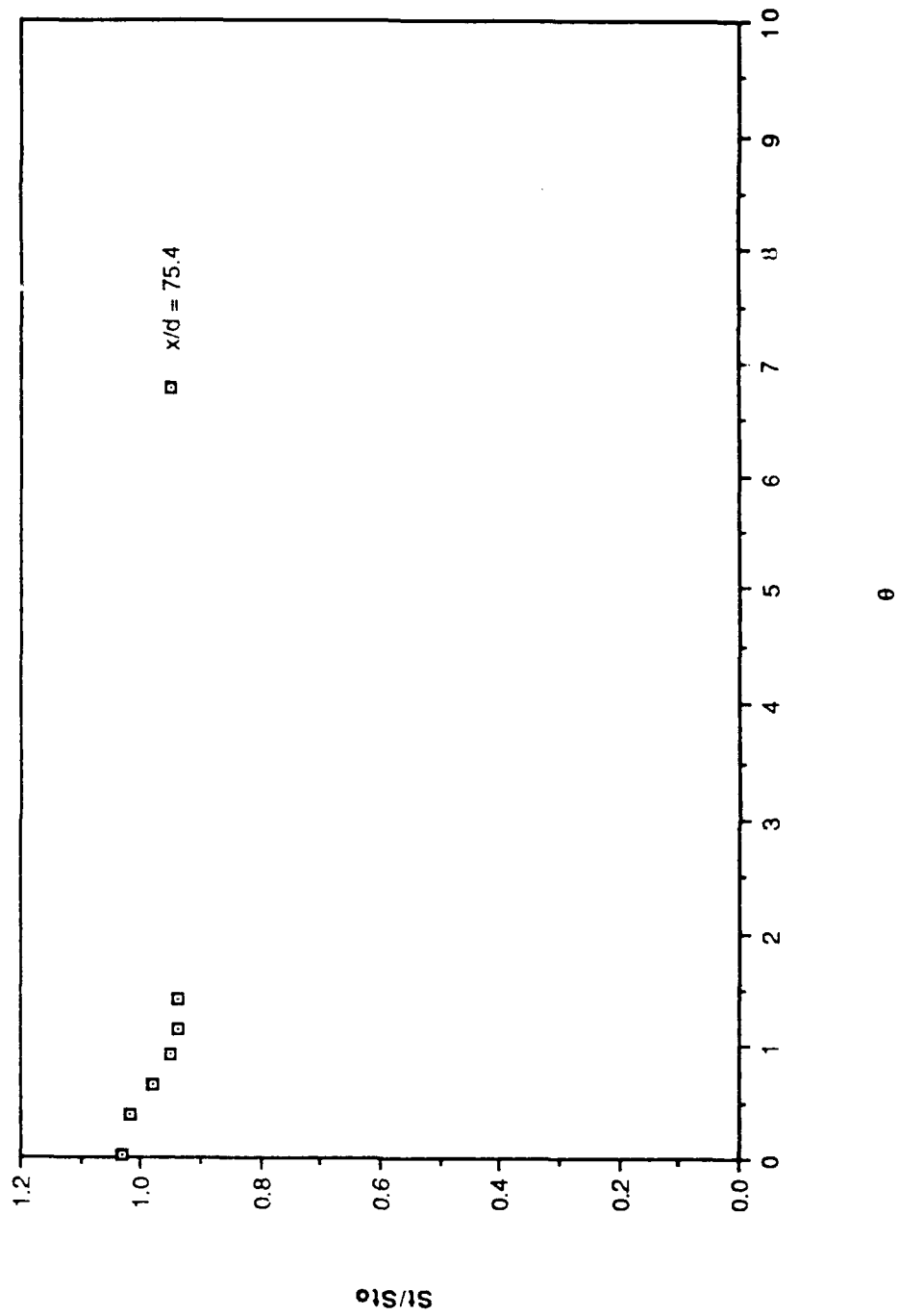


Figure 33. St/St_0 versus θ , 2 rows $m=0.5$, $x/d=75.4$, $Z=0.0$ cm, expanded

2 rows $m=0.5$ $z=0.0$

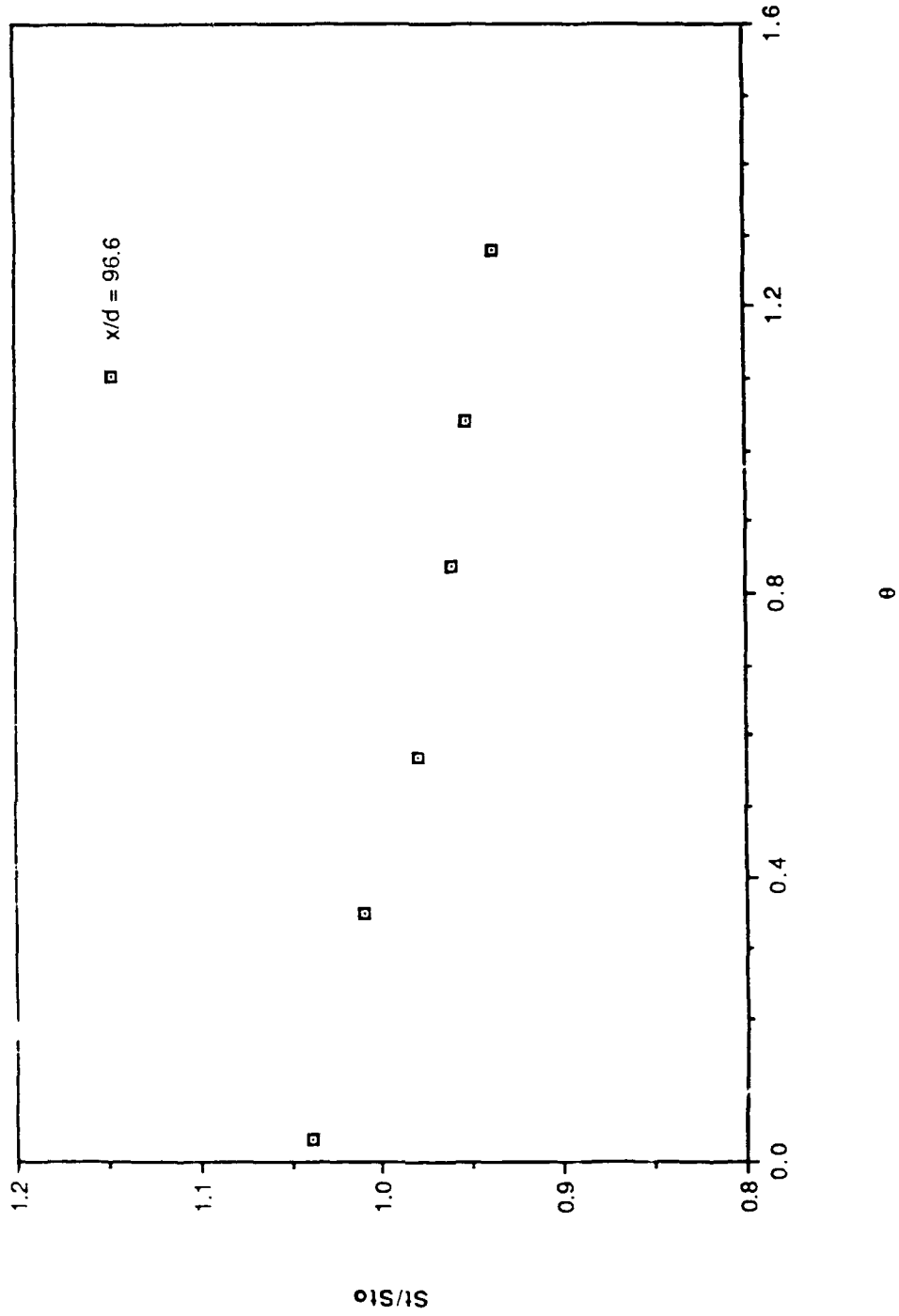


Figure 34. S_4/St_0 versus θ , 2 rows $m=0.5$, $x/d=96.6$, $Z=0.0$ cm, compact

2 rows $m=0.5$ $z=0.0$

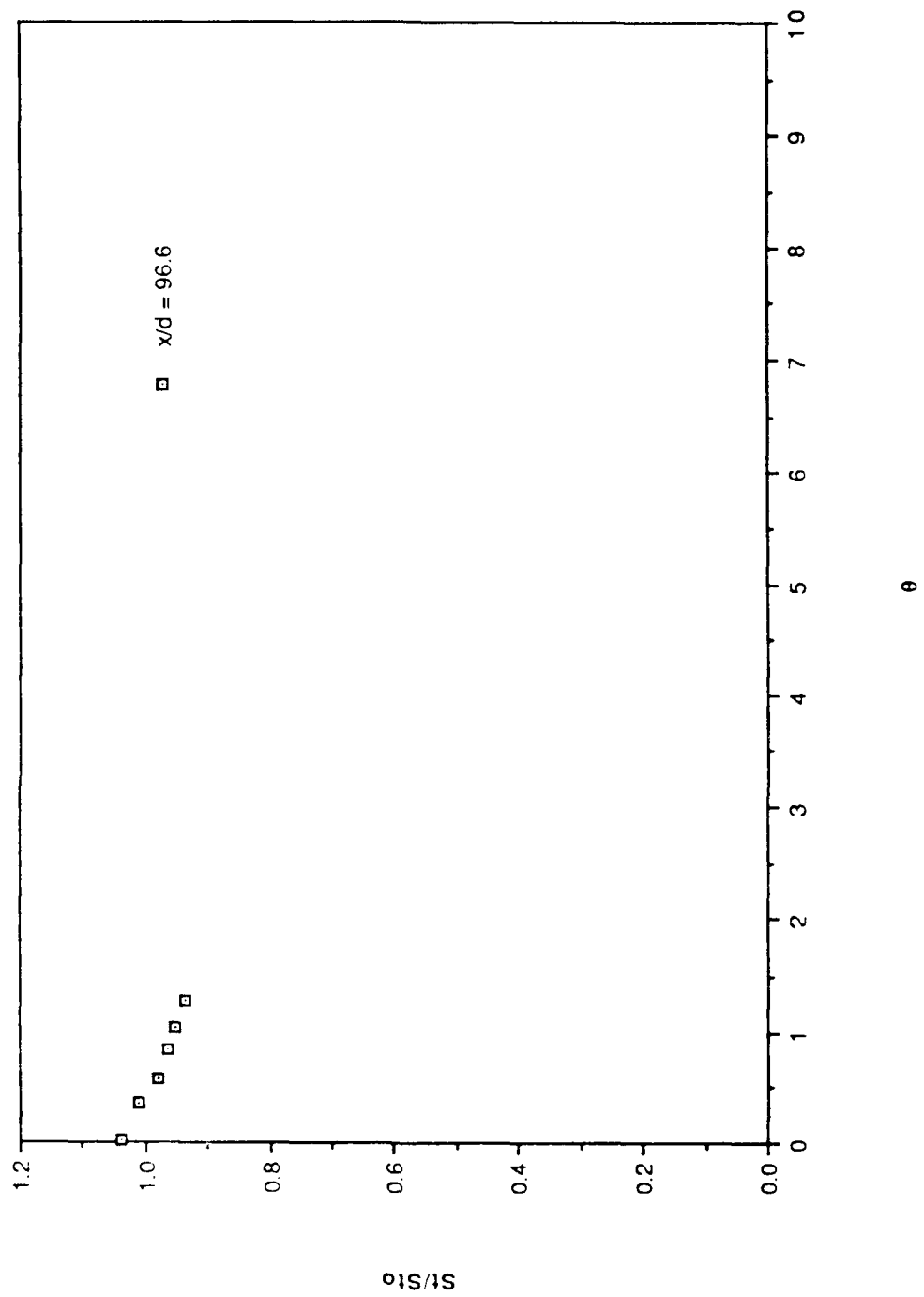


Figure 35. St/St_0 versus θ , 2 rows $m=0.5$, $x/d=96.6$, $Z=0.0$ cm, expanded

2 rows $m=0.5$ $z=-6.35$

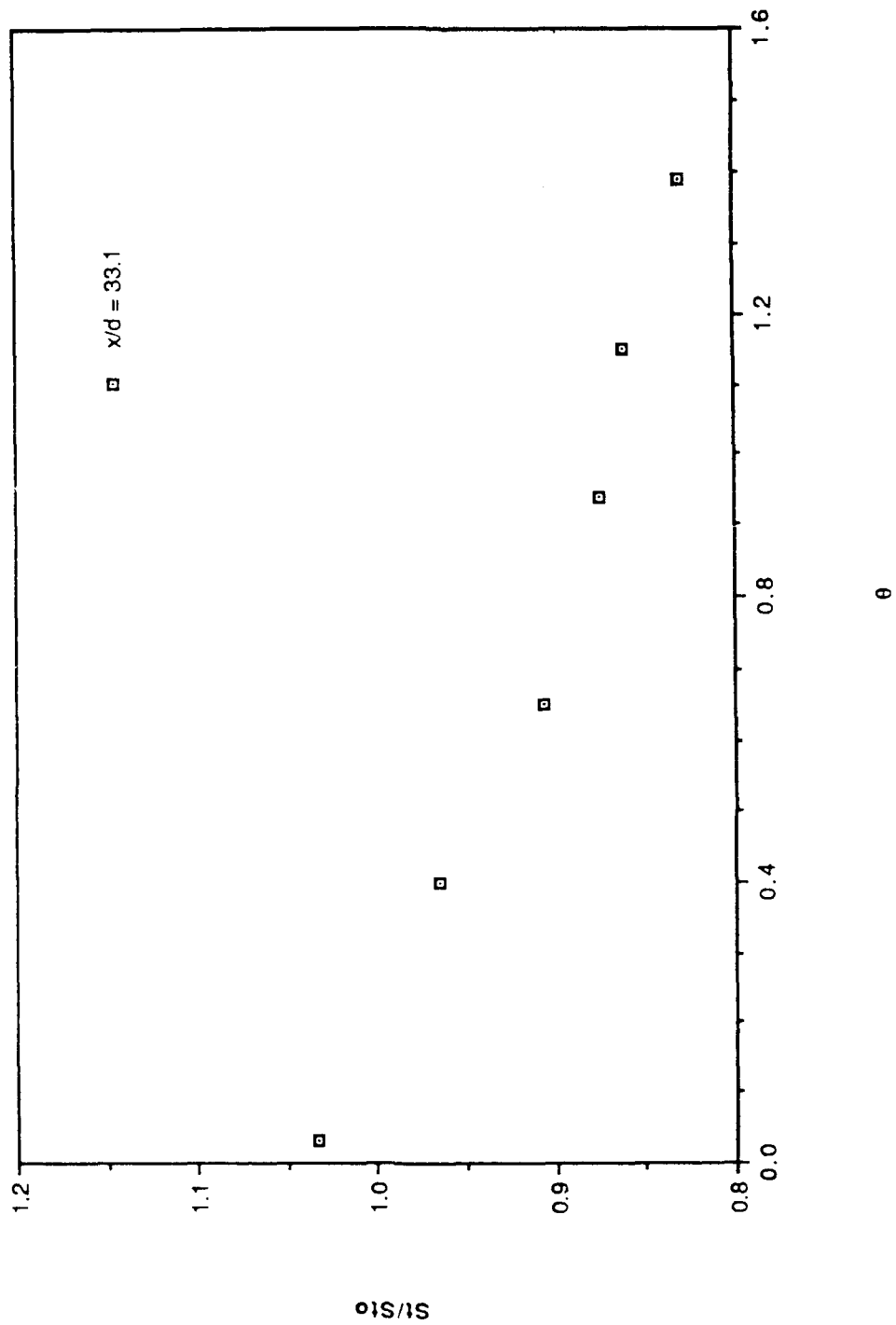


Figure 36. St/St_0 versus θ , 2 rows $m=0.5$, $x/d=33.1$, $Z=-6.35$ cm, compact

2 rows $m=0.5$ $Z=-6.35$

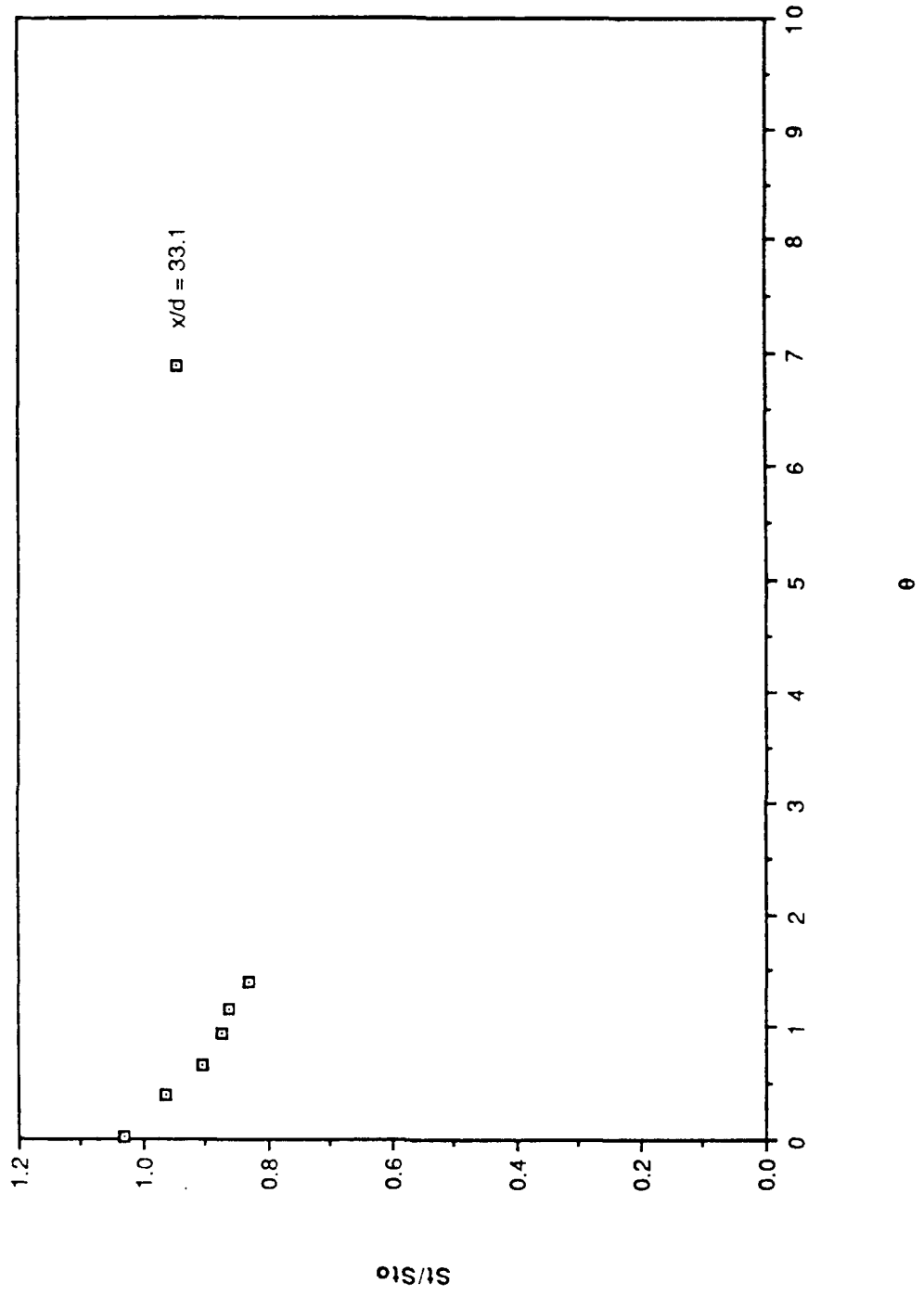


Figure 37. St/St_0 versus θ , 2 rows $m=0.5$, $x/d=33.1$, $Z=-6.35$ cm, expanded

2 rows $m=0.5$ $Z=-6.35$

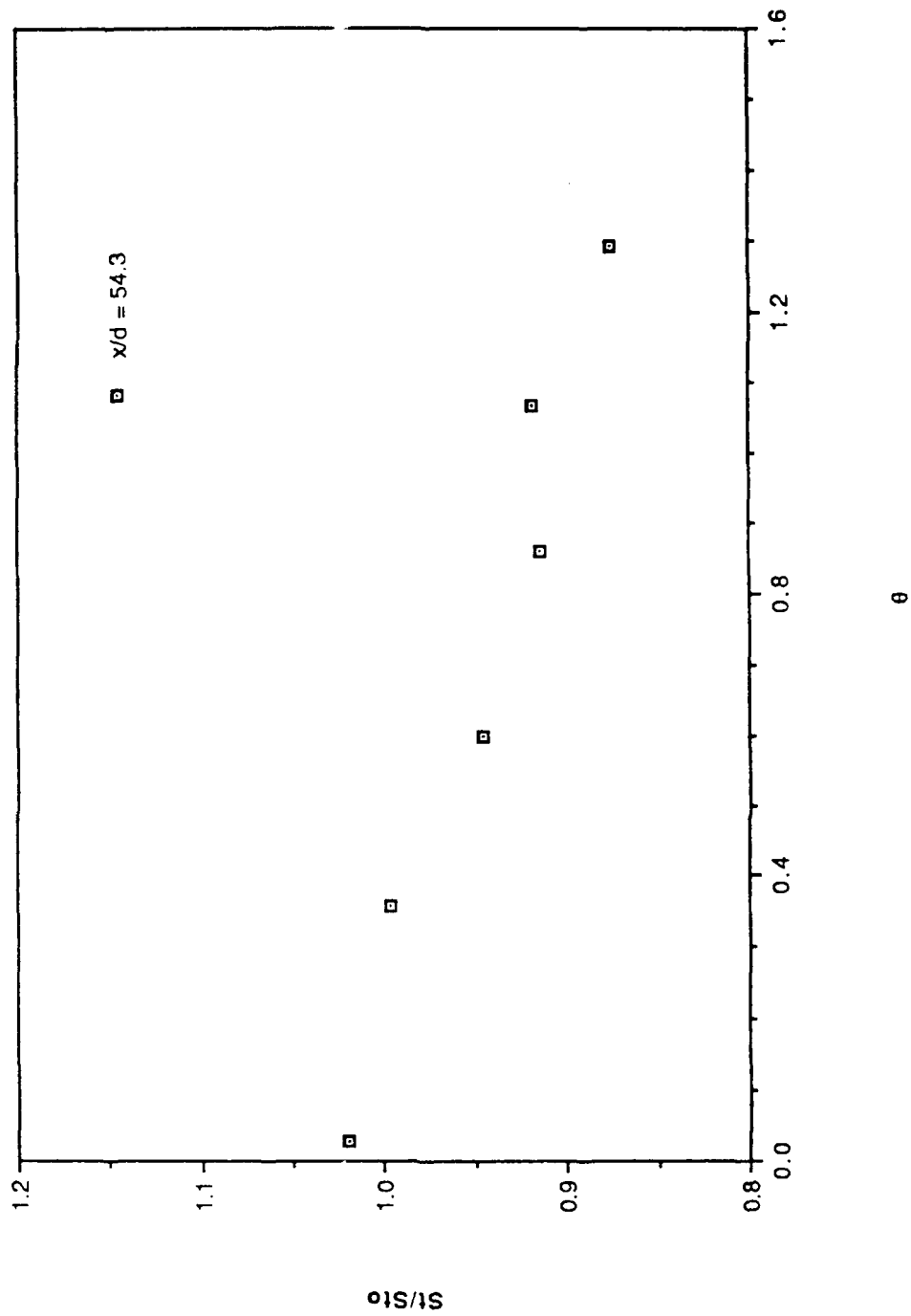


Figure 38. St/St_0 versus θ , 2 rows $m=0.5$, $x/d=54.3$, $Z=-6.35$ cm, compact

2 rows $m=0.5$ $z=-6.35$

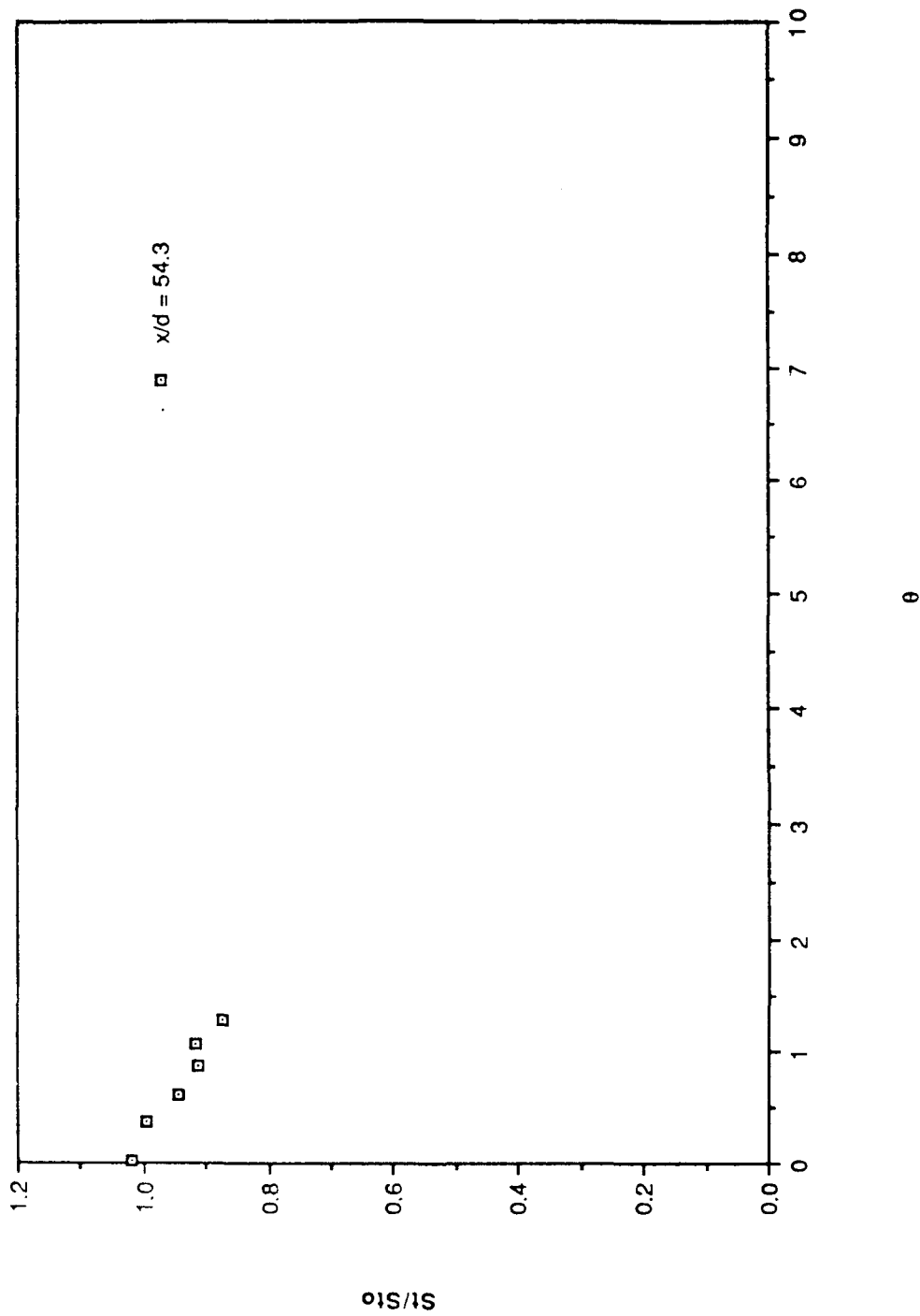


Figure 39. St/St_0 versus θ , 2 rows $m=0.5$, $x/d=54.3$, $Z=-6.35$ cm, expanded

2 rows $m=0.5$ $z=-6.35$

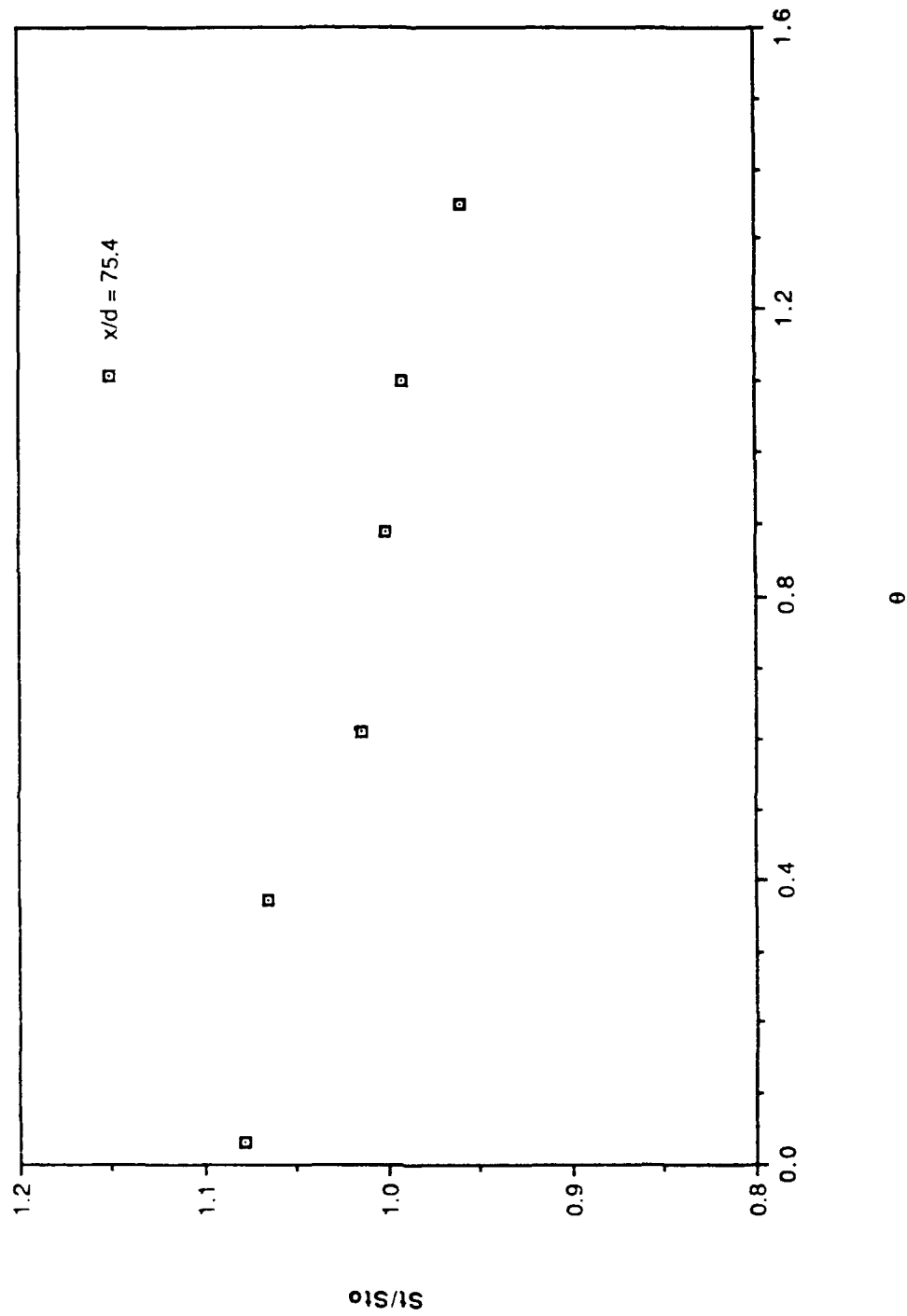


Figure 40. St/St_0 versus θ , 2 rows $m=0.5$, $x/d=75.4$, $Z=-6.35$ cm, compact

2 rows $m=0.5$ $z=-6.35$

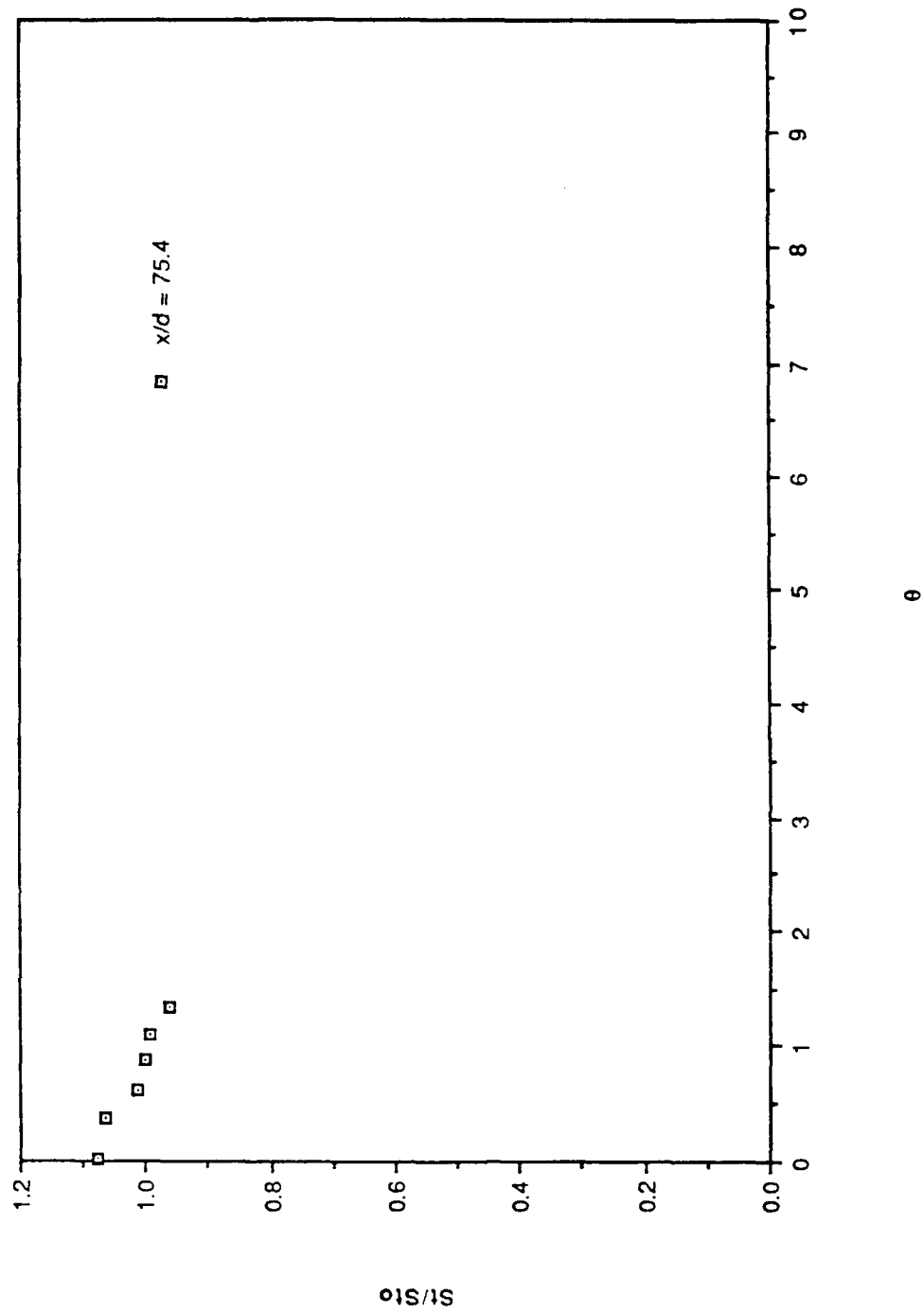


Figure 41. St/St_0 versus θ , 2 rows $m=0.5$, $x/d=75.4$, $Z=-6.35$ cm, expanded

2 rows $m=0.5$ $Z=-6.35$

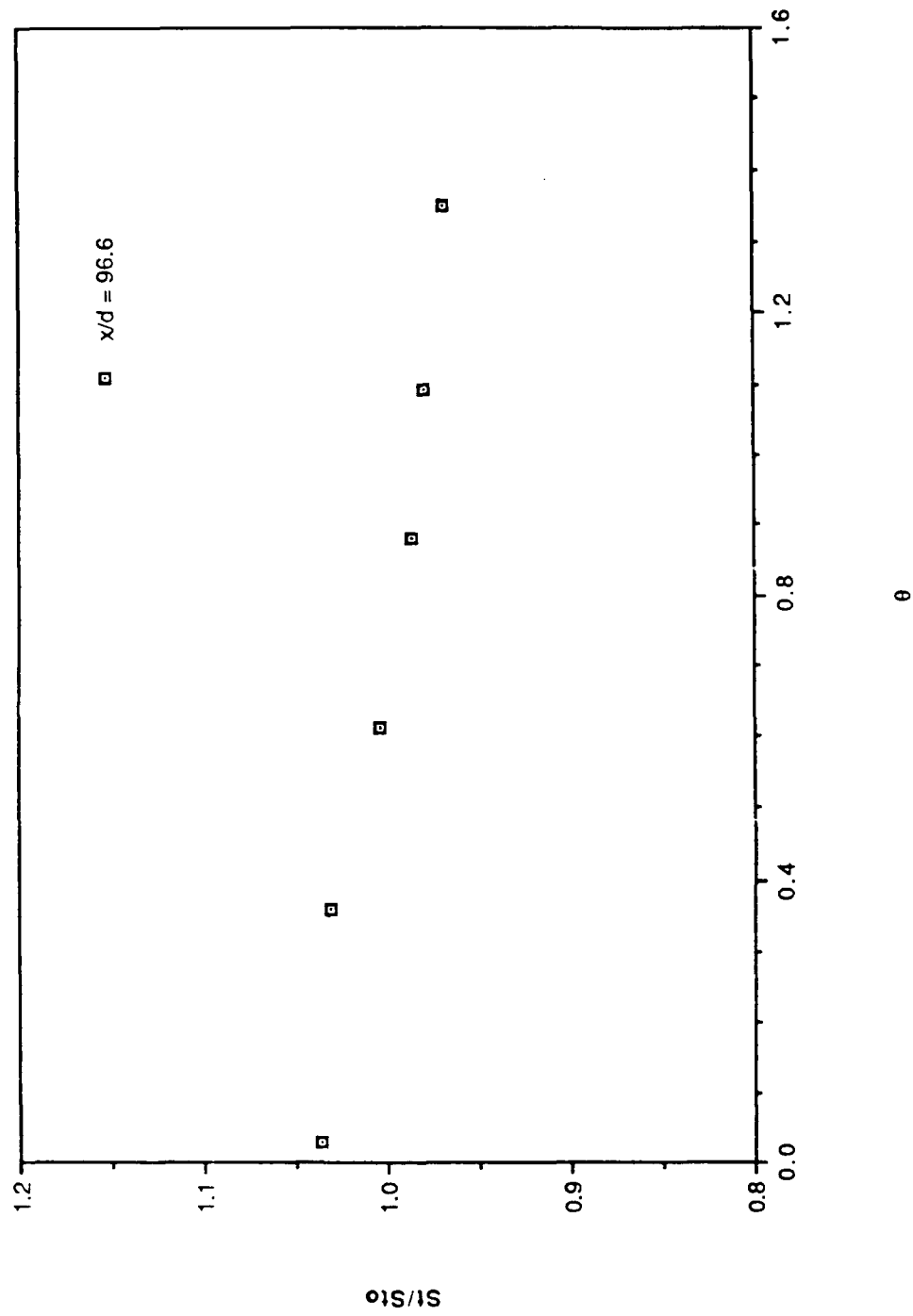


Figure 42. St/St_0 versus θ , 2 rows $m=0.5$, $x/d=96.6$, $Z=-6.35$ cm, compact

2 rows $m=0.5$ $Z=-6.35$

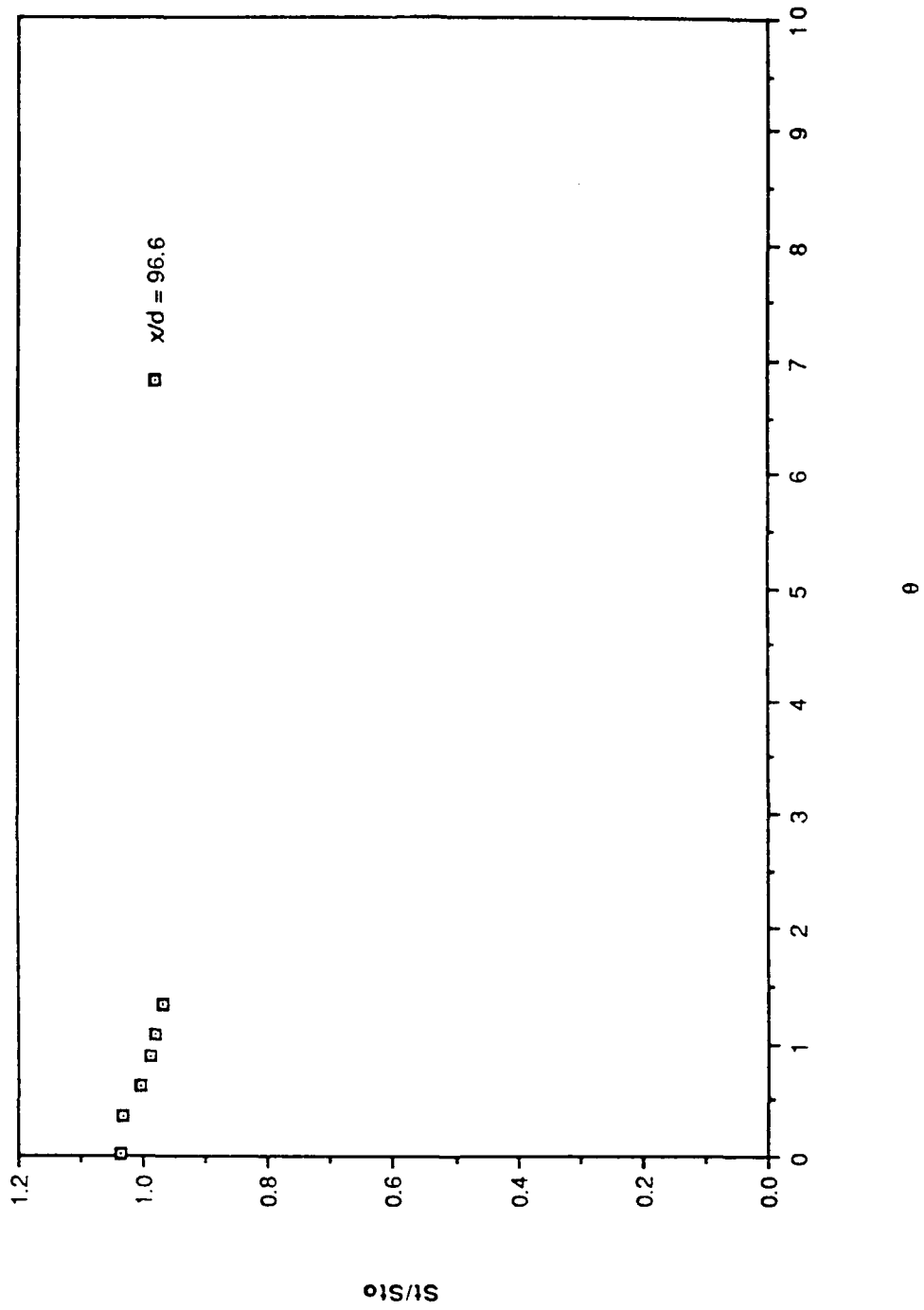


Figure 43. St/St_0 versus θ , 2 rows $m=0.5$, $x/d=96.6$, $Z=-6.35$ cm, expanded

2 rows $m=0.5$ $Z=+6.35$

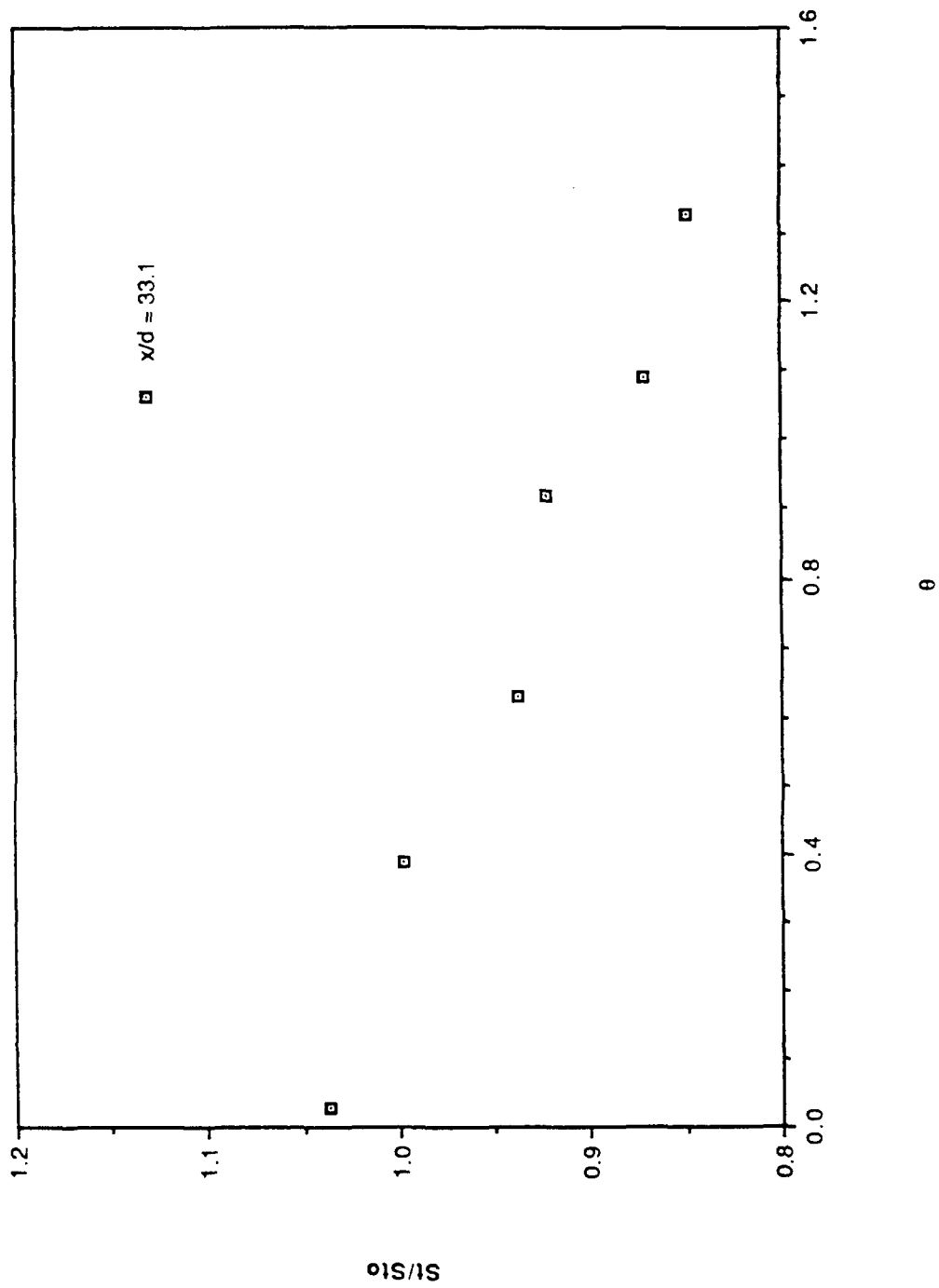


Figure 44. St/St_0 versus θ , 2 rows $m=0.5$, $x/d=33.1$, $Z=+6.35$ cm, compact

2 rows $m=0.5$ $Z=+6.35$

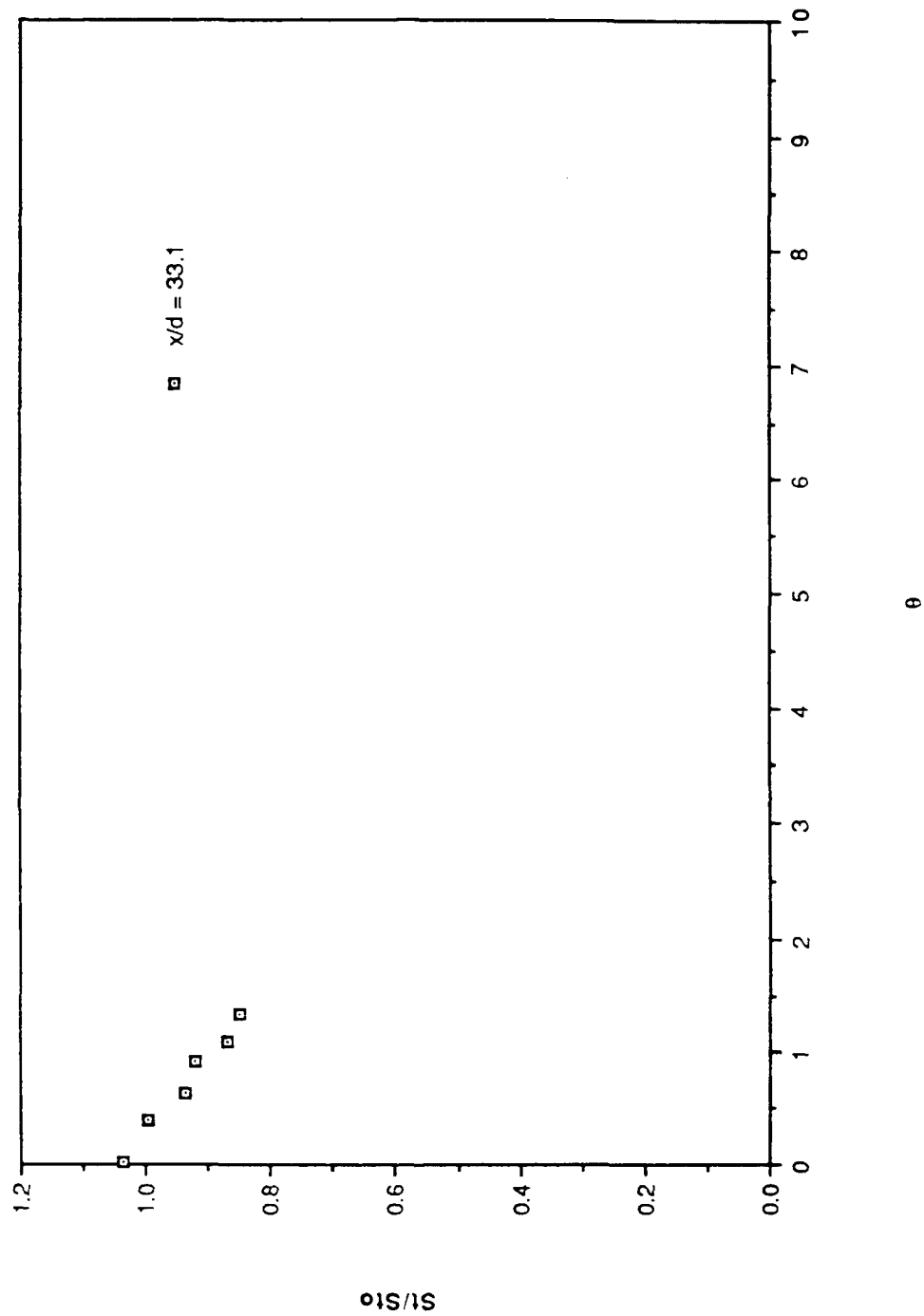


Figure 45. St/St_0 versus θ , 2 rows $m=0.5$, $x/d=33.1$, $Z=+6.35$ cm, expanded

2 rows $m=0.5$ $Z=+6.35$

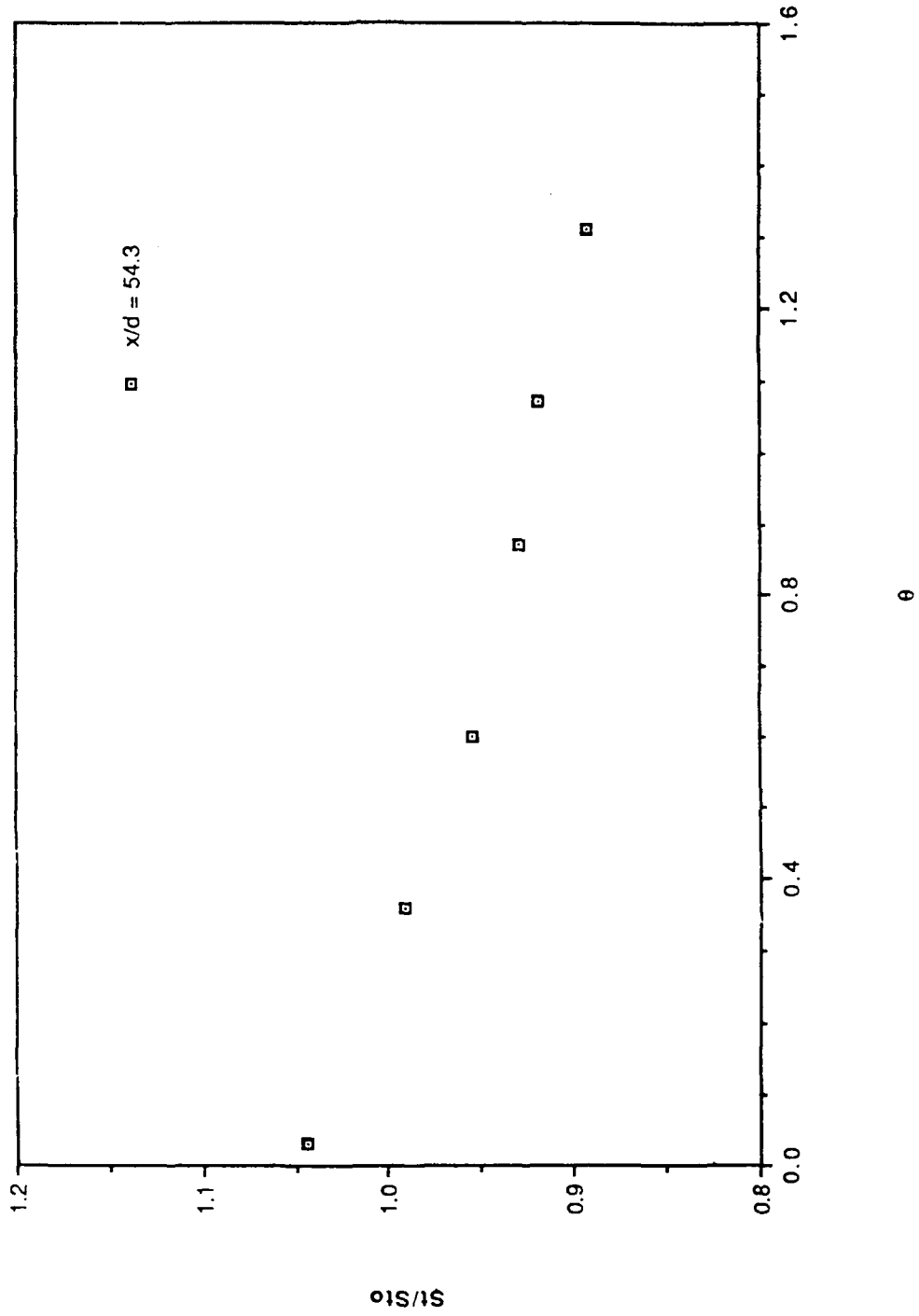


Figure 46. St/St_0 versus θ , 2 rows $m=0.5$, $x/d=54.3$, $Z=+6.35$ cm, compact

2 rows $m=0.5$ $Z=+6.35$

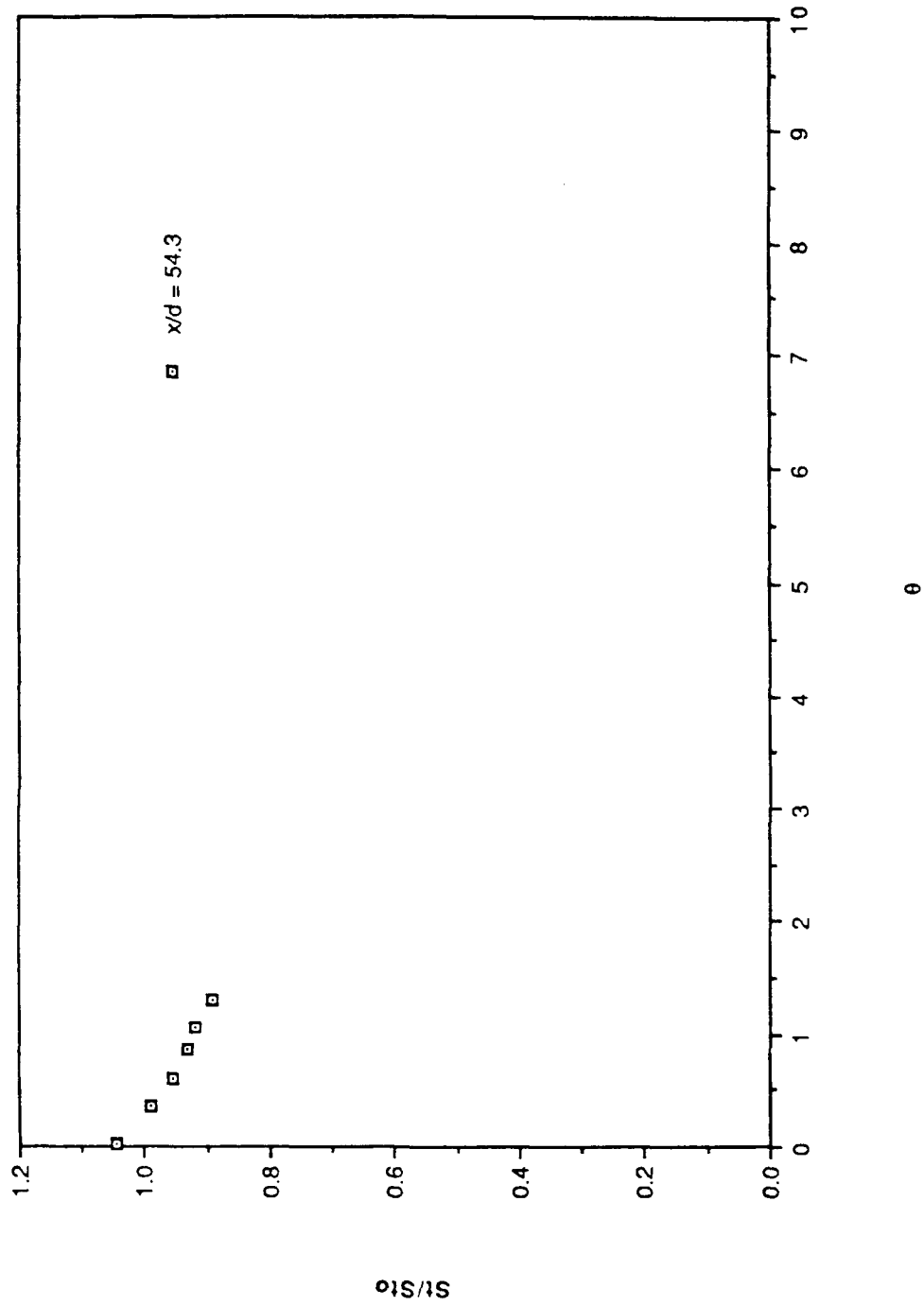


Figure 47. St/St_0 versus θ , 2 rows $m=0.5$, $x/d=54.3$, $Z=+6.35$ cm, expanded

2 rows $m=0.5$ $Z=+6.35$

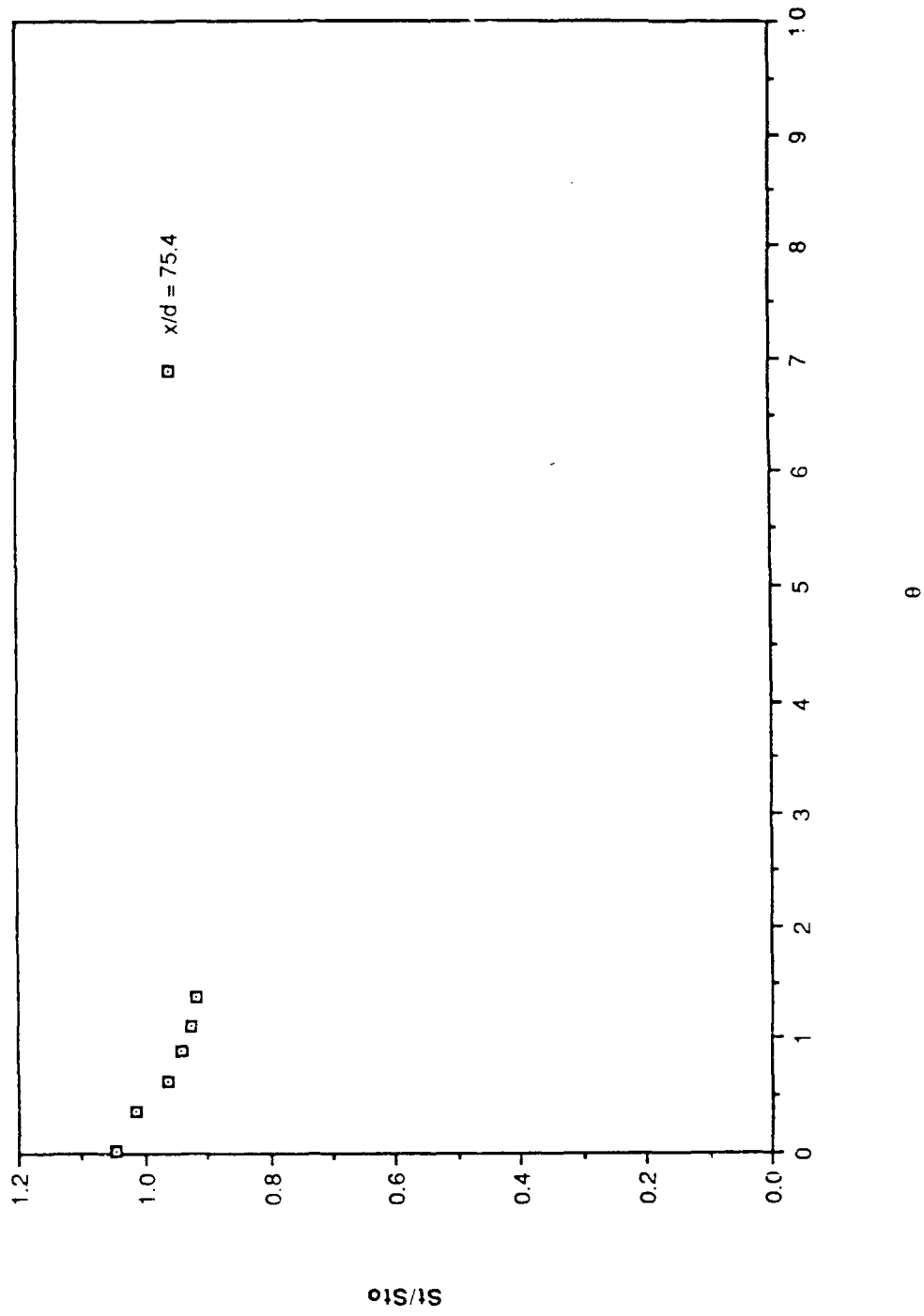


Figure 48. St/St_0 versus θ , 2 rows $m=0.5$, $x/d=75.4$, $Z=+6.35$ cm, compact

2 rows $m=0.5$ $Z=+6.35$

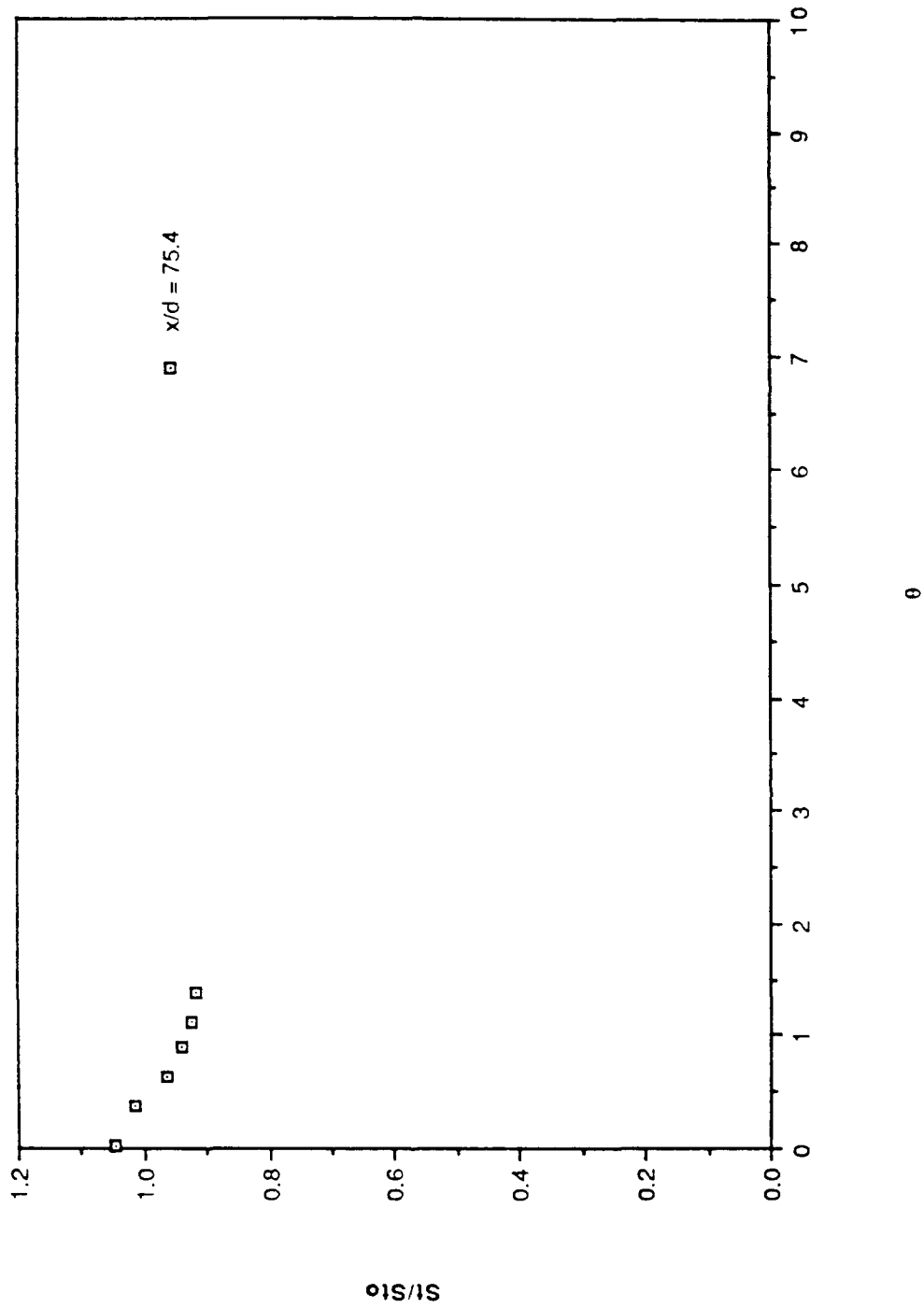


Figure 49. St/St_0 versus θ , 2 rows $m=0.5$, $x/d=75.4$, $Z=+6.35$ cm, expanded

2 rows $m=0.5$ $Z=+6.35$

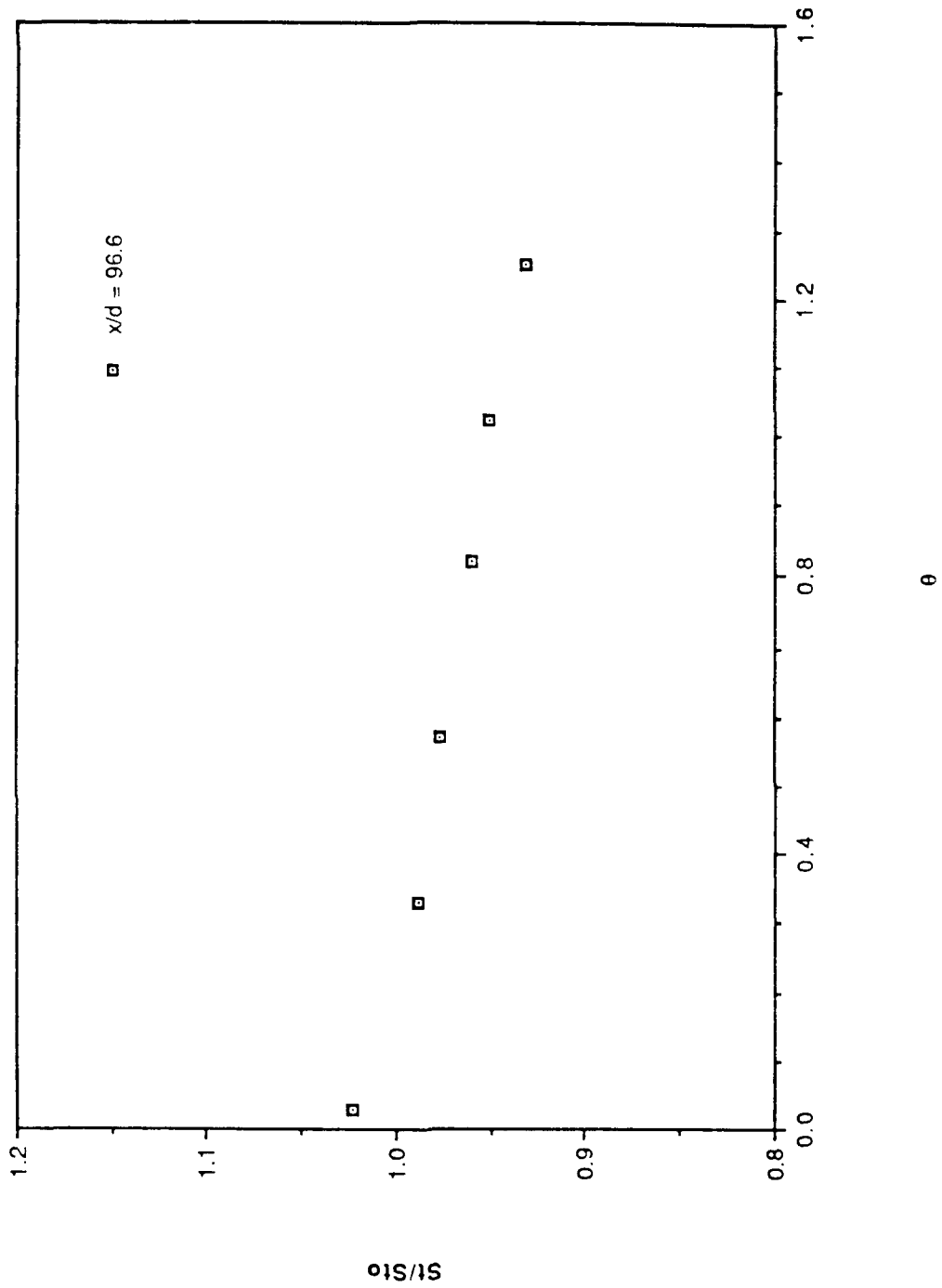


Figure 50. St/St_0 versus θ , 2 rows $m=0.5$, $x/d=96.6$, $Z=+6.35$ cm, compact

2 rows $m=0.5$ $Z=+6.35$

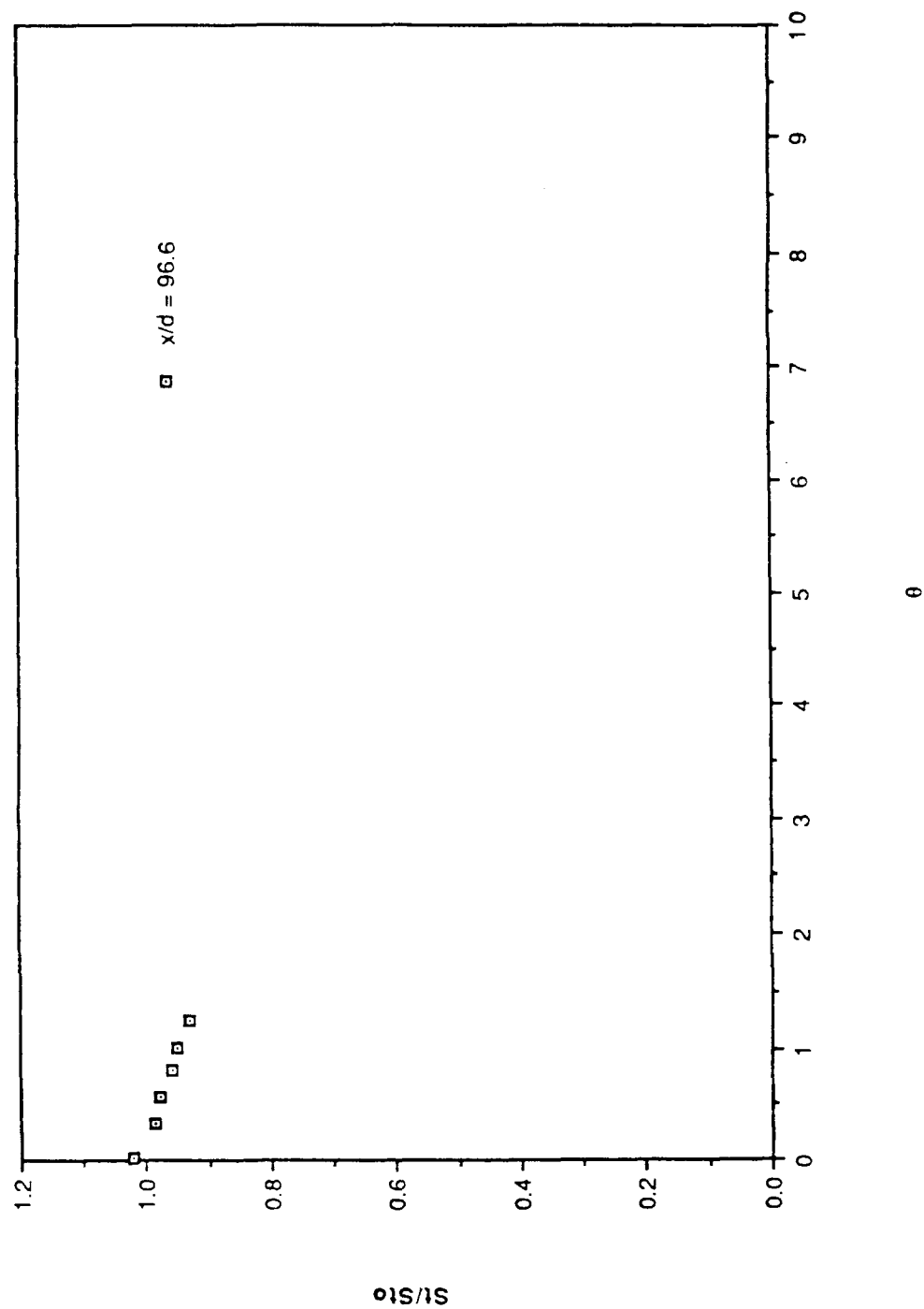


Figure 51. St/St_0 versus θ , 2 rows $m=0.5$, $x/d=96.6$, $Z=+6.35$ cm, expanded

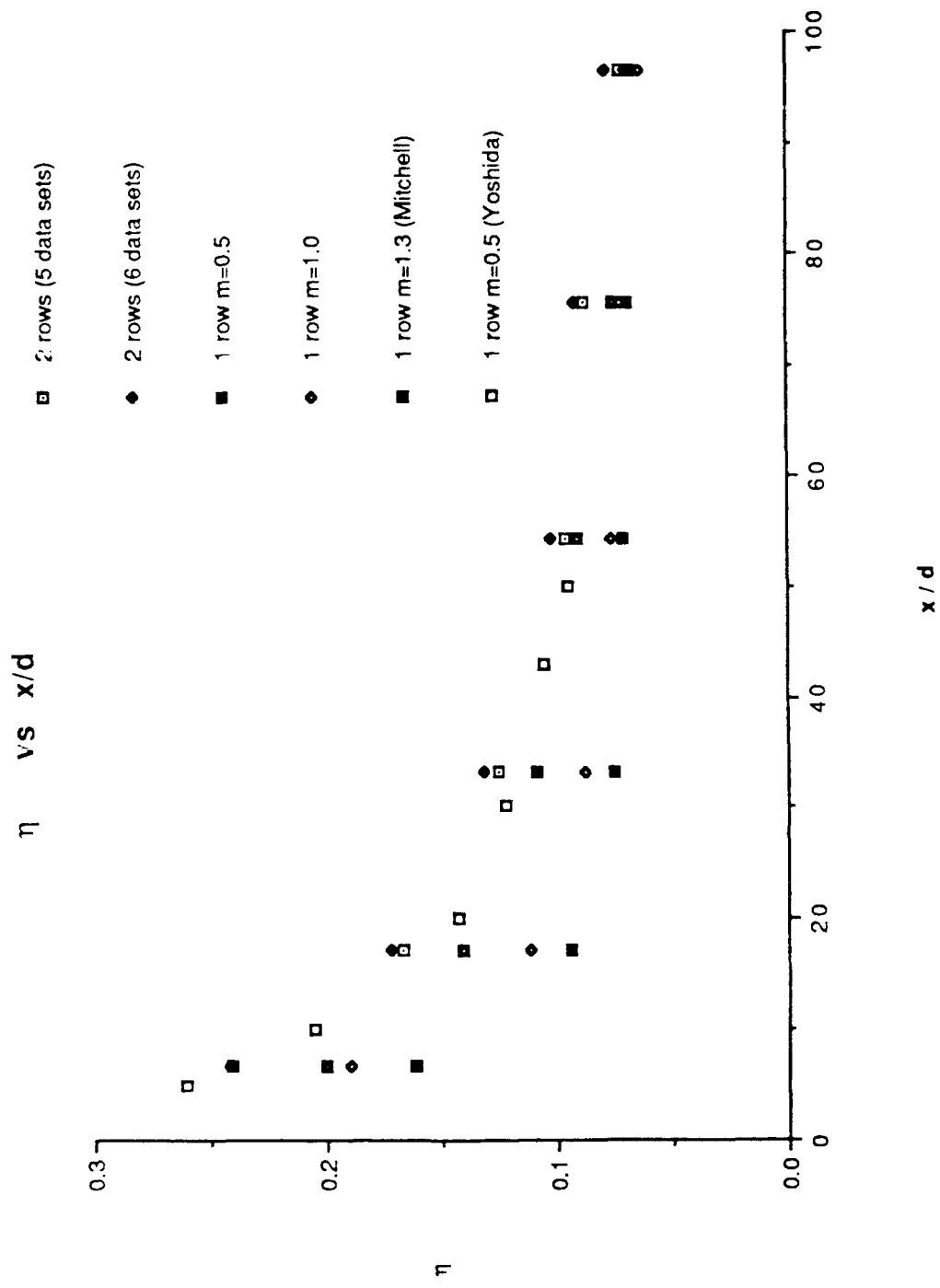


Figure 52. Comparison of η with x/d

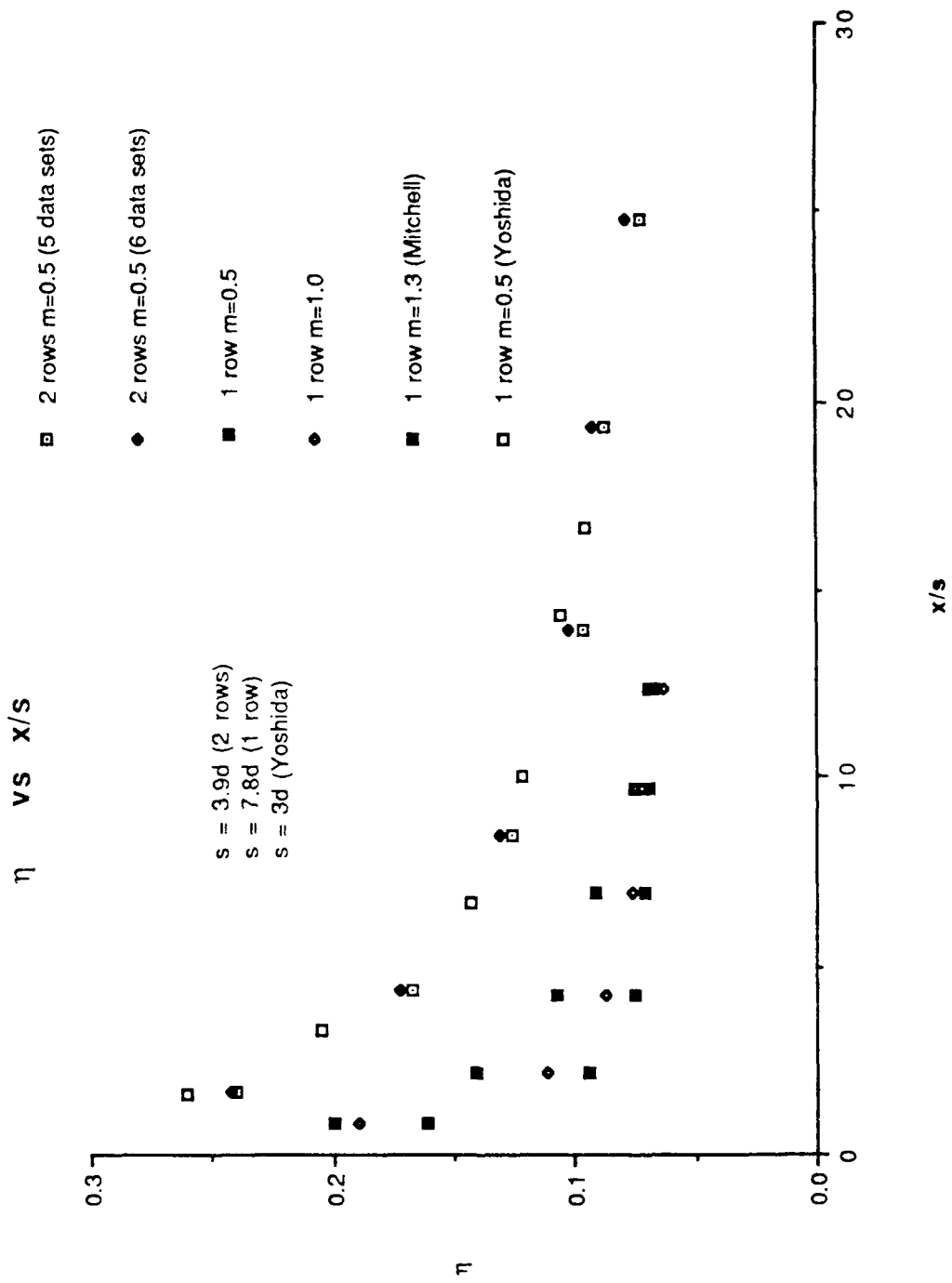


Figure 53. Comparison of η with x/s

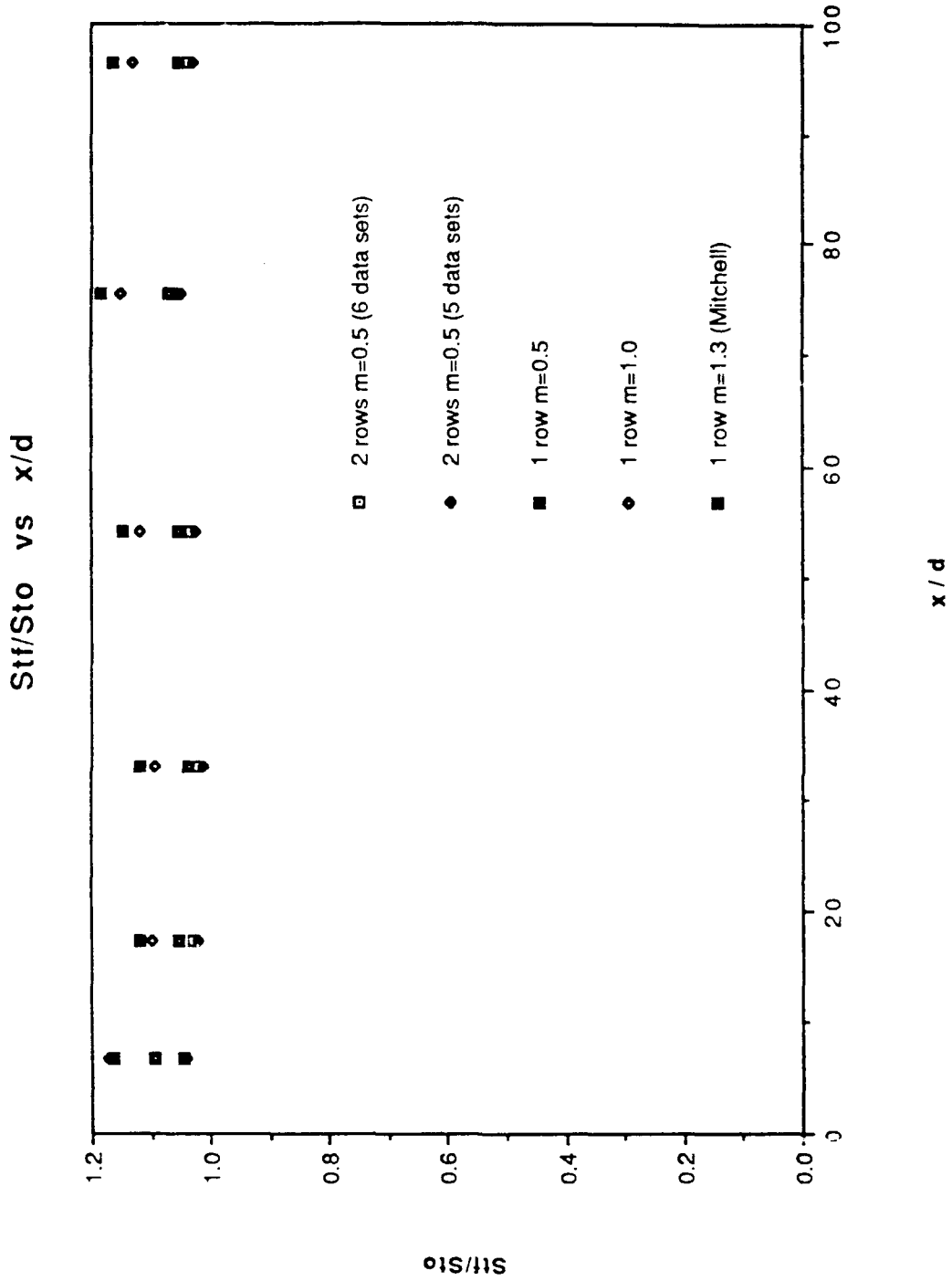
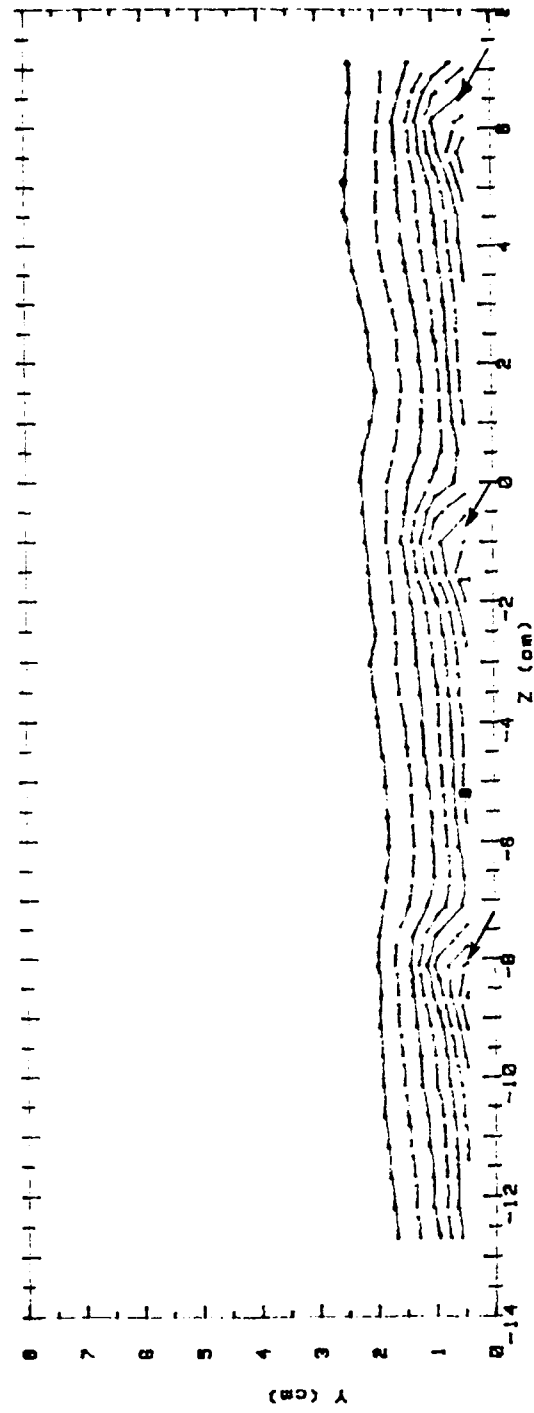


Figure 54. Comparison of St_f/St_o with x/d

RUN #00290.0914

Ux

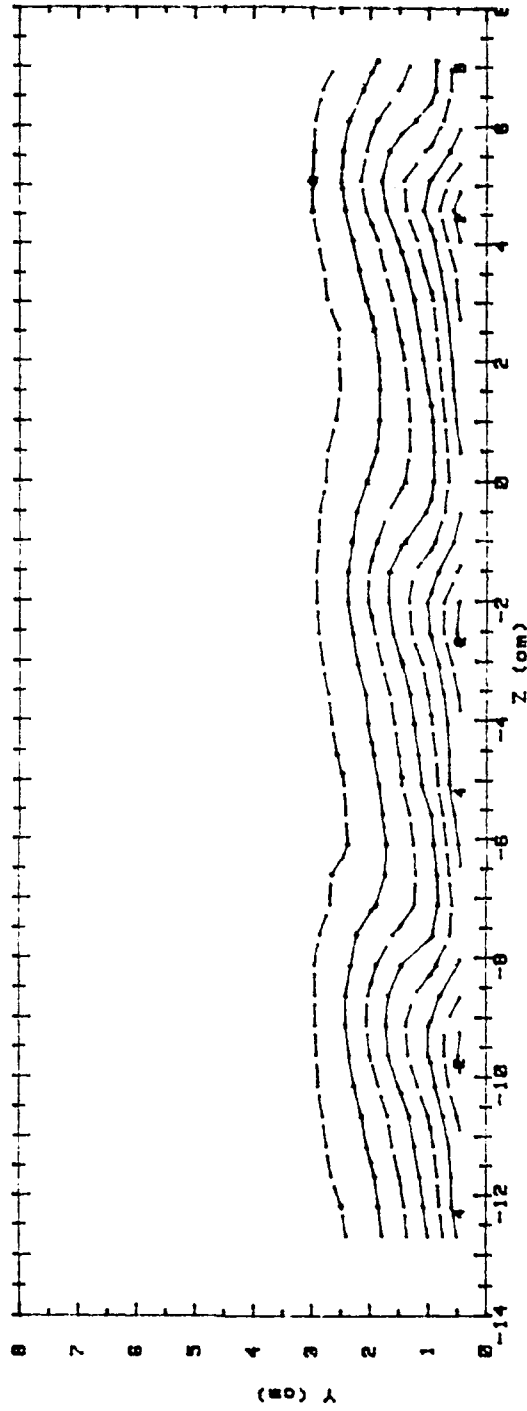


Ux (m/s)	RANGES	1	ROW	m=0.5	x/d = 10.2	
0	< 5.5	5	>	7.5	< 0	
1	5.5	< 6	6	>	8	< 0.5
2	6	< 8.5	7	>	0.5	< 0
3	8.5	< 7	8	>	8	< 0.5
4	7	< 7.5	8	>	8.5	< 10.5
			10	>	10.5	

Figure 55. Streamwise Velocity Field, 1 row m=0.5, x/d=10.2

RUN #00390.00941

Ux



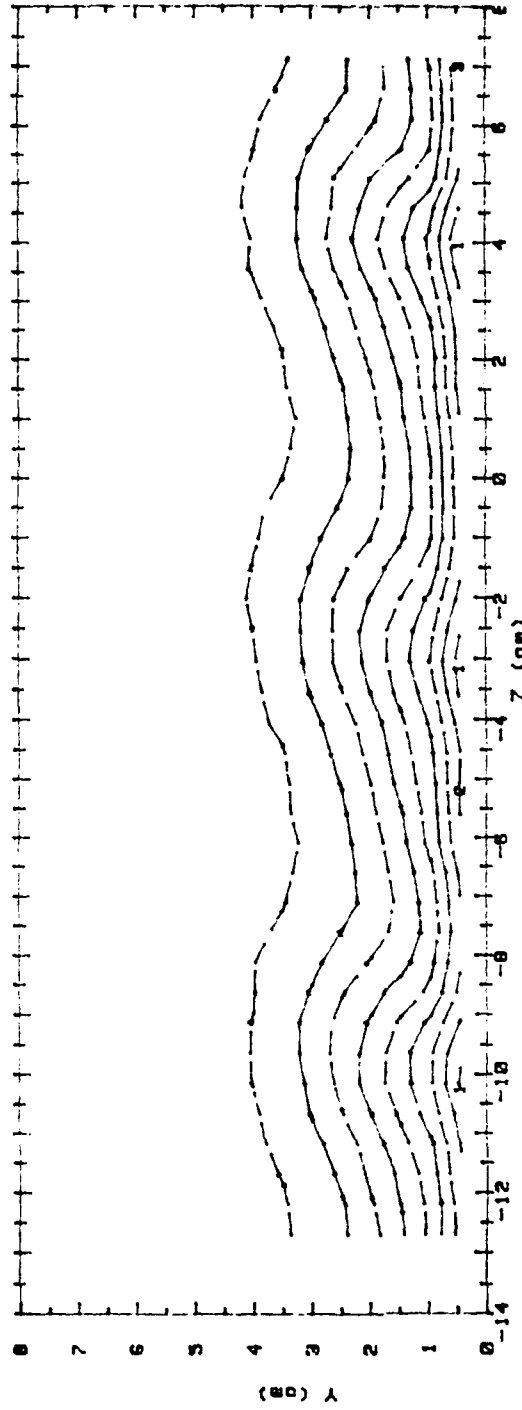
Ux(m/s) RANGES 1 ROW m=0.5 x/d = 45.8

0	< 5.5	5	> 7.5 < 8
1	> 5.5 < 6	6	> 8 < 8.5
2	> 6 < 6.5	7	> 8.5 < 9
3	> 6.5 < 7	8	> 9 < 9.5
4	> 7 < 7.5	9	> 9.5 < 10
		10	> 10

Figure 56. Streamwise Velocity Field, 1 row $m=0.5$, $x/d=45.8$

RUN #00590.1151

Ux



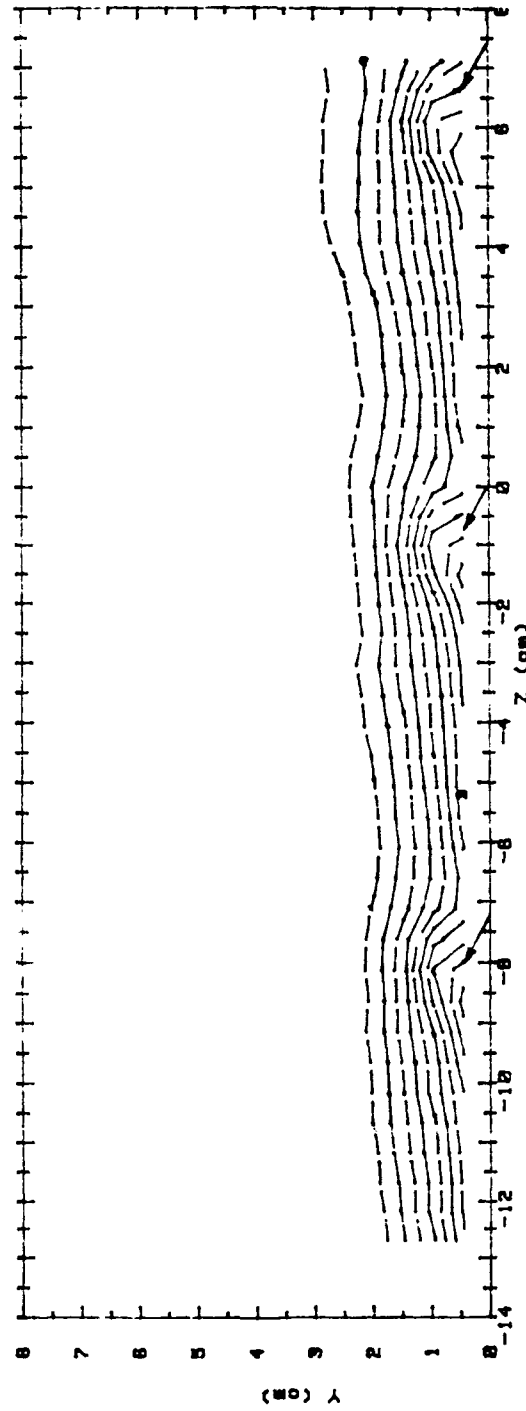
Ux(m/s) RANGES 1 ROW m=0.5 x/d = 86.8

0	< 5.5	5	> 7.5 < 8
1	> 5.5 < 6	6	> 8 < 8.5
2	> 6 < 6.5	7	> 8.5 < 9
3	> 6.5 < 7	8	> 9 < 9.5
4	> 7 < 7.5	9	> 9.5 < 10
		10	> 10

Figure 57. Streamwise Velocity Field, 1 row $m=0.5$, $x/d=86.8$

RUN #07290.0914

Ptotal



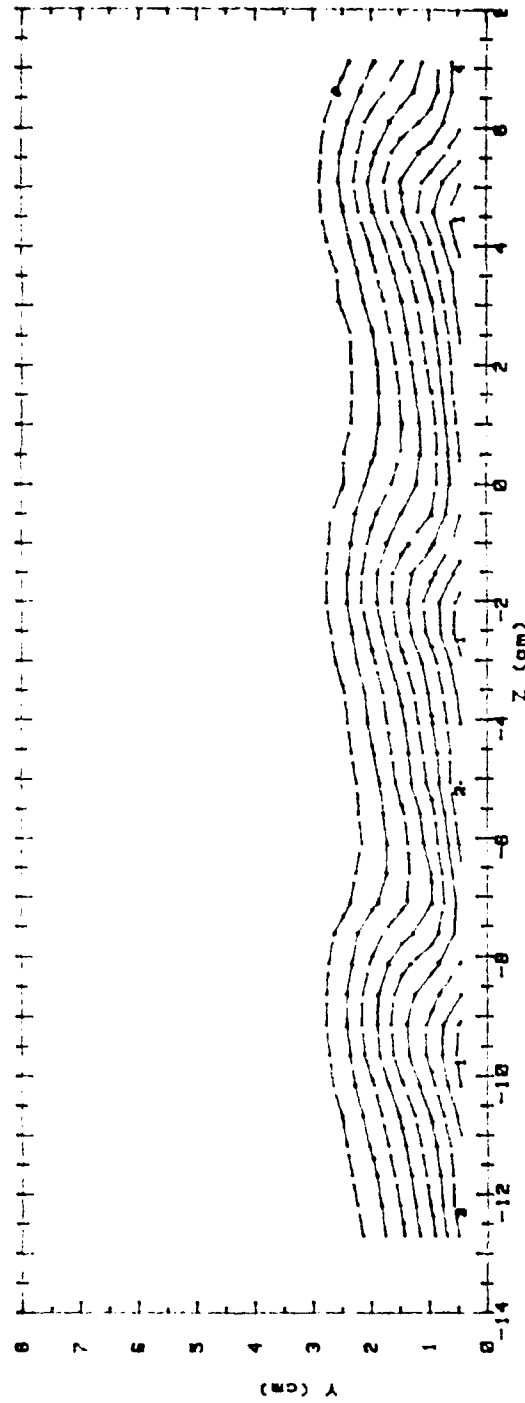
Ptotal (Pascals) RANGES 1 ROW m=0.5 x/d=10.2

0	< 20	5	> 36 < 40
1	> 20 < 24	6	> 40 < 44
2	> 24 < 28	7	> 44 < 48
3	> 28 < 32	8	> 48 < 52
4	> 32 < 36	9	> 52 < 56
		10	> 56

Figure 58. Total Pressure Field, 1 row m=0.5, x/d=10.2

RUN #00390.0941

Ptotal

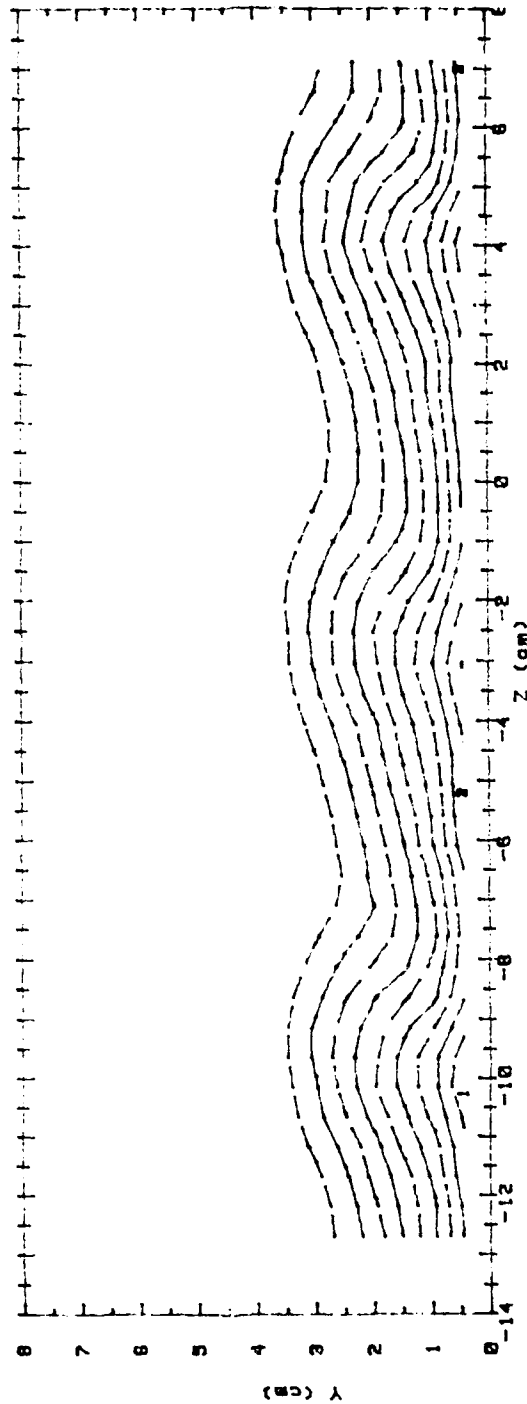


Ptotal (Pascals)	RANGES	1 ROW	m=0.5	x/d=45.8
0	< 20	5	> 36	< 40
1	> 20 < 24	8	> 40	< 44
2	> 24 < 28	7	> 44	< 48
3	> 28 < 32	8	> 48	< 52
4	> 32 < 36	8	> 52	< 56
		10	> 56	

Figure 59. Total Pressure Field, 1 row m=0.5, x/d=45.8

RUN #00590.1151

Ptotal



Ptotal(Pascals) RANGES | ROW m=0.5 x/d=86.8

0	< 20	5	36 < 40
1	20 < 24	6	40 < 44
2	24 < 28	7	44 < 48
3	28 < 32	8	48 < 52
4	32 < 36	9	52 < 56
		10	56

Figure 60. Total Pressure Field, 1 row $m=0.5$, $x/d=86.8$

RUN #00290.1847

Ux

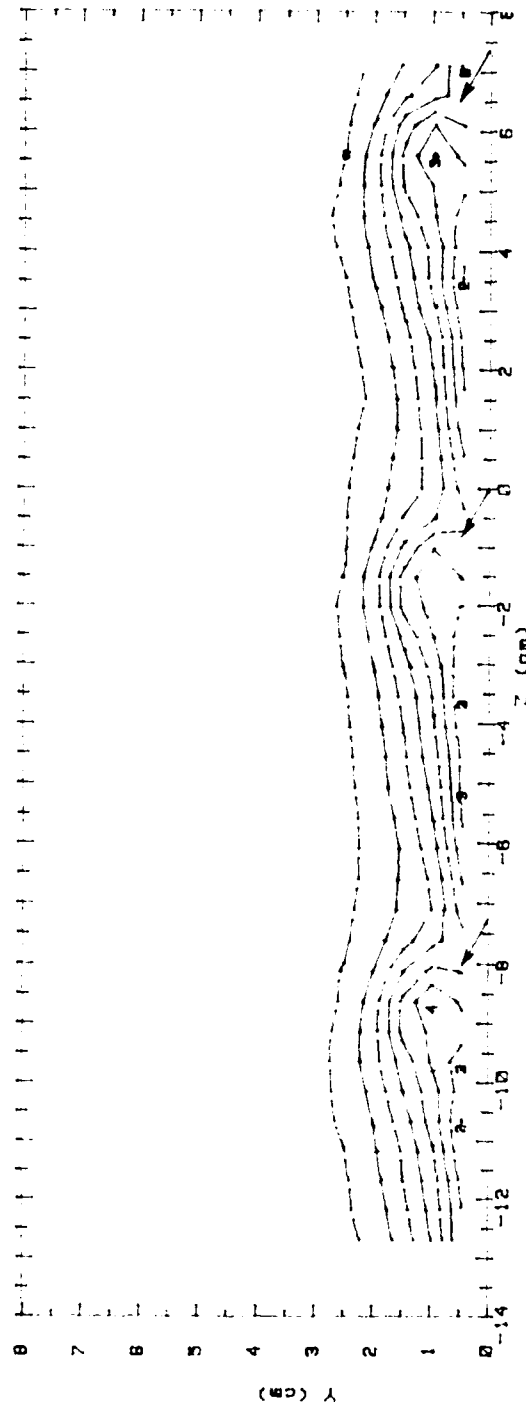
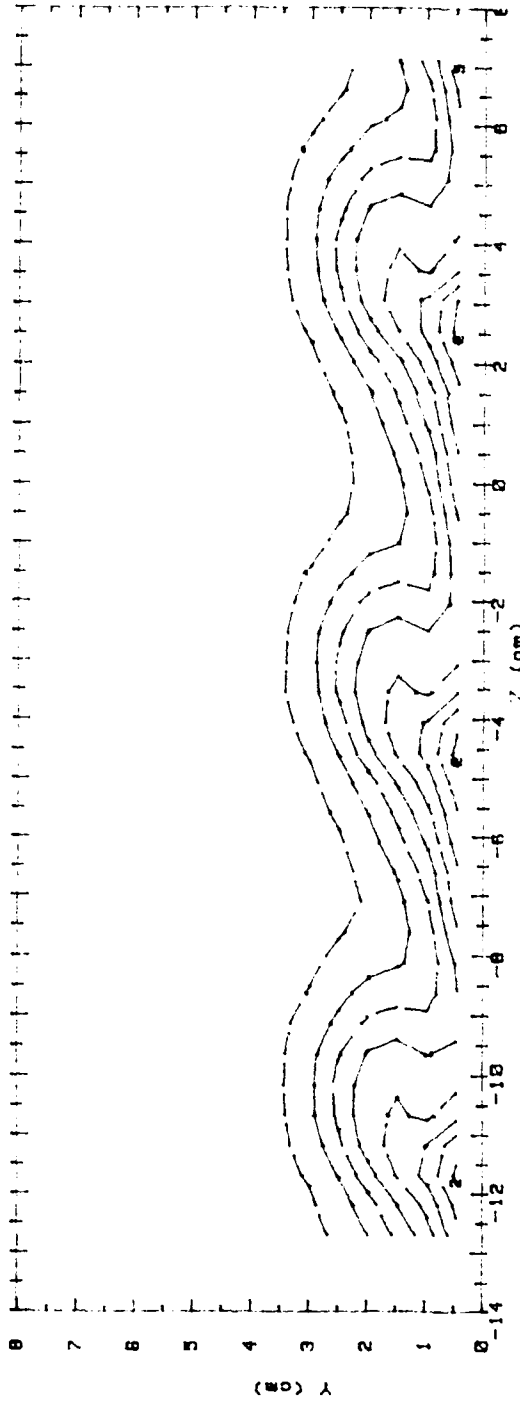


Figure 61. Streamwise Velocity Field, 1 row $m=1.0$, $x/d=10.2$

RUN #80490.1234

Ux

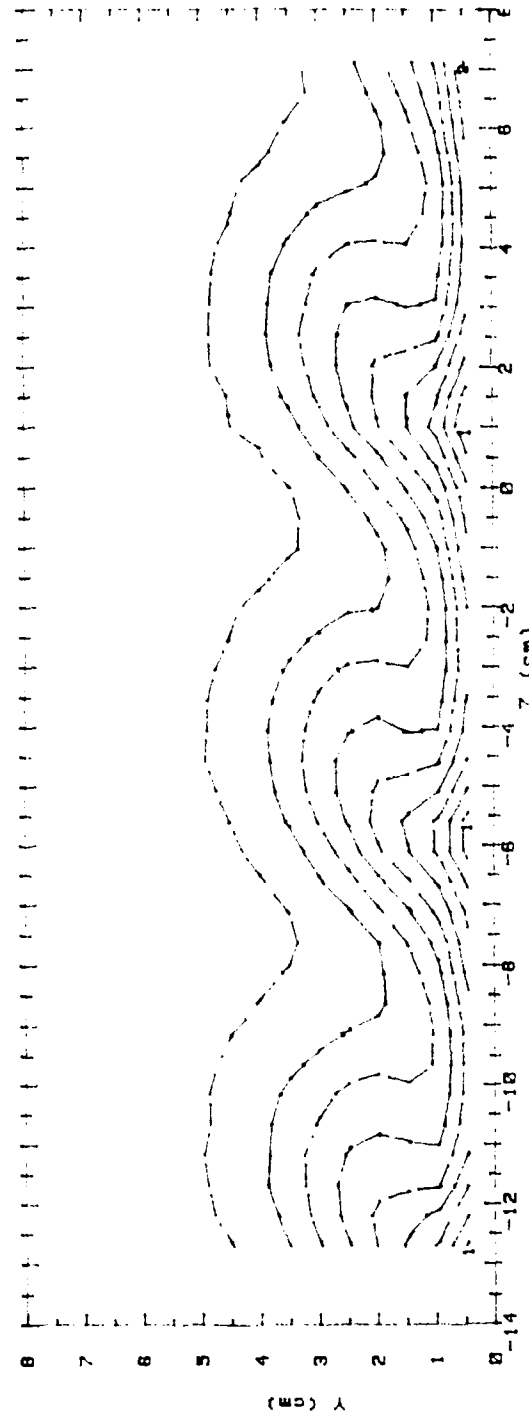


Contour Level	Velocity Range (m/s)
0	$U_x < 5.5$
1	$5.5 < U_x < 6$
2	$6 < U_x < 6.5$
3	$6.5 < U_x < 7$
4	$7 < U_x < 7.5$
5	$7.5 < U_x < 8$
6	$8 < U_x < 8.5$
7	$8.5 < U_x < 9$
8	$9 < U_x < 9.5$
9	$9.5 < U_x < 10$
10	$U_x > 10$

Figure 62. Streamwise Velocity Field, 1 row $m=1.0$, $x/d=45.8$

RUN #00590.1439

Ux



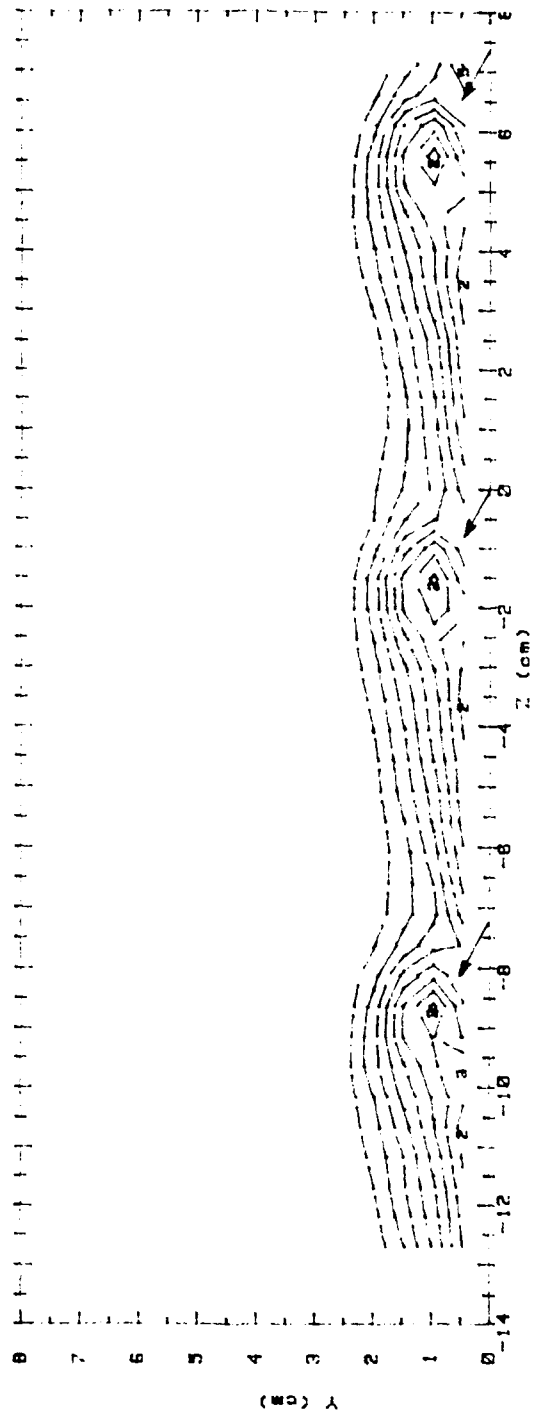
Ux(m/s) RANGES : ROW m=1.0 x/d = 86.8

0 < 5.5	5 > 7.5 < 8
1 > 5.5 < 6	6 > 8 < 8.5
2 > 6 < 6.5	7 > 8.5 < 9
3 > 6.5 < 7	8 > 9 < 9.5
4 > 7 < 7.5	9 > 9.5 < 10
	10 > 10

Figure 63. Streamwise Velocity Field, 1 row $m=1.0$, $x/d=86.8$

RUN #00290.1847

Ptotal



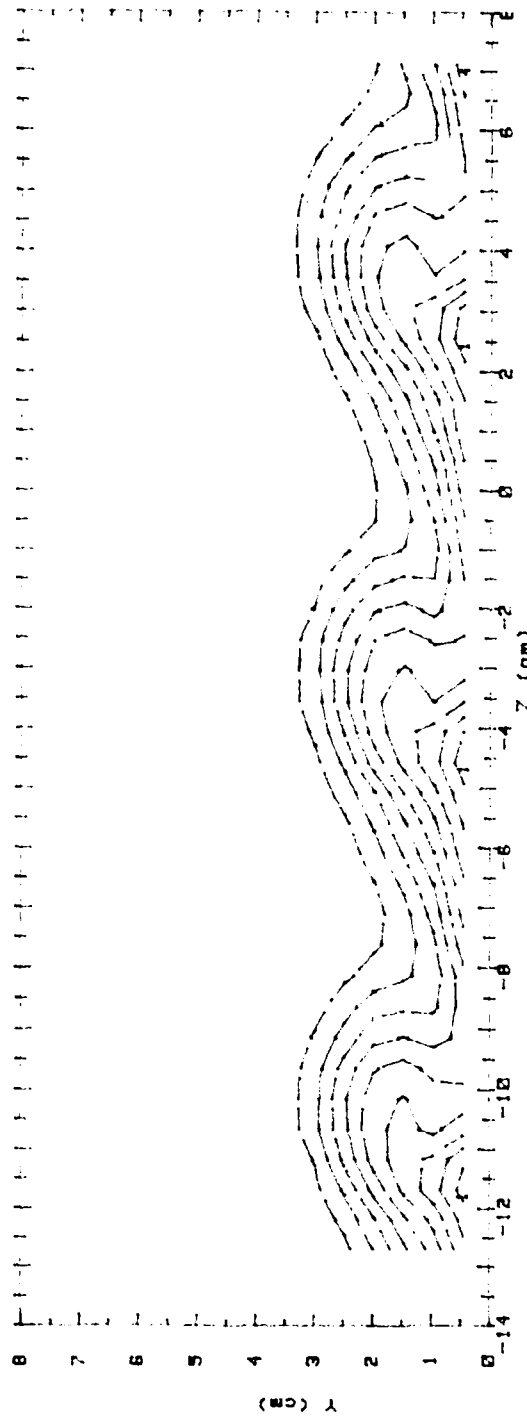
Ptotal(Pascals) RANGES 1 ROW m=1.0 x/d=10.2

0	< 20	5	> 36	< 40	
1	> 20	< 24	6	> 40	< 44
2	> 24	< 28	7	> 44	< 48
3	> 28	< 32	8	> 48	< 52
4	> 32	< 36	8	> 52	< 56
			10	> 56	

Figure 64. Total Pressure Field, 1 row $m=1.0$, $x/d=10.2$

RUN #80490.1234

Ptotal



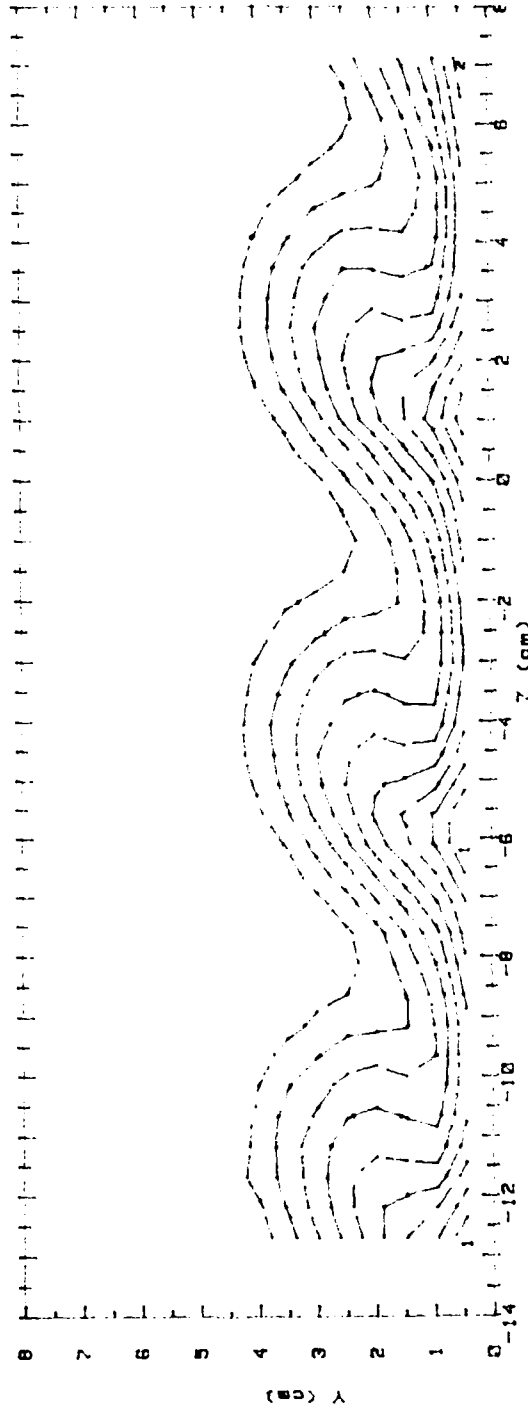
Ptotal(Pascals) RANGES : ROW m=1.0 x/d=45.8

0 1	< 20	5 1	36 < 40
1 1	20 < 24	6 1	40 < 44
2 1	24 < 28	7 1	44 < 48
3 1	28 < 32	8 1	48 < 52
4 1	32 < 36	9 1	52 < 56
		10 1	56

Figure 65. Total Pressure Field, 1 row $m=1.0$, $x/d=45.8$

RUN #80590.1439

Ptotal



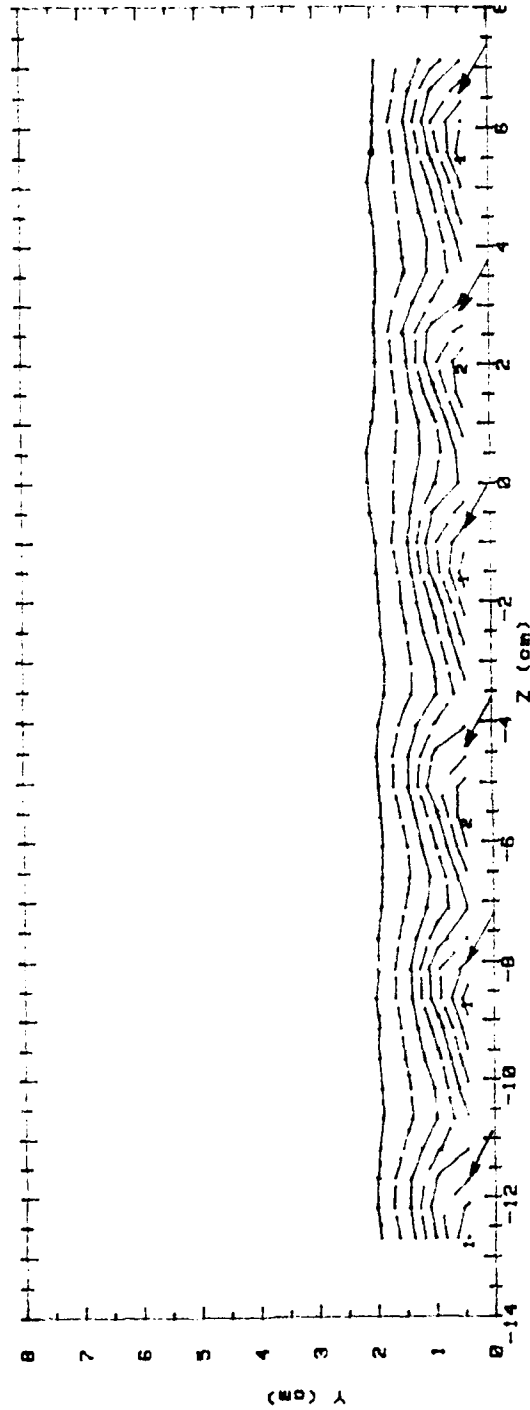
Ptotal(Pascals) RANGES : ROW m=1.0 x/d=86.8

0	< 20	5	36 < 40
1	20 < 24	6	40 < 44
2	24 < 28	7	44 < 48
3	28 < 32	8	48 < 52
4	32 < 36	9	52 < 56
		10	56

Figure 66. Total Pressure Field, 1 row $m=1.0$, $x/d=86.8$

RUN #80490.1837

Ux

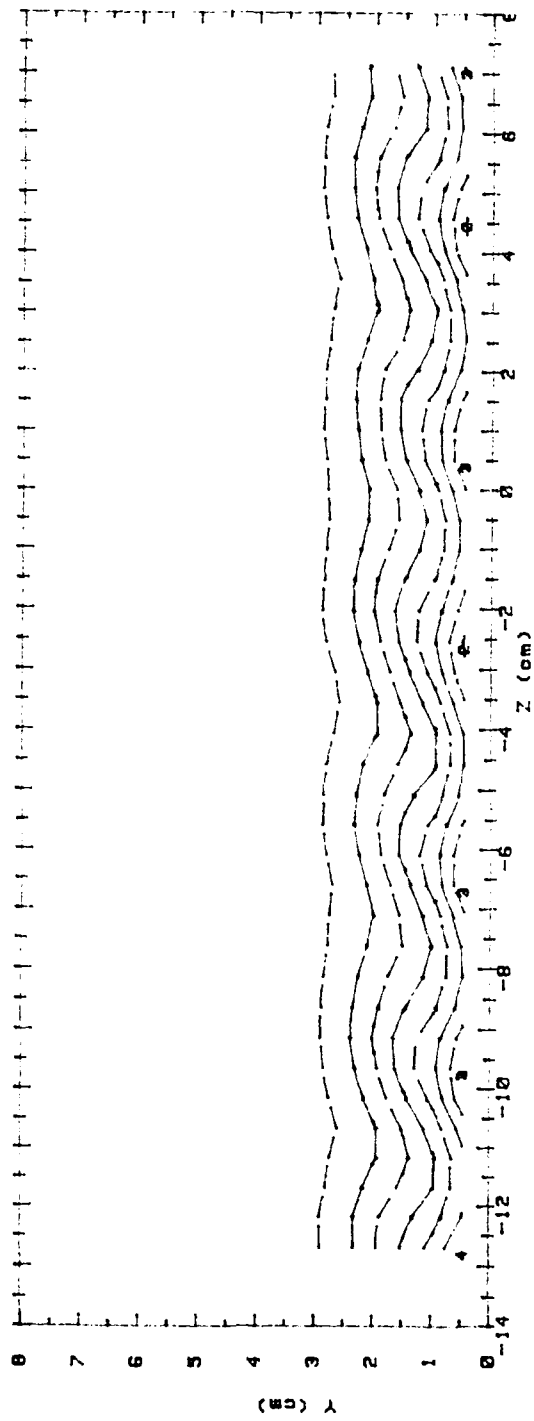


Ux (m/s)	RANGES	2 ROWS	m=0.5	x/d = 10.2
0	< 5.5	5	> 7.5	< 8
1	5.5 < 6	6	> 8	< 8.5
2	6 < 6.5	7	> 8.5	< 8
3	6.5 < 7	8	> 9	< 9.5
4	7 < 7.5	9	> 9.5	< 10.5
		10	> 10.5	

Figure 67. Streamwise Velocity Field, 2 rows m=0.5, x/d=10.2

RUN #00490.1531

Ux



Ux (m/s) RANGES 2 ROWS m=0.5 x/d = 45.8

0	< 5.5	5	> 7.5 < 8
1	> 5.5 < 6	6	> 8 < 8.5
2	> 6 < 6.5	7	> 8.5 < 9
3	> 6.5 < 7	8	> 9 < 9.5
4	> 7 < 7.5	9	> 9.5 < 10
		10	> 10

Figure 68. Streamwise Velocity Field, 2 rows m=0.5, x/d=45.8

RUN #80590.0857

Ux

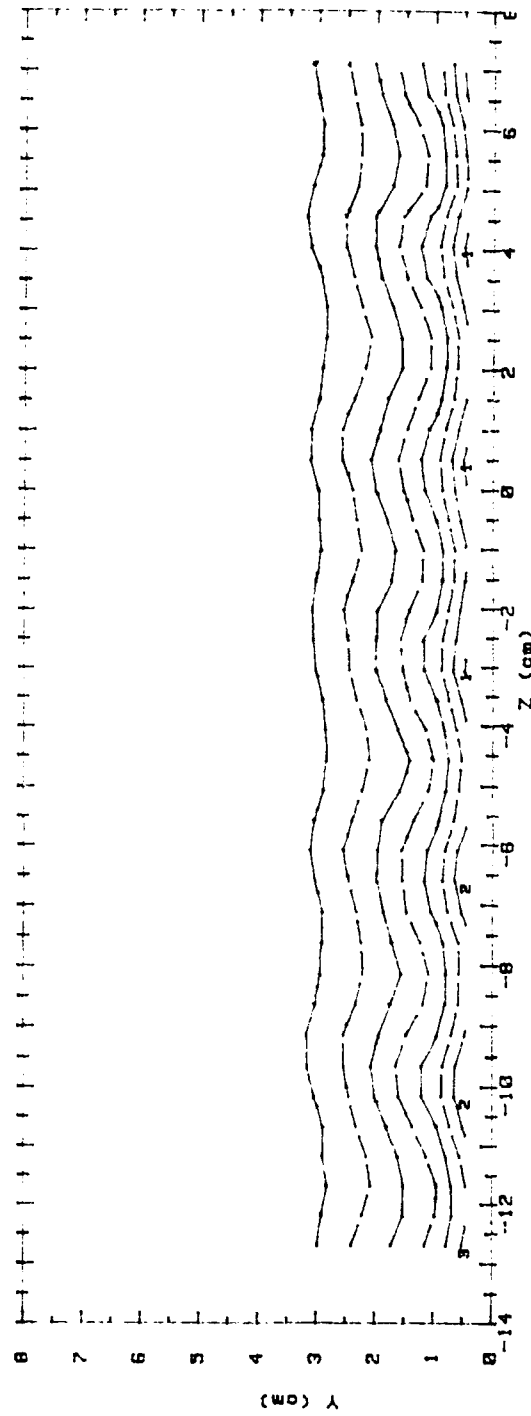
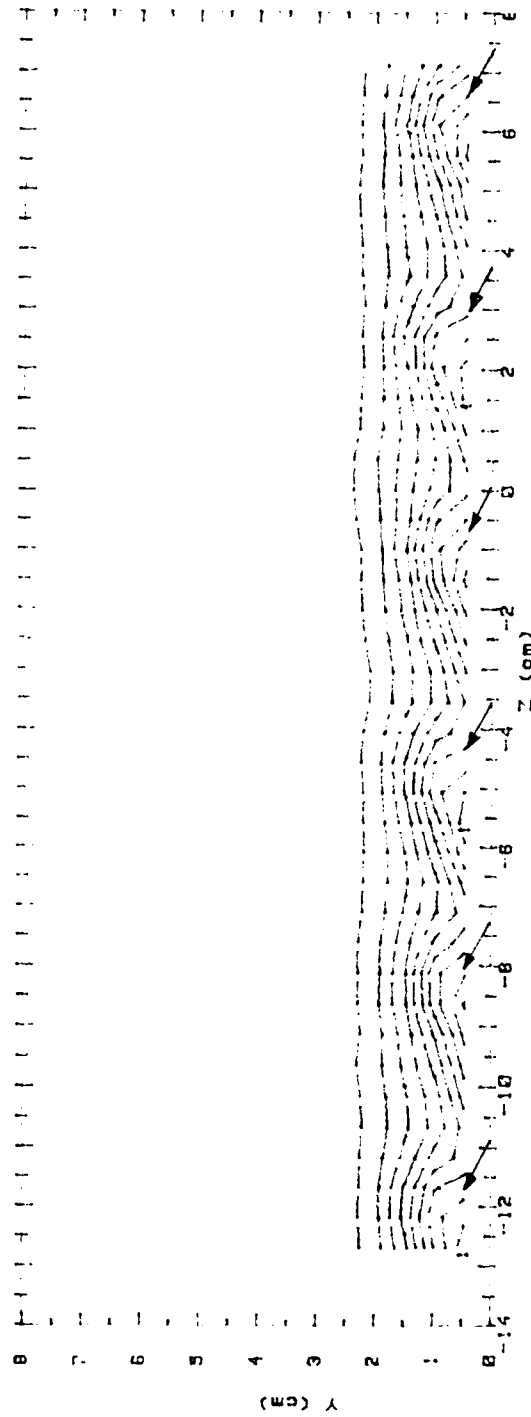


Figure 69. Streamwise Velocity Field, 2 rows $m=0.5$, $x/d=86.8$

RUN #80490.1837

Ptotal



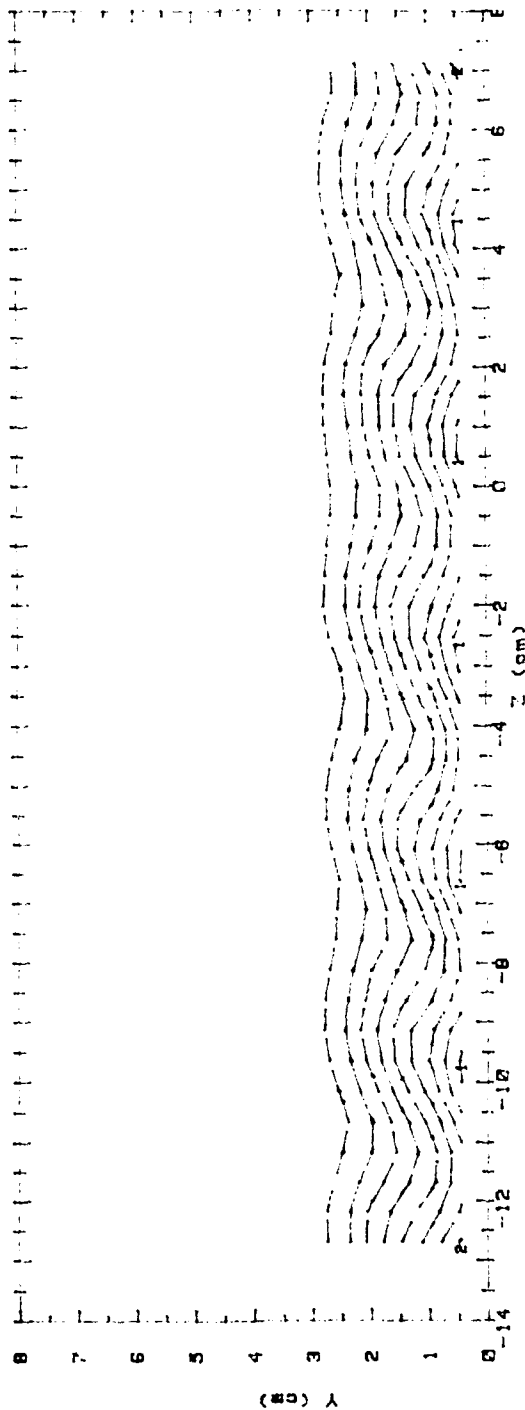
Ptotal (Pascals) RANGES 2 ROWS m=0.5 x/d=10.2

0 1	< 20	5 1	36	< 40	
1 1	20	< 24	6 1	40	< 44
2 1	24	< 28	7 1	44	< 48
3 1	28	< 32	8 1	48	< 52
4 1	32	< 36	9 1	52	< 56
			10 1	56	

Figure 70. Total Pressure Field, 2 rows m=0.5, x/d=10.2

RUN #80490.1531

Ptotal



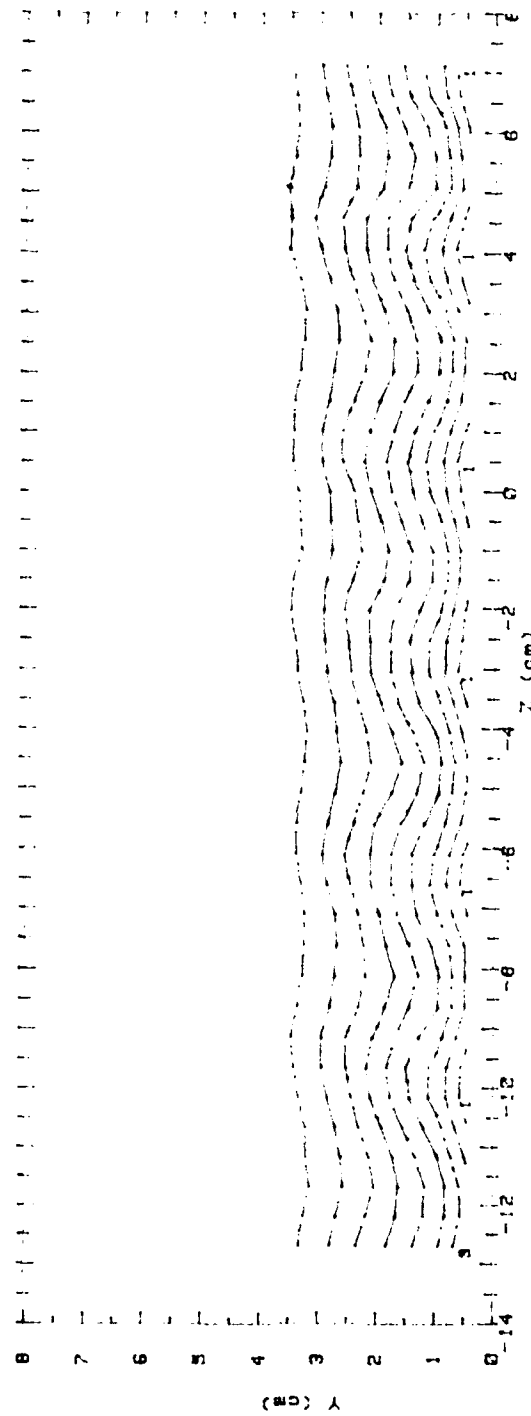
Ptotal(Pascals) RANGES 2 ROWS m=0.5 x/d=45.8

0 1	< 20	5 1	36 < 40
1 1	20 < 24	6 1	40 < 44
2 1	24 < 28	7 1	44 < 48
3 1	28 < 32	8 1	48 < 52
4 1	32 < 36	9 1	52 < 56
		10 1	56

Figure 71. Total Pressure Field, 2 rows $m=0.5$, $x/d=45.8$

RUN #80590.0857

Ptotal



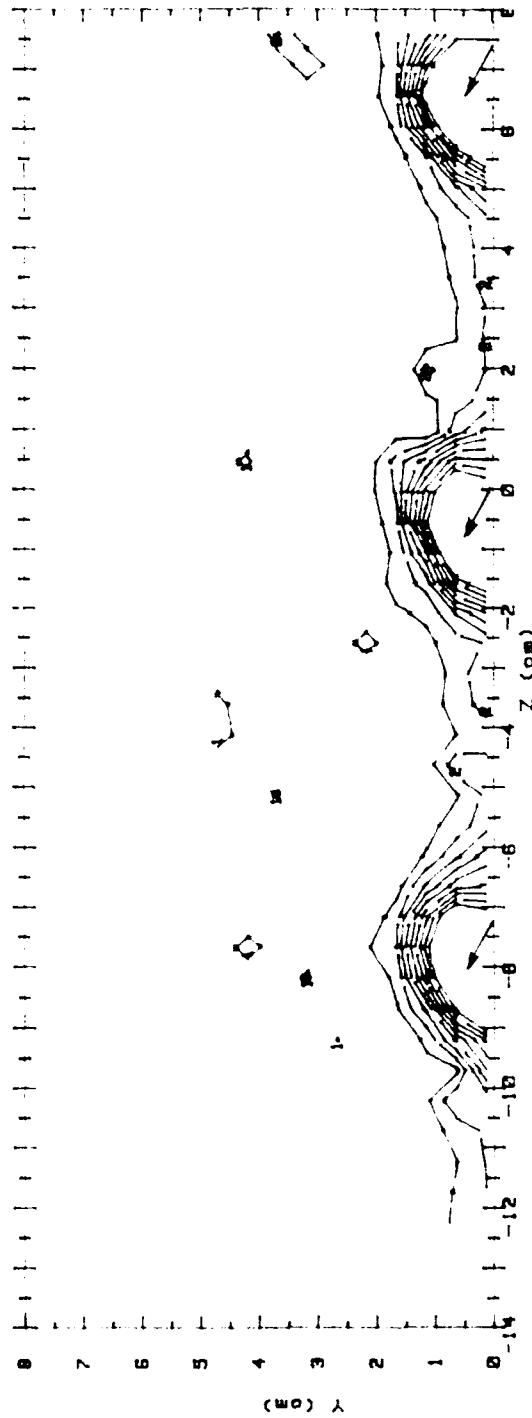
Ptotal (Pascals) RANGES 2 ROWS m=0.5 x/d=86.8

0 < 20	5 > 36 < 40
1 > 20 < 24	6 > 40 < 44
2 > 24 < 28	7 > 44 < 48
3 > 28 < 32	8 > 48 < 52
4 > 32 < 36	9 > 52 < 56
	10 > 56

Figure 72. Total Pressure Field, 2 rows $m=0.5$, $x/d=86.8$

RUN #80790.1732

T - Tfs



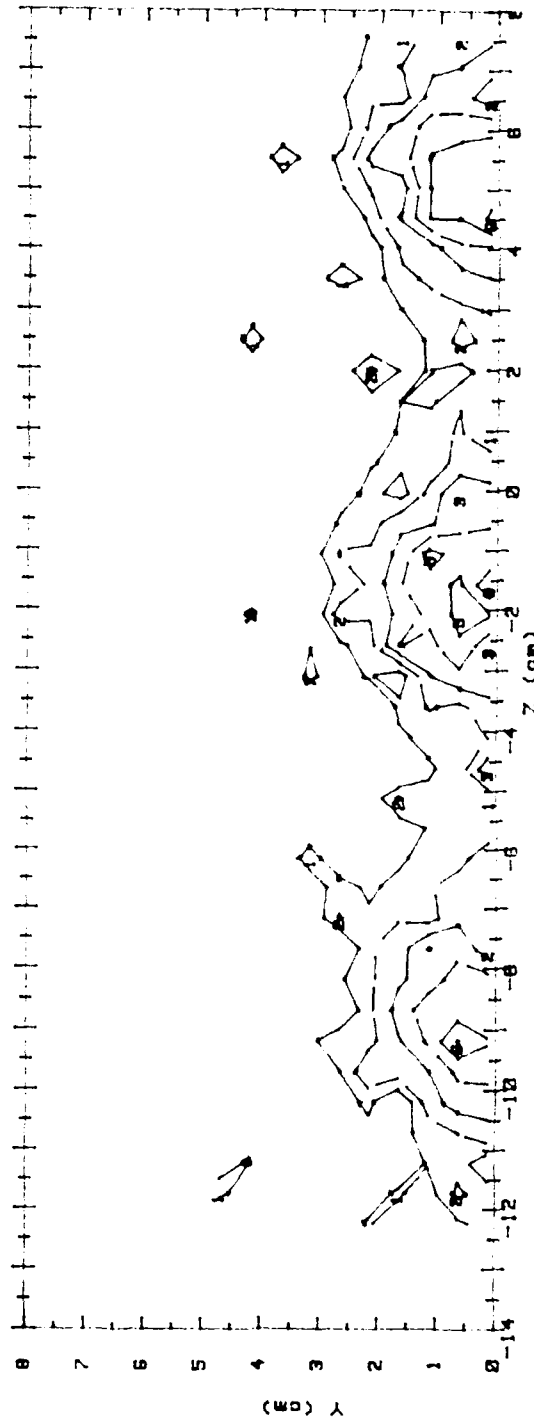
T - Tfs (CELCIUS) RANGES | ROW m=0.5 x/d = 10.2

0	< .5	5	2.5 < 3
1	.5 < 1	6	3 < 3.5
2	1 < 1.5	7	3.5 < 4
3	1.5 < 2	8	4 < 4.5
4	2 < 2.5	9	4.5

Figure 73. Local Injectant Distribution, 1 row m=0.5, x/d=10.2

RUN #80790.1553

T -- Tfs



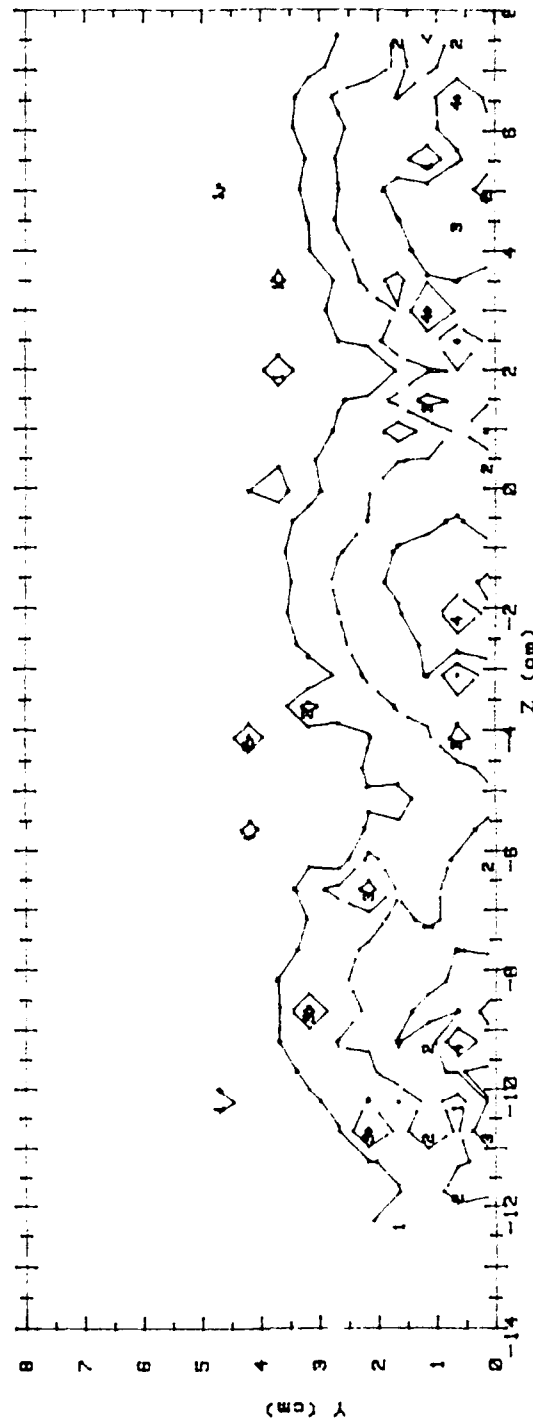
T -- Tfs (CELCIUS) RANGES 1 ROW m=0.5 x/d = 45.8

0 1	< .5	5 1	> 2.5	< 3	
1 1	> .5	< 1	6 1	> 3	< 3.5
2 1	> 1	< 1.5	7 1	> 3.5	< 4
3 1	> 1.5	< 2	8 1	> 4	< 4.5
4 1	> 2	< 2.5	8 1	> 4.5	

Figure 74. Local Injectant Distribution, 1 row m=0.5, x/d=45.8

RUN #80690.2108

T - Tfs



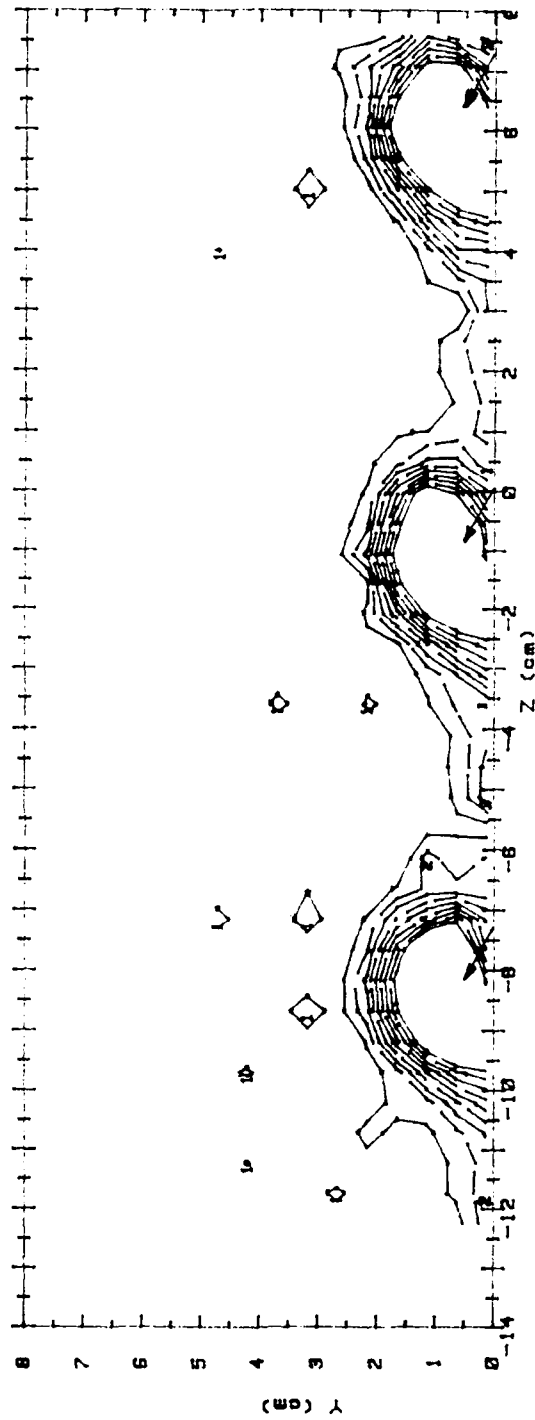
T - Tfs (CELCIUS) RANGES 1 ROW m=0.5 x/d = 86.8

0 :	< .5	5 :	2.5 < 3
1 :	.5 < 1	6 :	3 < 3.5
2 :	1 < 1.5	7 :	3.5 < 4
3 :	1.5 < 2	8 :	4 < 4.5
4 :	2 < 2.5	8 :	4.5

Figure 75. Local Injectant Distribution, 1 row m=0.5, x/d=86.8

RUN #80790.1906

T - Tfs



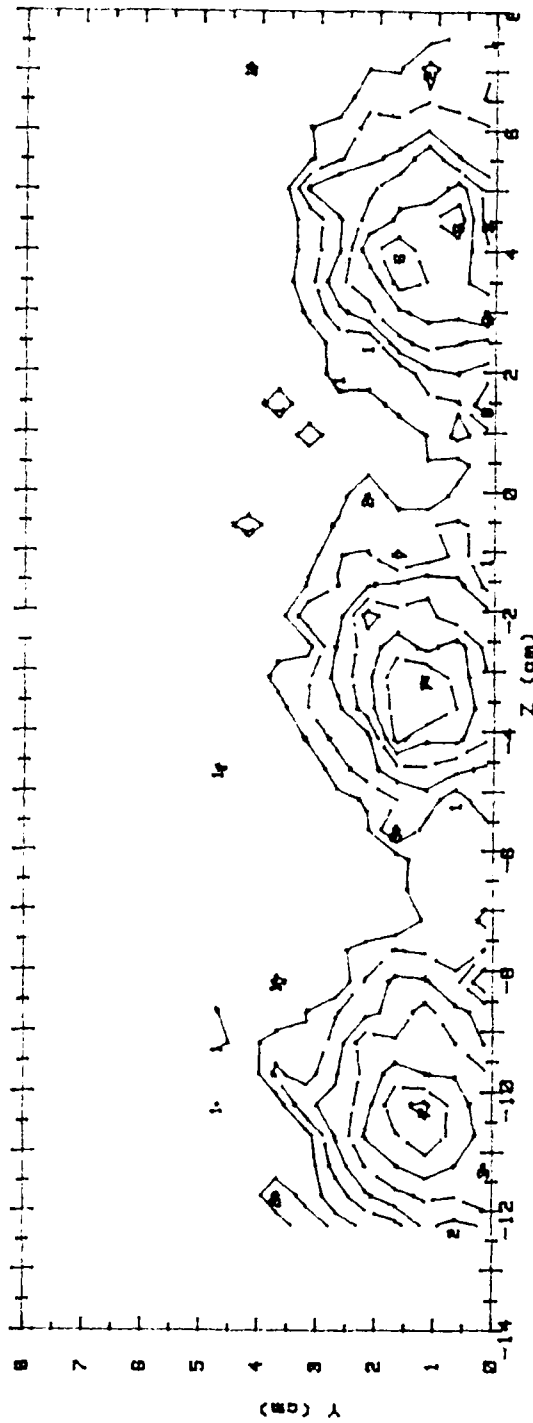
T - Tfs (CELCIUS) RANGES 1 ROW m=1.0 x/d = 10.2

0	< .5	5	> 2.5 < 3
1	> .5 < 1	6	> 3 < 3.5
2	> 1 < 1.5	7	> 3.5 < 4
3	> 1.5 < 2	8	> 4 < 4.5
4	> 2 < 2.5	8	> 4.5

Figure 76. Local Injectant Distribution, 1 row m=1.0, x/d=10.2

RUN #80790.1415

T - Tfs



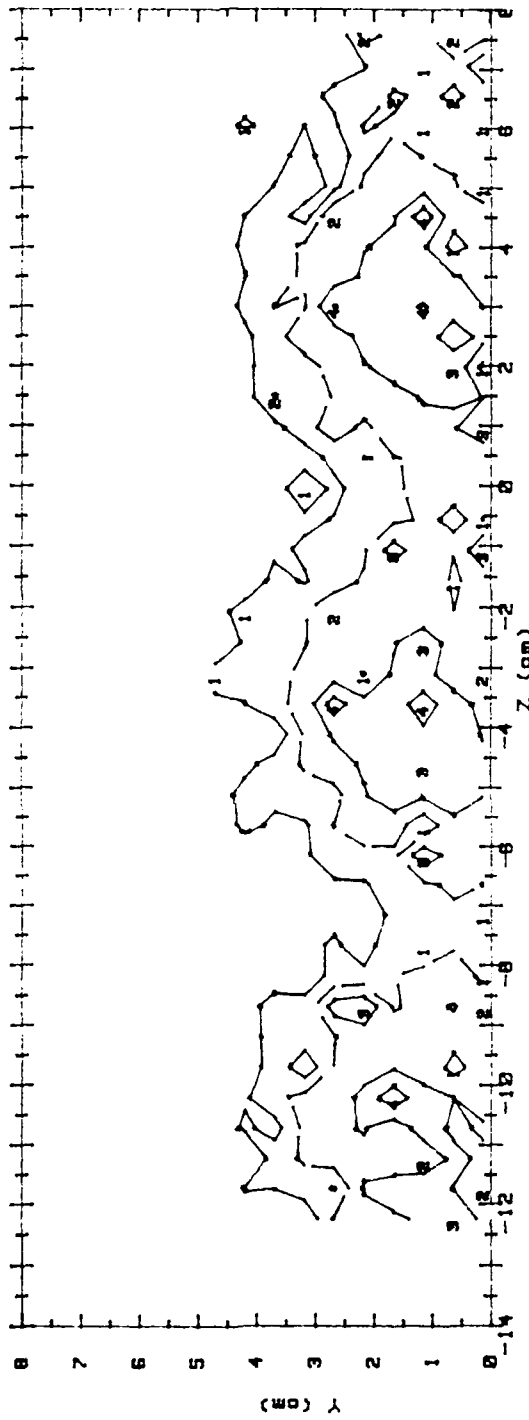
T - Tfs(CELCIUS) RANGES 1 ROW m=1.0 x/d = 45.8

0 :	< .5	5 :	2.5 < 3
1 :	.5 < 1	6 :	3 < 3.5
2 :	1 < 1.5	7 :	3.5 < 4
3 :	1.5 < 2	8 :	4 < 4.5
4 :	2 < 2.5	9 :	4.5

Figure 77. Local Injectant Distribution, 1 row m=1.0, x/d=45.8

RUN #80790.0822

T - Tfs



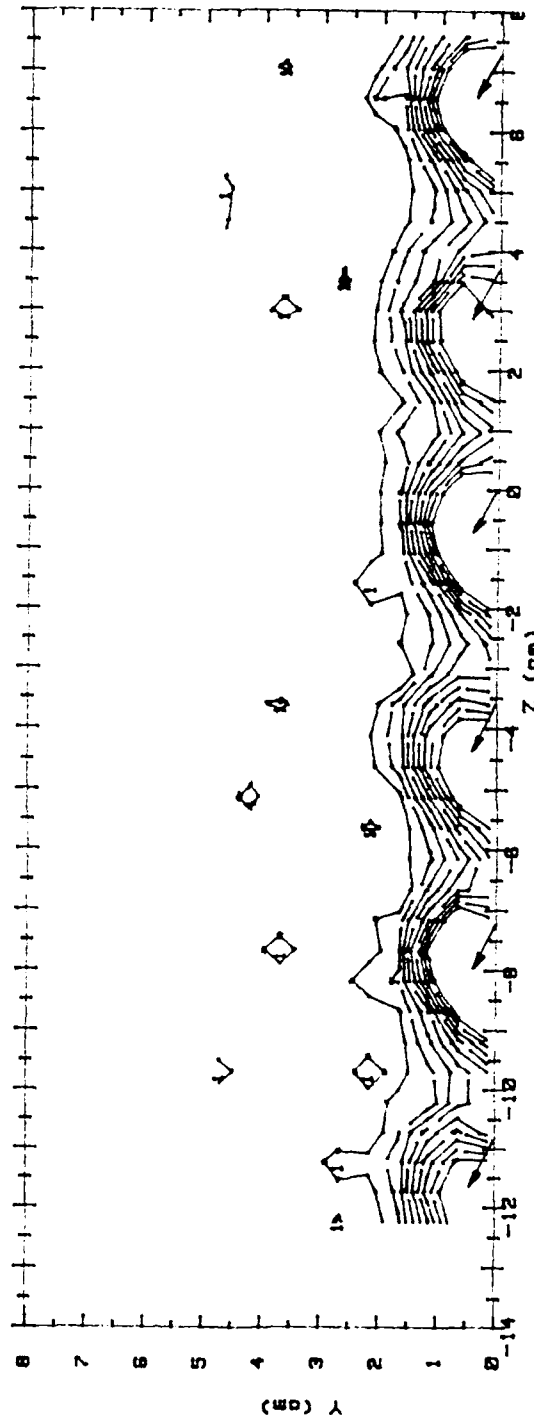
T - Tfs(CELCIUS) RANGES 1 ROW m=1.0 x/d = 86.8

0 :	< .5	5 :	2.5 < 3
1 :	.5 < 1	6 :	3 < 3.5
2 :	1 < 1.5	7 :	3.5 < 4
3 :	1.5 < 2	8 :	4 < 4.5
4 :	2 < 2.5	8 :	4.5

Figure 78. Local Injectant Distribution, 1 row m=1.0, x/d=86.8

RUN #80790.2035

T - Tfs



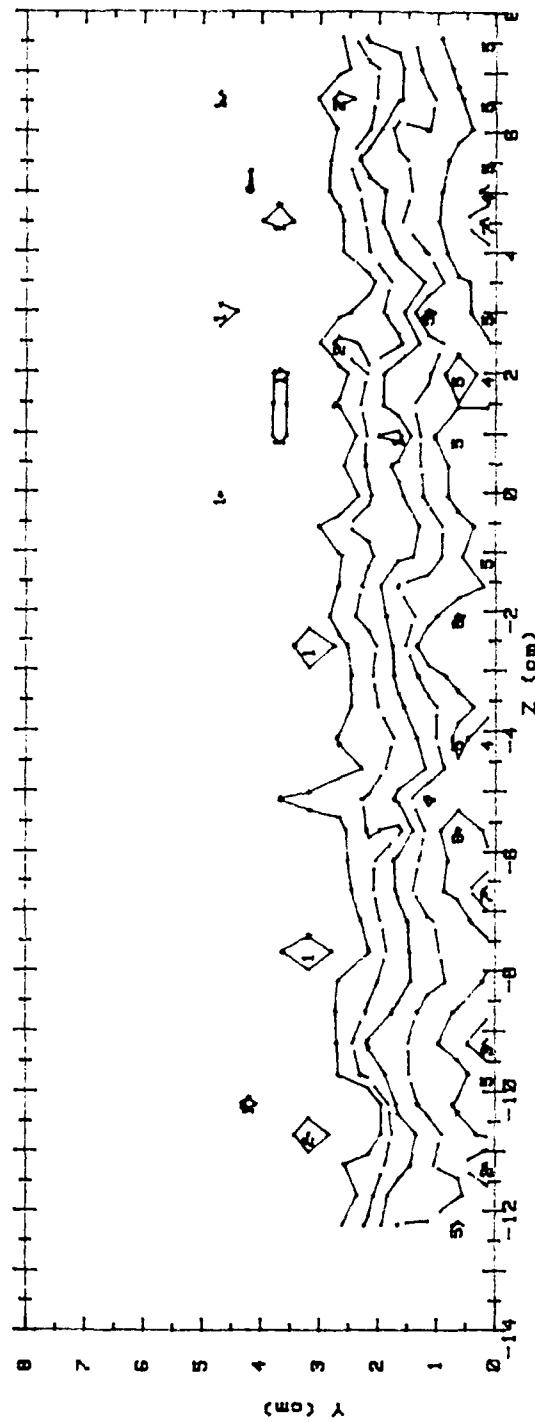
T - Tfs (CELCIUS) RANGES 2 ROWS m=0.5 x/d = 10.2

0 1	< .5	5 1	2.5 < 3
1 1	.5 < 1	6 1	3 < 3.5
2 1	1 < 1.5	7 1	3.5 < 4
3 1	1.5 < 2	8 1	4 < 4.5
4 1	2 < 2.5	8 1	4.5

Figure 79. Local Injectant Distribution, 2 rows $m=0.5$, $x/d=10.2$

RUN #80790.1252

T - Tfs



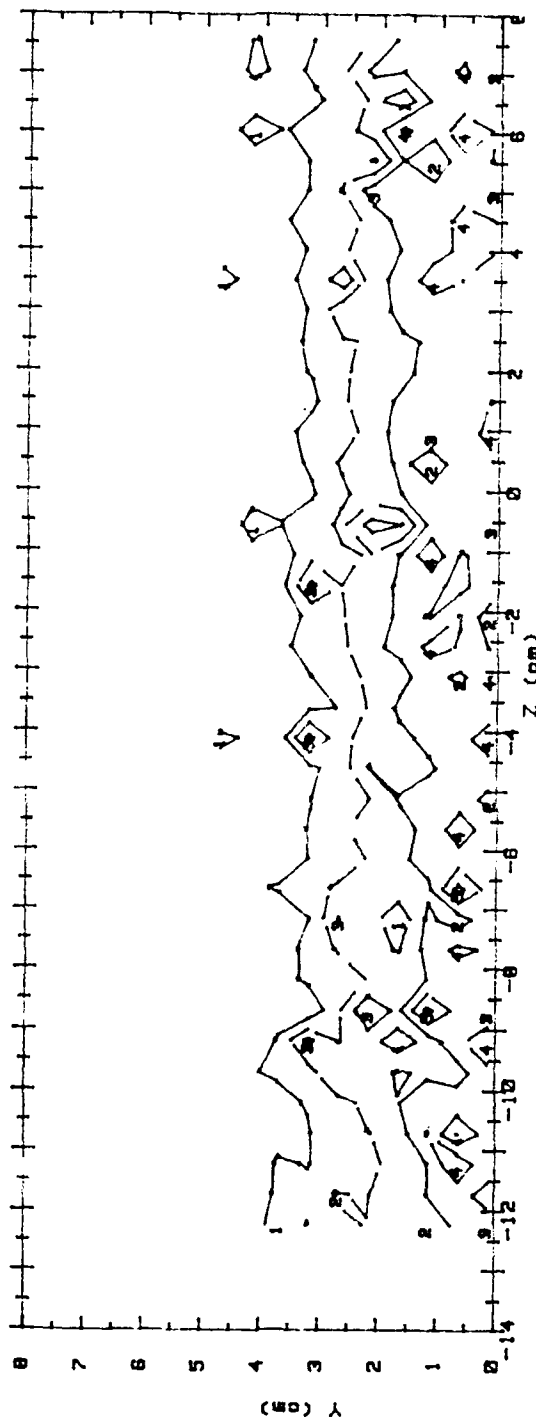
T - Tfs (CELCIUS) RANGES 2 ROWS m=0.5 x/d = 45.8

- | | | | | | |
|---|-------|-------|-------|-------|-------|
| 0 | < .5 | 5 | > 2.5 | < 3 | |
| 1 | > .5 | < 1 | 6 | > 3 | < 3.5 |
| 2 | > 1 | < 1.5 | 7 | > 3.5 | < 4 |
| 3 | > 1.5 | < 2 | 8 | > 4 | < 4.5 |
| 4 | > 2 | < 2.5 | 8 | > 4.5 | |

Figure 80. Local Injectant Distribution, 2 rows m=0.5, x/d=45.8

RUN #80790.1113

T - Tfs



T - Tfs(CELCIUS) RANGES 2 ROWS m=0.5 x/d = 86.8

0 1	< .5	5 1	> 2.5	< 3	
1 1	> .5	< 1	6 1	> 3	< 3.5
2 1	> 1	< 1.5	7 1	> 3.5	< 4
3 1	> 1.5	< 2	8 1	> 4	< 4.5
4 1	> 2	< 2.5	8 1	> 4.5	

Figure 81. Local Injectant Distribution, 2 rows m=0.5, x/d=86.8

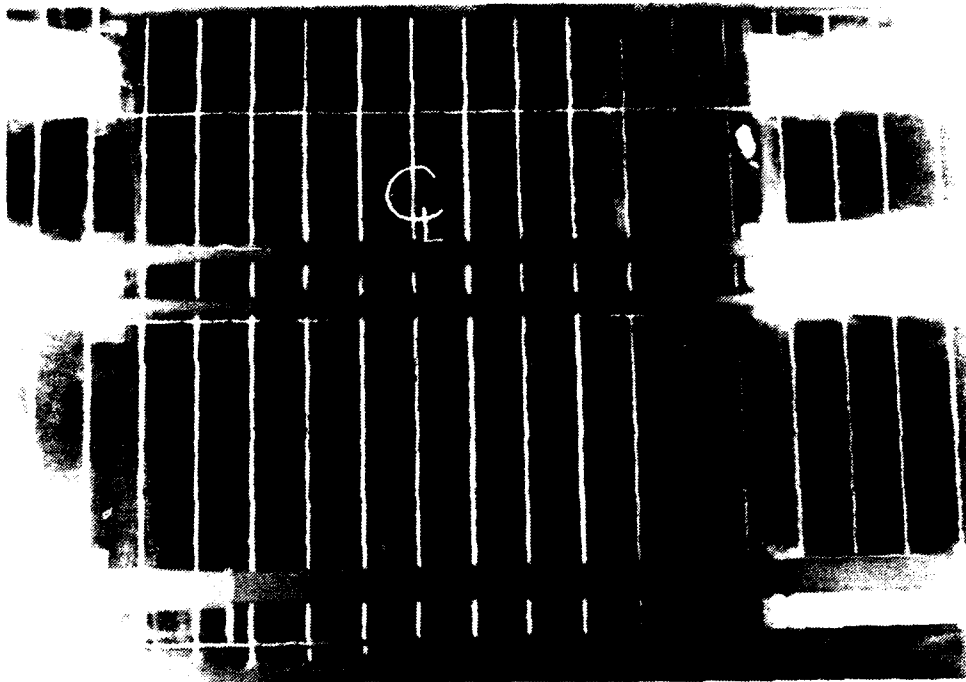


Figure 82. Flow Visualization, 1 row $m=0.5$

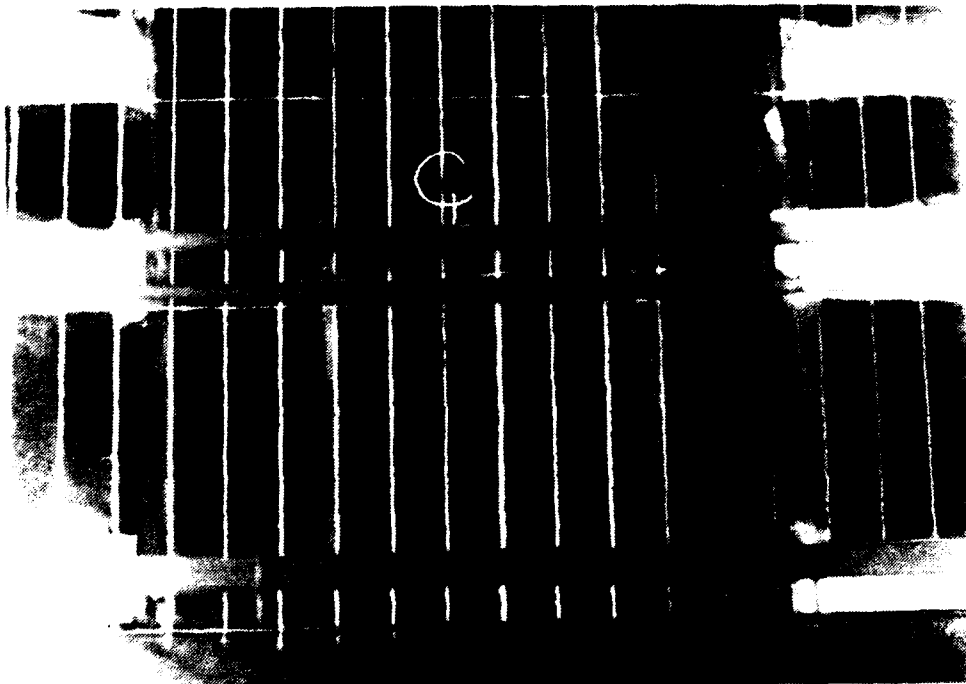


Figure 83. Flow Visualization, 1 row $m=1.0$

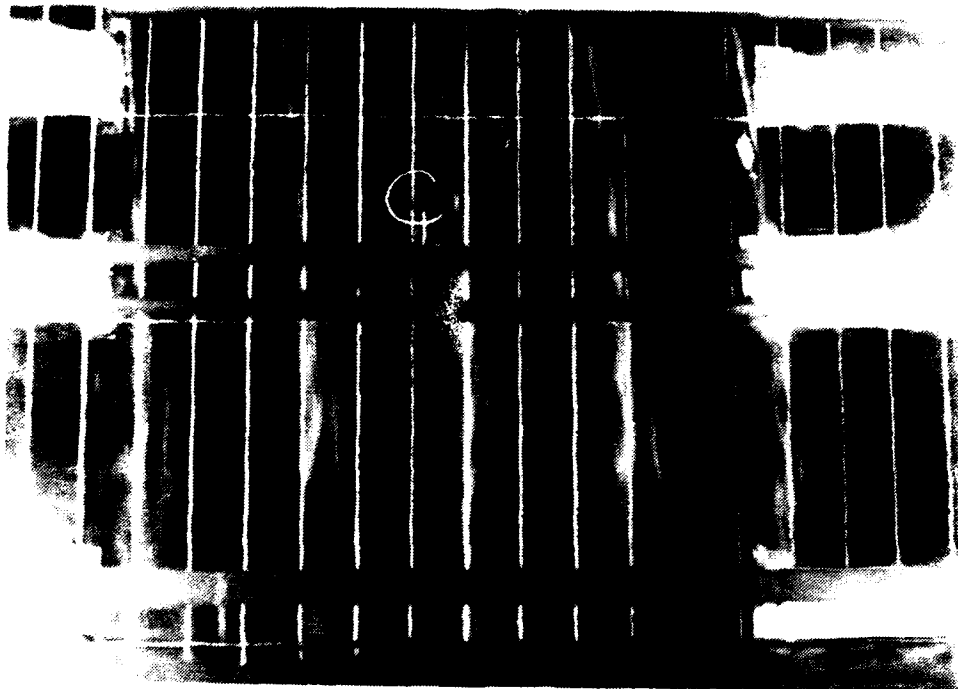


Figure 84. Flow Visualization, 1 row $m=1.5$

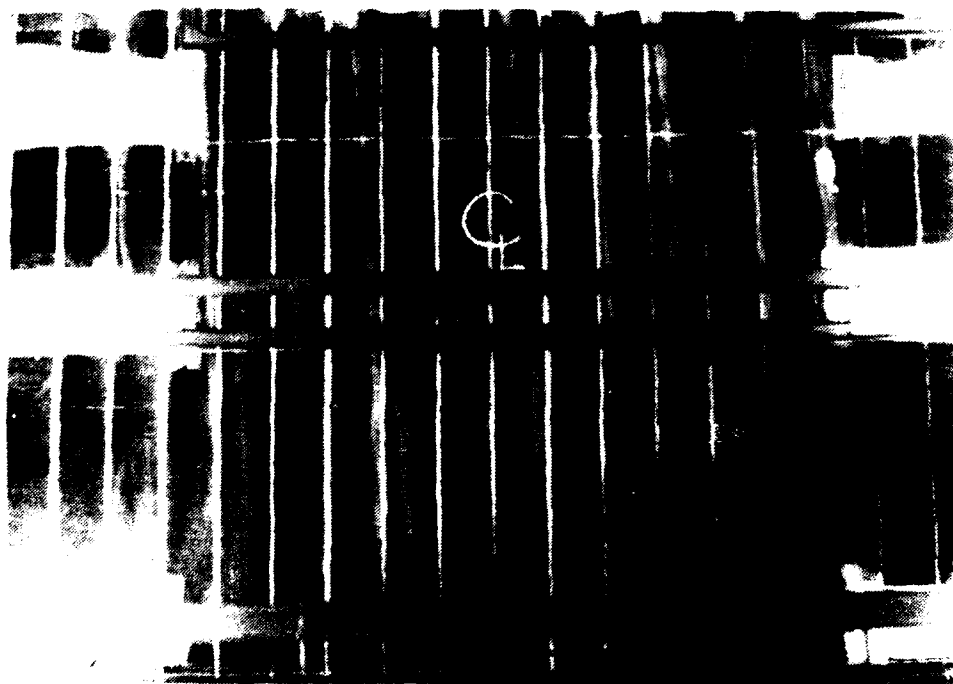


Figure 85. Flow Visualization, 2 rows $m=0.5$



Figure 86. Flow Visualization, 2 rows $m=1.0$

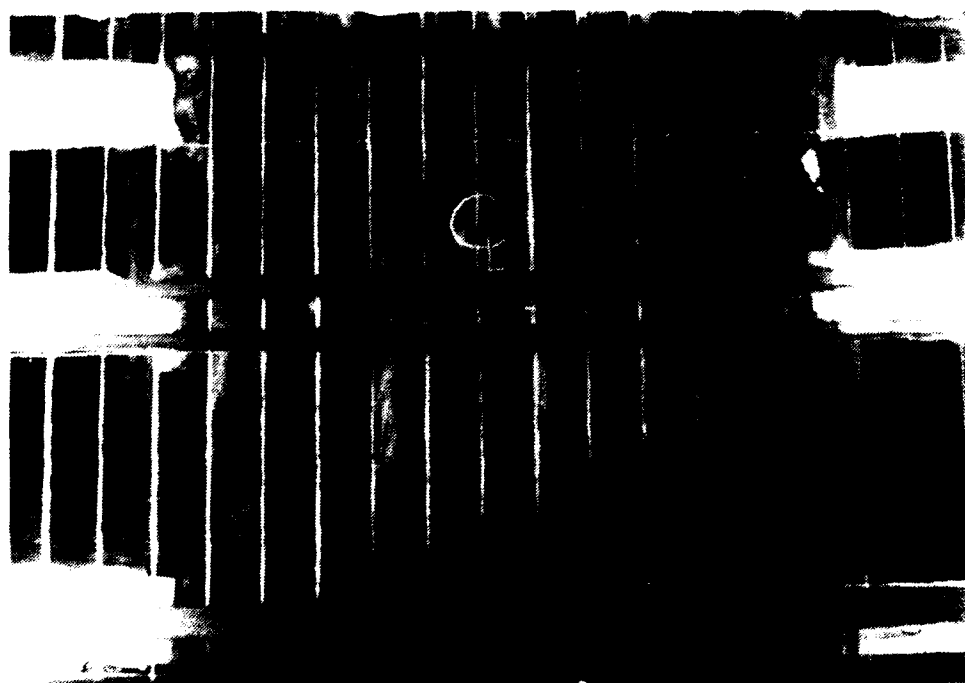


Figure 87. Flow Visualization, 2 rows $m=1.5$

APPENDIX B

UNCERTAINTY ANALYSIS

An uncertainty analysis, by Schwartz [Ref. 8], was accomplished on the input parameters and variables used for this study. A 95% confidence interval was utilized. Table II contains a summary of the parameters and their uncertainties :

TABLE II. EXPERIMENTAL UNCERTAINTIES FOR MEASURED QUANTITIES

<u>Quantity (units)</u>	<u>Typical Nominal Value</u>	<u>Experimental Uncertainty</u>
T_{∞} ($^{\circ}\text{C}$)	18.0	0.13
T_w ($^{\circ}\text{C}$)	40.0	0.21
P_{ambient} (mm Hg)	760	0.71
ρ_{∞} (kg/m^3)	1.23	0.009
U_{∞} (m/s)	10.0	0.06
C_p [J/(kg K)]	1006	1
$q_w A$ (W)	270	10.5
h [W/(m^2 K)]	24.2	1.03
St	0.00196	0.000086
St/St ₀	1.05	0.058
A (m^2)	0.558	0.0065
m	0.98	0.05
x/d	54.6	0.36

APPENDIX C

DATA ACQUISITION, PROCESSING AND PLOTTING PROGRAMS

1. Mean Velocity Survey Software :

ORIENT : This program calculates calibration coefficients for each of the five pressure transducers associated with the five sensing ports of the five hole pressure probe. **ORIENT** is also used to orient the five hole probe so that at a 0 yaw angle the pressures from the right and left ports are equal.

FIVEHOLE1 : This program acquires pressure data from each of the five transducers associated with the probe. The **FIVEHOLE1** program controls the MITAS motor controller which, in turn, controls the automatic traversing device on which the five hole probe is mounted. An 400 point pressure survey is conducted in the Y-Z plane normal to the freestream flow. Two data files, **FIV** and **FIVP**, are created. The **FIV** data file consists of mean velocity, center port pressure, average pressure of the four peripheral ports, and the yaw and pitch coefficients for each of the 400 locations sampled. The **FIVP** data file consists of the pressures P1 through P5 sensed by each of the five pressure probe sensing ports, the average pressure of the four peripheral ports and the mean velocity, for each of the 400 survey locations.

PADJUST : This program accesses the **FIV^P** data file created by **FIVEHOLE1** and adjusts the pressures to account for spatial resolution

problems. Pressure correction is performed using a curve fit to move the measurement location to the center sensing port location.

VELOCITY : This program accesses the data file created by PADJUST and computes U_x , U_y and U_z velocity components.

UX3 : This program accesses the data file created by VELOCITY and plots streamwise velocity (U_x) contours of the Y-Z plane surveyed by the five hole pressure probe.

PTOT3 : PTOT3 accesses the VELOCITY program data file and plots total pressure contours of the surveyed Y-Z plane.

2. Mean Temperature Survey Software :

ROVER1 : This program acquires flow temperature data from the "roving" thermocouple mounted on the automatic traversing device. The traversing device is controlled by the MITAS controller which is, in turn, controlled by this program. The output data file consists of differential temperatures ($T_{\text{rover}} - T_{\text{ref}}$) for each of the 400 survey locations in the Y-Z plane.

PLTMP3 : This program uses the differential temperature data file created by ROVER and plots differential temperature contours of the surveyed Y-Z plane.

3. Heat Transfer Measurement Software (No Film Cooling) :

STANTON3 : This program acquires multiple channel thermocouple data for heat transfer measurements with no film cooling. It creates two output data files, TDATA and IDATA. The TDATA file consists of the 126 test plate thermocouple temperatures. The IDATA file records run number, test plate voltage and current, ambient pressure, pressure differential, ambient temperature, freestream velocity, air density and freestream temperature.

STANTON4 : STANTON4 accesses TDATA and IDATA files created by STANTON3 and calculates heat transfer coefficients and Stanton numbers for each of the 126 thermocouple locations. This program also calculates the average Reynolds number for each thermocouple row. STANTON4 creates three output files. These files are HDATA, SDATA, and STAV. The HDATA file consists of the local heat transfer coefficient, the Stanton number and the X and Z coordinates for each of the 126 test plate thermocouples. The SDATA file contains only the Stanton number values calculated for each thermocouple location. STAV contains the X location and the average Reynolds and Stanton numbers for each of the six thermocouple rows.

4. Heat Transfer Measurement Software (with Film Cooling) :

SETCOND : This program is used to set conditions for heat transfer data acquisition when film cooling is employed. SETCOND determines injection

velocity, Reynolds number, blowing ratio (m) and non-dimensional temperature (θ). It requires user input from the terminal of freestream conditions, rotometer percent flow and injection plenum differential pressure.

STANFC1A : This program is used when film cooling is employed to acquire multiple channel thermocouple data for heat transfer measurements. STANFC1A creates three data files : a temperature data file (T), a terminal input data file (I) and a film cooling data file (FC). The temperature data file consists of the 126 test plate thermocouple temperatures. The terminal input data file records the identical information contained in the IDATA file of STANTON3, as discussed earlier. The film cooling data file contains the injection rotometer percent flow and the injection plenum differential pressure.

STANFC2A : This program accesses the temperature, terminal input and film cooling data files created by STANFC1A. The program calculates Stanton number values for the 126 thermocouple locations and creates a single output file (ST) containing these values.

STANR1 : This program reads three Stanton number data files and creates a single output file containing two Stanton number ratios for each of the 126 thermocouple locations. The required input data files are : SDATA file created by STANTON4 containing baseline Stanton numbers for no film cooling and two ST data files created by STANFC2A containing Stanton numbers with film cooling.

FLMEFF6 : This program processes Stanton number data and calculates the local and spanwise averaged film cooling effectiveness and iso-energetic Stanton number ratios. The program reads several files and creates two output files. The program reads the SDATA file created by STANTON4 which contains the baseline Stanton numbers for no film cooling and up to six ST, TDATA and IDATA files created by STANFC2A. One of the two output data files contains the local effectiveness and iso-energetic Stanton number ratios and the other output file contains the spanwise averaged effectiveness and iso-energetic Stanton number ratios.

3DSTGETA : This program accesses the files created by FLMEFF6 and plots the spanwise variation of effectiveness in three-dimensional form.

3DSTGSTIRS : This program accesses the files created by FLMEFF6 and plots the spanwise variation of the iso-energetic Stanton number ratio in three-dimensional form.

3DSTRST : This program accesses the Stanton number ratio file created by STANR1 and plots the spanwise variations of the Stanton number ratios in three-dimensional form.

APPENDIX D

DATA FILE DIRECTORY

1. Heat Transfer Data:

A. STANTON3 / STANTON4 data files -- (no film cooling) :

TDATAxx ---- temperature data file
IDATAxx ---- user terminal input data file
HDATAxx ---- heat transfer coefficient data file
SDATAxx ---- local Stanton number data file

<u>Data Run #</u>	<u>Data File</u>	<u>Experimental Conditions</u>
071090.1234	TDATA55 IDATA55 HDATA55 SDATA55	no film cooling

B. STANFC1A / STANFC2A data files -- (film-cooling)

Txx ---- temperature data file
Ixx ---- user terminal input data file
FCxx ---- film-cooling parameters data file
STxx ---- local Stanton number data file

<u>Data Run #</u>	<u>Data File</u>	<u>Experimental Conditions</u>
070590.1352	T65 I65 FC65 ST65	2 rows $m=0.5$ $\theta=0.0$

070590.1355	T66 I66 FC66 ST66	2 rows $m=0.5$ $\theta=0.0$
070590.1536	T67 I67 FC67 ST67	2 rows $m=0.5$ $\theta=0.47$
070590.1540	T68 I68 FC68 ST68	2 rows $m=0.5$ $\theta=0.49$
071090.1835	T72 I72 FC72 ST72	2 rows $m=0.5$ $\theta=0.79$
071090.1840	T73 I73 FC73 ST73	2 rows $m=0.5$ $\theta=0.81$
070590.1654	T63 I63 FC63 ST63	2 rows $m=0.5$ $\theta=1.13$
070590.1659	T64 I64 FC64 ST64	2 rows $m=0.5$ $\theta=1.11$

071090.2053	T74 I74 FC74 ST74	2 rows $m=0.5$ $\theta=1.36$
071090.2101	T75 I75 FC75 ST75	2 rows $m=0.5$ $\theta=1.39$
070590.1801	T60 I60 FC60 ST60	2 rows $m=0.5$ $\theta=1.66$
070590.1805	T62 I62 FC62 ST62	2 rows $m=0.5$ $\theta=1.65$
071190.0954	T80 I80 FC80 ST80	1 row $m=0.5$ $\theta=0.0$
071190.0958	T81 I81 FC81 ST81	1 row $m=0.5$ $\theta=0.0$
071490.1448	T82A I82A FC82A ST82A	1 row $m=0.5$ $\theta=0.57$

071490.1451	T83A I83A FC83A ST83A	1 row $m=0.5$ $\theta=0.57$
071190.1554	T84 I84 FC84 ST84	1 row $m=0.5$ $\theta=0.9$
071190.1559	T85 I85 FC85 ST85	1 row $m=0.5$ $\theta=0.91$
071190.1854	T86 I86 FC86 ST86	1 row $m=0.5$ $\theta=1.29$
071190.1858	T87 I87 FC87 ST87	1 row $m=0.5$ $\theta=1.3$
071190.2155	T88 I88 FC88 ST88	1 row $m=0.5$ $\theta=1.16$
071190.2159	T89 I89 FC89 ST89	1 row $m=0.5$ $\theta=1.18$

071290.0953	T90 I90 FC90 ST90	1 row $m=1.0$ $\theta=0.0$
071290.0957	T91 I91 FC91 ST91	1 row $m=1.0$ $\theta=0.0$
071290.1251	T92 I92 FC92 ST92	1 row $m=1.0$ $\theta=0.53$
071290.1255	T93 I93 FC93 ST93	1 row $m=1.0$ $\theta=0.52$
071290.1611	T94 I94 FC94 ST94	1 row $m=1.0$ $\theta=0.72$
071290.1615	T95 I95 FC95 ST95	1 row $m=1.0$ $\theta=0.74$
071290.1859	T96 I96 FC96 ST96	1 row $m=1.0$ $\theta=1.03$

071290.1902	T97 I97 FC97 ST97	1 row m=1.0 theta=1.02
071290.2151	T98 I98 FC98 ST98	1 row m=1.0 theta=1.21
071290.2156	T99 I99 FC99 ST99	1 row m=1.0 theta=1.23

C. FILM EFFECTIVENESS DATA

Generating Program : FLMEFF6

FE_{xx} ---- local effectiveness data file

SPAVG_{xx} ---- spanwise average effectiveness data file

<u>Data Run #</u>	<u>Data File</u>	<u>Experimental Conditions</u>
070590.1352	FE42	2 rows m=0.5
070590.1540	SPAVG42	6 data sets
071090.1835		
070590.1654		
071090.2053		
070590.1805		

070590.1352	FE43	2 rows m=0.5
071090.1835	SPAVG43	5 data sets
070590.1654		
071090.2053		
070590.1805		

071190.0958	FE41	1 row m=0.5
071490.1451	SPAVG41	
071190.2155		
071190.1854		

071290.0953	FE40	1 row m=1.0
071290.1251	SPAVG40	
071290.1611		
071290.1859		
071290.2151		

D. STANTON NUMBER RATIO FILES

Generating Program : STANR1

STRxx ---- Film-coolig data file

<u>Data Run #</u>	<u>Data File</u>	<u>Experimental Conditions</u>
070590.1801	STR10	2 rows m=0.5
071190.1854	STR11	1 row m=0.5
071290.2151	STR12	1 row m=1.0

E. MEAN VELOCITY DATA :

<u>Data Run #</u>	<u>Data File</u>	<u>Generating Program</u>	<u>Experimental Conditions</u>
080290.0914	FIV01 FIVP01 FIV0A V1	FIVEHOLE1 FIVEHOLE1 PADJUST VELOCITY	1 row m=0.5 x/d = 10.2
080290.1847	FIV02 FIVP02 FIV0B V2	FIVEHOLE1 FIVEHOLE1 PADJUST VELOCITY	1 row m=1.0 x/d = 10.2
080390.0941	FIV03 FIVP03 FIV0C V3	FIVEHOLE1 FIVEHOLE1 PADJUST VELOCITY	1 row m=0.5 x/d = 45.8
080490.1234	FIV04 FIVP04 FIV0D V4	FIVEHOLE1 FIVEHOLE1 PADJUST VELOCITY	1 row m=1.0 x/d = 45.8
080490.1531	FIV05 FIVP05 FIV0E V5	FIVEHOLE1 FIVEHOLE1 PADJUST VELOCITY	2 rows m=0.5 x/d = 45.8
080490.1837	FIV06 FIVP06 FIV0F V6	FIVEHOLE1 FIVEHOLE1 PADJUST VELOCITY	2 rows m=0.5 x/d = 10.2
080590.0857	FIV07 FIVP07 FIV0G V7	FIVEHOLE1 FIVEHOLE1 PADJUST VELOCITY	2 rows m=0.5 x/d = 86.8

080590.1151	FIVC3 FIVP08 FIV0H V8	FIVEHOLE1 FIVEHOLE1 PADJUST VELOCITY	1 row m=0.5 x/d = 86.8
080590.1439	FIV09 FIVP09 FIV0I V9	FIVEHOLE1 FIVEHOLE1 PADJUST VELOCITY	1 row m=1.0 x/d = 86.8

F. Mean Temperature Survey Data :

Generating Program : ROVER1

<u>Data Run #</u>	<u>Data File</u>	<u>Experimental Conditions</u>
080790.0822	TEM0	1 row m=0.5 x/d=86.8
080790.1113	TEM1	2 rows m=0.5 x/d=86.8
080790.1252	TEM2	2 rows m=0.5 x/d=45.8
080790.1415	TEM3	1 row m=1.0 x/d=45.8
080790.1553	TEM4	1 row m=0.5 x/d=45.8
080790.1732	TEM5	1 row m=0.5 x/d=10.2
080790.1906	TEM6	1 row m=1.0 x/d=10.2
080790.2035	TEM7	2 rows m=0.5 x/d=10.2
080690.2108	TEM8	1 row m=0.5 x/d=86.8

REFERENCES

1. Metzger, D.E., Carper, H.J. and Swank, L.R., "Heat Transfer with Film Cooling Near Nontangential Injection Slots", *Journal of Engineering for Power*, pp. 157-163, April, 1968.
2. Ligrani, P.M. and Camci, C., "Adiabatic Film Cooling Effectiveness from Heat Transfer Measurements in Compressible, Variable-Property Flow", *Journal of Heat Transfer*, pp 313-320, May, 1985.
3. Ortiz, A., *The Thermal Behavior of Film Cooled Turbulent Boundary Layers as Affected by Longitudinal Vortices*, M.E. Thesis, Naval Postgraduate School, Monterey, California, September, 1987.
4. Ligrani, P. M., Ortiz, A., Joseph, S. L. and Evans, D.L., "Effects of Embedded Vortices on Film-Cooled Turbulent Boundary Layers", ASME-88-GT-170, ASME Gas Turbine and Aeroengine Congress and Exposition, Amsterdam, The Netherlands, June, 1988, also *ASME Transactions -- Journal of Turbomachinery*, Vol. 111, pp. 71-77, 1989.
5. Joseph, S. L., *The Effects of an Embedded Vortex on a Film-Cooled Turbulent Boundary Layer*, M.E. Thesis, Naval Postgraduate School, Monterey, California, December, 1986.
6. Williams, W., *Effects of an Embedded Vortex on a Single Film-Cooling Jet in a Turbulent Boundary Layer*, M.S. Thesis, Naval Postgraduate School, Monterey, California, June, 1988.
7. Kays, W. M. and Crawford, M. E., *Convective Heat and Mass Transfer*, Second Edition, p. 216, McGraw-Hill Book Company, 1980.
8. Schwartz, G. E., *Control of Embedded Vortices Using Wall Jets*, M.S. Thesis, Naval Postgraduate School, Monterey, California, September, 1988.
9. Mitchell, Stephen W., *The Effects of Embedded Longitudinal Vortices on Heat Transfer in a Turbulent Boundary Layer with Film Cooling from Holes with Compound Angles*, M.S. Thesis, Naval Postgraduate School, Monterey, California, September, 1990.

10. Goldstein, R.J. and Yoshida, T., "The Influence of a Laminar Boundary Layer and Laminar Injection on Film Cooling Performance", *Journal of Heat Transfer*, Vol. 104, pp. 355-362, May, 1982.